From the holdings of the Department of Special Collections , Princeton University Library, Princeton, NJ

These documents are either in the public domain, or can only be used for educational and research purposes (Fair use) as per U.S. Copyright law (text below). By accessing this file, all users agree that their use falls in the public domain or within fair use as defined by the copyrightlaw. We do not charge any permission or usage fees for the publication of images of material inour collections, including those provided by Princeton University Library, via our website, catalog, or directly from staff.For more information regarding copyright, credit, and citation please review the information onthe Copyright, Credit and Citation Guidelines page of our website.
https://library.princeton.edu/special-collections/policies/copyright-credit-and-citation-guidelines. If you have any questions, including how to order higher-quality images from the collection, contact Special Collections Public Services via our Ask Us! Form. https://library.princeton.edu/special-collections/ask-us

Doctoral Dissertations, 2011-2026 Atmospheric and Oceanic Sciences

2015

Non-rotating and rotating radiative-convective equilibrium

Zhou, Wenyu

Princeton, NJ : Princeton University

http://arks.princeton.edu/ark:/88435/dsp01n009w468h

U.S. Copyright law: The copyright law of the United States (Title 17, §108, United States Code) governs the making of photocopies or other reproductions of copyrighted material. Under certain conditions specified in the law, libraries and archives are authorized to furnish a photocopy or other reproduction. One of these specified conditions is that the photocopy or reproduction is not to be used for any purpose other than private study, scholarship, or research. If a user makes a request for, or later uses, a photocopy or reproduction for purposes in excess of fair use that user may be liable for copyright infringement. This institution reserves the right to refuse to accept a copying order if, in its judgment, fulfillment of the order would involve a violation of copyright law. https://www.copyright.gov/title17/title17.pdf

Non-rotating and rotating radiative-convective equilibrium

Wenyu Zhou

A Dissertation
Presented to the Faculty
of Princeton University
in Candidacy for the Degree
of Doctor of Philosophy

Recommended for Acceptance
by the Program in
Atmospheric and Oceanic Sciences
Adviser: Isaac M. Held

November 2015

© Copyright by Wenyu Zhou, 2015.

All rights reserved.

Abstract

Radiative-convective equilibrium (RCE), in which the radiative cooling in the atmosphere is balanced by the convective heating in a horizontally homogeneous environment, is a good starting point for studying tropical convection. It also provides an idealized framework to compare analogous simulations by global climate models (GCMs) which rely on convective parameterizations, and cloud-resolving models (CRMs) which aim to explicitly resolve moist convection. In this work, we seek to further our understanding of tropical cyclones and convective aggregation in the idealized framework of non-rotating and rotating RCE with both types of models.

First, we achieve rotating RCE by coupling the resolution and physics of a GCM to rotating hydrostatic dynamics. A large doubly-periodic f-plane is used to allow multiple tropical cyclones (TCs) to coexist. Both cases with fixed and coupled sea surface temperature (SST) are considered. For fixed SST, the sensitivity to environmental parameters is investigated. Particularly, we find that the intensity, radius of maximum wind and size of TCs increase with SST. For coupled SST, SST is predicted using a simple slab ocean model. The effect of the eyewall cooling on TC intensity is studied. We show that Potential-Intensity theory overestimates the impact of the eyewall cooling on TC intensity, as its key assumption that entropy is well-mixed along angular-momentum surfaces within the atmospheric boundary layer no longer holds in cases with substantial eyewall cooling.

We then study TC genesis with a small doubly-periodic f-plane. Through cloud-resolving simulations, we show that vertical shear plays an important role on regulating the sensitivity of tropical cyclogenesis to both the environmental rotation and thermodynamic state. As indicated by analogous simulations with the resolution and physics of GCMs, such effects of wind shear might not be fully represented in GCMs.

Finally, we investigate convective self-aggregation from non-rotating RCE. The critical SST for self-aggregation to occur is sensitive to the model configuration, in the sense that the smaller convective cells the model simulates, the higher the critical SST could be. Such

model sensitivity adds complexity to the dependency of self-aggregation on SST and its implication on the variation of convective aggregation with global warming.

Acknowledgements

I still rememeber the beautiful sunset over the horizon when I first arrived at Princeton five years ago and now it is time to say goodbye. I am going to miss the town of Princeton and the people I met here. I thank everybody who helped me make it to the finish line

First and foremost, I would like to thank my advisor, Isaac Held, for providing invaluable guidance and support over the past five years. I especially enjoyed our frequent conversations, sharing his remarkable insight and deep understandings in atmospheric dynamics. I am also greatly appreciative of his encouragement, which has made me a more confident person than I was five years ago.

Next, I would like to thank the members of my general and thesis committee, Steve Garner, Geoff Vallis and Gabriel Vecchi, for their advices on various stages of my study in Princeton. In particular, I greatly appreciate many meetings with Steve Garner, from whom I have learned my knowledge on tropical cyclones. I would also like to thank Thomas Knutson at GFDL for being one of my thesis readers.

I would like to express my sincere gratitude to students in AOS program. You are the most friendly and intelligent people I have ever met and you have made our AOS program more than a department but also a family.

I have benefited greatly from the research environment at Princeton and GFDL. There are a lot of great scientists and postdocs who have helped me in many ways. In particular, I would like to thank Ming Zhao, for providing the code of HiRAM and also many helpful discussions on moist convective parameterization. Tim Merlis is always generous to share his idea and insights on research. Zhi Liang helps configuring the WRF model on gaea environment. I thank GFDL helpdesk for their kind help in solving many technical problems. The AOS administrative staff has always been friendly and helpful. I am grateful to Anna Valerio, for helping with visa issue and graduation procedures.

I would also like to thank my friends at Princeton, those I met at Princeton and those from my undergraduate department at Tsinghua University. Our occasional get-togethers are always a lot of fun and you have made my life at Princeton much more enjoyable.

Lastly, the greatest thanks should go to my wife, Xiao Chen, for all her love, support, and tolerance on me. What a wonderful journey it has been to meet you at Princeton, get married and have our daughter. You have made me a happier man. Finally, I thank my parents for their unconditional believe in me. Without the education and care that you gave me, I would never made it where I am. Thank you!

Contents

Abstract iii

Acknowledgements v

List of Tables x

List of Figures xi

1 Introduction **1**

1.1 Motivation 1

1.2 Idealized framework of RCE 4

1.3 Outline 6

2 Rotating Radiative-Convective Equilibrium with fixed SST **8**

2.1 Introduction 8

2.2 Model configuration and experiments setup 10

2.3 Varying environmental parameters in turbulent equilibrium 12

2.4 Varying domain size 19

2.5 Conclusions 23

3 Rotating Radiative-Convective Equilibrium with coupled SST **26**

3.1 Introduction 26

3.2 Model Configuration and Experiments 28

3.3 Description 29

3.4 Eyewall cooling of tropical cyclones 32

3.5 Intensity of tropical cyclones . . . 37
3.6 Structure of tropical cyclones . . . 41
3.7 Conclusions . . . 43
3.8 Appendix: A modified PI algorithm considering the eyewall cooling . . . 45

4 The impact of vertical shear on the sensitivity of tropical cyclogenesis to environmental rotation and thermodynamic state 47

4.1 Introduction . . . 47
4.2 Model and Experiments . . . 50
4.2.1 WRF . . . 50
4.2.2 HiRAM . . . 53
4.3 Varying vertical shear in a RCE framework . . . 53
4.4 Varying environmental thermodynamic state . . . 57
4.5 Preliminary results with the resolution and column physics of HiRAM . . . 64
4.6 Conclusions . . . 67

5 Self-aggregation of convection 72

5.1 Introduction . . . 72
5.2 SAM . . . 76
5.2.1 Control experiment . . . 77
5.2.2 Sensitivity to horizontal grid resolution . . . 79
5.2.3 Sensitivity to microphysics scheme . . . 81
5.2.4 Sensitivity to surface flux scheme . . . 82
5.3 WRF . . . 82
5.3.1 Control experiment . . . 83
5.3.2 Sensitivity to the physics schemes . . . 85
5.3.3 Sensitivity to the initial perturbation . . . 85
5.3.4 Sensitivity to SST and domain size . . . 86

5.4 Conclusions 87

6 Conclusions **91**

6.1 Summary 91

6.2 Directions for future research 94

6.2.1 Tropical cyclones 94

6.2.2 Tropical cyclogenesis 95

6.2.3 Convective organization 95

6.2.4 Implications for testing GCM column physics 96

Bibliography **97**

List of Tables

1.1 Summary of thesis context and models in each Chapter. 6

3.1 Approximate values of parameters in the minimalist model for the eyewall cooling. 37

4.1 Characteristic parameters related to tropical cyclogenesis, χ_b and χ_m, computed from soundings. 60

5.1 A list of our experiments 75

List of Figures

1.1 A comparison of (top) observed and (bottom) model-simulated hurricane tracks from 1981 to 2005 (Zhao et al., 2009). 2

1.2 Instantaneous snapshots of clouds (0.4 g kg^{-1}) isosurface and near-surface temperature after 60 days in two simulations with the same resolution dx=2 km but different domain sizes: L=(a) 198 and (b) 510 km. Convection self-aggregates when the domain is large enough, resulting in an atmospheric state with one convectively active moist region (Muller and Held, 2012). 5

1.3 Rotating radiative-convective equilibrium simulated with the resolution and column physics of HiRAM at GFDL in a large domain. Surface shading: sea level pressure; Blue: liquid cloud; Gray: ice cloud. 5

1.4 Rotating radiative-convective equilibrium simulated with the cloud-resolving model WRF in a small domain. Surface shading: sea level pressure; Blue: liquid cloud; Gray: ice cloud. 6

2.1 Snapshots of surface wind (m s^{-1}) for different sea surface temperatures. (left) SST= 297 K; (right) SST = 305 K. f is set at 20°N. 13

2.2 (a) The average number of TCs in the domain with their central surface pressures within the specified 10 hPa interval as a function of SST with f at 20°N. (b) As in (a), but for the sensitivity to f with SST fixed at 301 K. For both sets of experiments, surface exchange coefficients are calculated from Monin-Obukhov scheme. 13

2.3 TC intensity and PI as function of SST (left), f (middle) and C_D. The gray line shows the median of all collected TCs. The first and third quartiles are indicated by the gray box. The black line shows the mean of the strongest storms at each instant of time. The red line shows the estimate from PI theory. 14

2.4 Snapshots of surface wind (m s^{-1}) for different ambient rotation rates with SST fixed at 301 K. (left) f at 5°N; (right) f at 20°N. 15

2.5 Differences in vertical profiles of temperature and specific humidity between (a, b) different f (vs 5°N case) with surface exchange coefficients calculated from Monin-Obukhov scheme; and (c, d) different C_D (vs 2.4x10^{-3} case) with f at 15°N and SST fixed at 301 K. 16

2.6 (a) The average number of TCs in the domain with their central surface pressures within the specified 10 hPa interval as a function of surface drag coefficient C_D (0.6, 1.2, 2.4 $\times 10^{-3}$) with f at 10°N. (b) (c) As in (a), but with f at 15°N and 20°N. C_k is fixed at 1.2×10^{-3} and SST is 301 K. 17

2.7 Time- and azimuthal-mean tangential (colors), radial (white) and vertical (black) velocities of the strongest tropical cyclone for sea surface temperature a) 297 K and b) 305 K with f at 20°N. Tangential winds are contoured at every 5 m s^{-1}. Positive (cyclone) values are solid, negative (anticyclone) values are dashed, and the zero contour is a red dashed line. Radial winds are contoured at [2, 5, 10, 15, 20] m s^{-1}. Positive (outflow) values are dashed, negative (inflow) values are solid. Vertical velocity is contoured (negative only) at [-1, -2, -3] Pa s^{-1}. 18

2.8 The radius of maximum surface wind (R_{mw}) as a function of SST (a), f (b) and C_D (c). The gray line is the median of all collected TC. The first and forth quartiles are indicated by the gray box. The black dash line shows the mean of the strongest storms at each instant of time. 18

2.9 (a) The average number of TCs n (black-dash line with diamond) and the natural extent of TCs r_0 ($\sqrt{\frac{A}{n}}$, gray dash-dot line with circle) as a function of SST. Ambient rotation rate f is set at 20°N. Three possible scalings are shown. Red line: $\sqrt{R_{mw}\frac{V_p}{f}}$; blue line: $\frac{V_p}{f}$; green line: $\frac{NH}{f}$. (b) As in (a) but for the variation of ambient rotation rate f . The underlying SST is 301 K. The estimates from these three scalings are normalized to the natural extent of TCs with SST at 301 K and f at 20°N. 20

2.10 Composite of surface wind for simulations with domain sizes at 1250 km, 2500 km, 5000 km, 7500 km and snapshot of surface wind for domain size at 12500 km, all with SST at 301 K and f at 10°N. 20

2.11 Time series of minimum surface pressure for different regimes. SST is 301 K and ambient rotation rate f is fixed at 10°N. 21

2.12 Time mean TC central surface pressure as a function of domain sizes at (a) different ambient rotation rates and (b) sea surface temperatures. The four regimes mentioned above are marked with different symbols, ∇ (tropical depression), + (intermittent storm), $\circ$ (sustained storm) and $\triangle$ (multiple storms). The average scale of TCs in corresponding large domain simulation is marked with a | symbol. 22

2.13 Sensitivity of R_{mw} to f (black line), SST (red line) and C_D (blue line) in a fixed-size small domain (5000 km on a side). In f and C_D perturbation experiments, SST is fixed at 301 K. In SST and C_D perturbation experiments, ambient rotation rate is set at 15°N. 24

3.1 Snapshots of instantaneous surface winds (m s^{-1}) for simulations with (a) H=0.1 m, (b) H=0.5 m, (c) H=2.5m and (d) H=20m. 27

3.2 Snapshots of instantaneous sea surface temperature (K) for simulations with H=0.1 m (left) and H=20 m (right). 28

3.3 Time and azimuthal-mean height-radius cross-section of horizontal temperature anomaly (K) for simulations with H=0.1 m (left) and H=20 m (right). . 30
3.4 The domain-mean SST (black solid line), the maximum and minimum of the azimuthally-mean SST ($\widetilde{SST}_{max}$ and $\widetilde{SST}_{min}$, thin black dash lines) around tropical cyclones. 31
3.5 (a) The vertical profile of the domain-mean cloud amount; (b) The differences in the cloud radiative forcing at TOA for shortwave (gray line with circle symbol), longwave (gray line with diamond symbol) and total (black line) between simulations with coupled SST and the simulation with fixed SST. . 32
3.6 (a) The differences in vertical profiles of domain-mean temperature between simulations with coupled SST and the simulation with fixed SST. (b) The correlation between SST in the eyewall region and the mean lapse rate between 250 hPa and 950 hPa, computed as $-(T_{250}-T_{950})/(Z_{250}-Z_{950})$. (c) The same as (a) but for relative humidity. (d) The same as (a) but for specific humidity. 33
3.7 The relative cooling of the eyewall, $\triangle SST = \widetilde{SST}_{max} - \widetilde{SST}_{min}$, simulated by the model (black solid line) and estimated by Eqn. 3.9 (thin black dash line). 34
3.8 The time- and azimuthal-mean surface fluxes and SST as a function of the distance from TC center for different depths of slab ocean layer. (a) SST; (b) The net surface energy flux; (c) The net shortwave (solid) and net longwave flux (dash) at the surface; (d) The latent (solid) and sensible (dash) heat flux at the surface. 35
3.9 Intensity and PIs as a function of H. The gray solid lines show the median intensity of tropical cyclones and the gray dash lines indicate the first and third quartiles; The red lines show PI computed from the original algorithm (PI-O); The blue lines show PI computed from the modified PI algorithm considering the eyewall cooling (PI-E). 38

3.10 The time- and azimuthal-mean surface disequilibrium of enthalpy as a function of the distance from TC center in simulations with different depths of slab ocean layer. The surface disequilibrium is computed as $\delta k = \delta t + L_v \delta q / C p_a$ where δt and δq are the differences in temperature and specific humidity between the saturated surface and the surface air (at the first model level). The cross symbols indicate the locations of the eyewall. 39

3.11 Time and azimuthal-mean height-radius cross-section of angular momentum (m^2 s^{-1}, top) and equivalent potential temperature (K, bottom) for simulations with H=0.1 m (left) and H=20 m (right). 41

3.12 Time and azimuthal-mean height-radius cross-section of tangential wind (color shade), radial wind (black contour) and vertical velocity (white contour) for simulations with H=0.1 m (left) and H=20 m (right). Radial winds are contoured at 2, 5, 10, 15 m s^{-1}. Positive (outflow) values are dotted, negative (inflow) values are solid. Vertical velocity is contoured at 0.2, 0.3 m s^{-1} (K). 42

3.13 (a) The variation of the radius of the maximum wind (R_{MW}) as a function of H. The black solid lines with diamond maker show the median value. The gray box indicates the first and third quartiles. (b) The size of tropical cyclones calculated as $L = \sqrt{A/n}$ (black solid line). Rossby radius of deformation $\sqrt{NH/f}$ is shown as the gray dash line. The stratification stability is calculated as $N^2 = g/\theta_o \delta\theta/\delta_z$, where θ_o is the potential temperature at 500 hPa, $\delta\theta$ is the difference in potential temperature between 200 hPa and 900 hPa. The scaling height of atmosphere is set as a constant of 8 km. The scaling of $\sqrt{V_M/f}$ is shown as the gray dash-dot line and $\sqrt{R_{MW} V_M/f}$ is shown as the gray solid line. 43

4.1 Time series of maximum azimuthal-mean wind in simulations of tropical cyclogenesis in a quiescent environment with the Coriolis parameter at 10^oN, 20^oN, and 30^oN (Smith et al., 2014). 49

4.2 Radius-height cross-section of the azimuthal wind field (m s^{-1}) for the initial (a) bottom vortex with z_0=0 m, L_z=5000 m and (b) mid-level vortex with z_0=3720 m, L_z=3175.23 m. We use b=120 km and R = 4000 km for both vortexes. 51
4.3 Six environmental wind profiles used in this study. 52
4.4 Vertical profiles of (a) temperature, (b) specific humidity and (c) relative humidity in differet soundings. 53
4.5 Time evolution of the minimum surface pressure in simulations initialized from a bottom vortex with a vertical shear of (a) easterly 7 m s^{-1}; (b) easterly 5 m s^{-1}; (c) easterly 3 m s^{-1}; (d) 0 m s^{-1}; (e) westerly 3 m s^{-1}; (f) westerly 5 m s^{-1}. The surface wind is 3 m s^{-1} westerly. 55
4.6 As in Figure 4.5 but for simulations initialized from a mid-level vortex. . . . 56
4.7 Surface pressure (black contour at each 5 hPa from 1010 hPa), smoothed relative vorticity at 500 hPa (blue contour at each 0.25 s^{-1} from 0.25 s^{-1}), and column-integrated relative humidity (shading) at Hour 24, 48 and 72 in the simulation with f at 10^oN and initialized from a mid-level vortex in an environmental flow with a westerly surface wind of 3 m s^{-1} and a westerly wind shear of 5 m s^{-1}. The circulation center at 900 hPa is denoted as a black cross symbol and the circulation center at 500 hPa is denoted as a blue cross symbol. 56
4.8 As in Figure 4.7 but with f at 20^oN at Hour 24, 48, 72, 96, 120, 144 (from left to right; from top to bottom). 57
4.9 As in Figure 4.7 but with f at 30^oN at Hour 24, 48, 72. 57
4.10 The magnitude (top) and angle (middle) of the tilt between the surface and the mid-level vortices and the magnitude of the local wind shear (bottom) in simulations with a 5 m s^{-1} westerly vertical shear initialized from a bottom (left) or mid-level (right) vortex. 58

4.11 Time evolution of the minimum surface pressure in simulations with a 3 m s^{-1} westerly vertical shear for various initial environmental thermodynamic states. 59
4.12 Time evolution of the minimum surface pressure in simulations with a quiescent environment for various initial environmental thermodynamic states. . . 59
4.13 Time-radius cross-section of convective available potential energy (CAPE) in simulations with f at 10^0N (top) and 30^oN (bottom) for different environmental thermodynamic states. 60
4.14 Time-radius cross-section of the radial flow in the boundary layer in simulations with f at 10^0N (top) and 30^oN (bottom) for different environmental thermodynamic states. 62
4.15 Time-radius cross-section of the equivalent potential temperature in the boundary layer in simulations with f at 10^0N (top) and 30^oN (bottom) for different environmental thermodynamic states 63
4.16 Time evolution of the minimum surface pressure in simulations initialized from the RE (top) and MT (bottom) soundings with varying SST. The environment is quiescent. 64
4.17 Interannual variation of hurricane numbers for North Atlantic from 1981 to 2005. IBTrACS observations (red) and four-member ensemble mean (blue); shaded area shows the simulated maximum and minimum number for each year. Model time series are normalized by time independent multiplicative factors so as to reproduce the observed total number. Dotted lines show observed and model linear trends (Zhao et al., 2009). 65
4.18 Time evolution of the maximum surface wind in simulations with the resolution and column physics of HiRAM at GFDL, initialized from a bottom (left) and mid-level (right) vortex in a quiescent environment. 66

4.19 Time evolution of the maximum surface wind in simulations with the resolution and column physics of HiRAM at GFDL, initialized from a bottom (left) and mid-level (right) vortex in an environment with a 3 m s^{-1} westerly surface wind and a 3 m s^{-1} westerly vertical shear between 200 hPa and 850 hPa. . 66

5.1 The instantaneous isosurface of condensate water content (0.05 g kg^{-1}) with column precipitable water (PW, in mm) for Day 1, 10, 30 and 60 in the control experiment using SAM model. 78

5.2 Time evolution of domain mean of terms in the $\hat{h}'^2$ budget, each normalized by $\hat{h}'^2$, with the unit of day^{-1}. Plotted is the correlation between vertically integrated column FMSE anomalies and column longwave flux convergence (blue), column shortwave flux convergence (red), surface enthalpy flux (black), and horizontal convergence of flux of FMSE (black dashed). 79

5.3 The variance of column relative humidity at 'aggregated' scale ($\triangle$**CRH**) as a function of time in various runs for (a) SAM and (b) WRF model. 80

5.4 The instantaneous isosurface of condensate water content (0.05 g kg^{-1}) and near-surface air temperature (at the first model level of 37.5 m) in small-domain RCE simulations with SAM model and horizontal resolution of (a) 3 km (b) 3km but with the Morrison et al. (2005) microphysics; (c)1 km and (d) 0.5 km. 81

5.5 The instantaneous isosurface of condensate water content (0.05 g kg^{-1}) with column precipitable water (PW, in mm) for Day 60 in the control experiment using the WRF model. 83

5.6 The instantaneous isosurface of condensate water content (0.05 g kg^{-1}) and near-surface air temperature (at the first model level of 37.5 m) in small-domain RCE simulations with WRF model and horizontal resolution of (a) 3 km (b) 1 km and (c) 0.5 km. 84

5.7 The instantaneous isosurface of condensate water content (0.05 g kg^{-1}) with column precipitable water (PW, in mm) for (a) Hour 6 and (b) Hour 12 , (c) Day 2, (d) Day 10, (e) Day 30 and (f) Day 60 in the WRF run initialized with a moist bubble ($\triangle q_v = 1.5$ g kg^{-1}) in the center of the domain. 87

5.8 The instantaneous isosurface of condensate water content (0.05 g kg^{-1}) with column precipitable water (PW, in mm) for (a) Hour 6 and (b) Hour 12 , (c) Day 2, (d) Day 10 in the WRF run initialized with a moist bubble ($\triangle q_v = 1.0$ g kg^{-1}) in the center of the domain. 88

5.9 The schematic dependence of self-aggregation on sea surface temperature (SST) and the horizontal grid resolution ($\triangle X$) in SAM and WRF model. Above the curve, convection spontaneously aggregates if the domain size is large enough. 89

Chapter 1

Introduction

1.1 Motivation

Earth's climate is a highly complex system composed of turbulent flows interacting at a wide range of spacial scales. Large-scale circulations such as Hadley cell exist on a planetary scale, convective clouds have scales varying from hundreds to thousands of meters while microphysical processes like the formation of rain occur on a scale of micrometers. This wide span of spacial scales has brought difficulty to numerical simulations. For example, global climate models (GCMs), that integrate the primitive equations of geophysical fluid flows globally, are currently run at some cut-off grid scale around 25-50 km or larger. This resolution is far away from resolving small-scale processes like moist convection, not to mention microphysical processes, such that these processes have to be carefully parameterized by subgrid closures, which we refer to as the column physics of GCMs. Among all parameterizations in GCMs, the component of moist convection has been a particular challenge. Although tremendous efforts have been made in developing reliable convective parameterizations (Arakawa, 2004), they still suffer from inaccuracy and contribute to many biases in current generation of GCMs. The different convective closures in various GCMs not only contribute to the inter-model scatter in their simulations of the current climate and projections of future climate

change (e.g. Frierson, 2007) but also lead to strengths and limitations in specific aspects of model simulations, such as tropical cyclones (e.g. Zhao et al., 2009), Convectively Coupled Equatorial Waves (e.g. Lin et al., 2008), Madden-Jullian Oscillation (e.g. Kim et al., 2014a) and diurnal cycle of convection over land (e.g. Bechtold et al., 2004; Wang et al., 2007). Particularly, by replacing the relaxed Arakawa-Schubert convective closure (Moorthi and Suarez, 1992a) in an earlier model, AM2 (GAMDT, 2004), with a shallow convection scheme (Bretherton et al., 2004; Zhao et al., 2009) which results in a larger fraction of precipitation occurring at the resolved scale rather than through the parameterization, the High Resolution Atmospheric Model at GFDL (HiRAM) is able to realistically simulate the observed global climatology and interannual variability of hurricane frequency at 50-km resolution (Figure 1.1). However, its simulations of Madden-Jullian Oscillation and the diurnal cycle of convection over land are not very realistic.

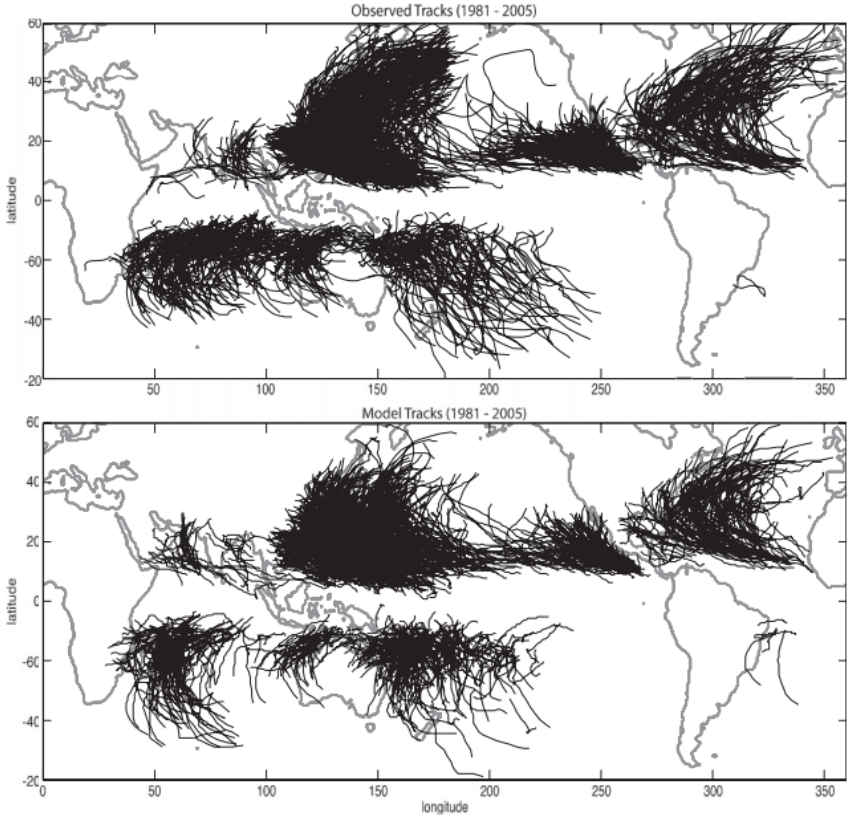

Figure 1.1: A comparison of (top) observed and (bottom) model-simulated hurricane tracks from 1981 to 2005 (Zhao et al., 2009).

It is thus important to understand the strength and weakness of convective parameterizations. There is however a gap between understanding and simulation in GCMs due to the complexity of the realistic climate system. One way to degrade the complexity is to design a model hierarchy as suggested in Held (2005). For example, the widely-used single-column model allows one to focus on the column physics of GCMs by isolating the interaction with the large-scale dynamics (e.g. Derbyshire et al., 2004; Guichard et al., 2004). The single-column geometry however does not allow the interaction between horizontal grid points and excludes any structures of moist convection. One step further, one can achieve the three-dimensional dynamical radiative-convective equilibrium (RCE) by coupling the column physics of GCMs with hydrostatic dynamics in a doubly-periodic domain (e.g. Held et al., 2007; Held and Zhao, 2008), which then allows moist convection to be organized into certain structures that we are interested in, such as tropical cyclones and convective aggregation.

While it is not feasible with current computational power to get rid of the convective closure globally, cloud-system resolving models (CRMs) with a horizontal resolution of several kilometers or smaller, are affordable in a limited domain. With the ability to explicitly resolve moist convection (at least the deep convection), CRMs no longer need to rely on convective parameterizations and have been an increasingly used tool to help us understand the physics of moist convection (e.g. Khairoutdinov and Randall, 2003). Moreover, idealized simulations of CRMs in the framework of RCE provides a 'ground truth' to be compared by the analogous simulations with the resolution and column physics of GCMs. Such comparison between CRMs and GCMs will bring valuable insights into our understanding of the column physics of GCMs. The specific aspects about the idealized framework of RCE we study in this thesis is introduced in the following section.

1.2 Idealized framework of RCE

Moist convection in the tropics is a unique and important ingredient of Earth climate system, which not only plays a key role in determining small-scale local processes but can also affects the large-scale environment through their dynamic and radiative effect. On large enough space and time scale, tropical convection can be viewed as in a radiative-convective equilibrium (RCE) in which the convective heating stabilizes the atmosphere at the same rate as the atmosphere is destabilized by radiative cooling. In the simplest version of RCE one typically ignores spherical geometry and places the flow in a doubly-periodic domain with horizontally homogeneous forcing and boundary conditions. Such a framework has been a widely-accepted paradigm for understanding tropical convection and used to address many important questions, such as, the scaling of precipitation extreme with warming (Romps, 2010; Muller, 2013), the atmospheric stability (Singh and O'Gorman, 2013) and the entropy budget of convection (Pauluis and Held, 2002a,b).

Given the homogeneous boundary conditions and forcing, convection in simulations of RCE is naturally expected to be statistically uniform in space and time. However, under certain condition, convective clouds are found to be spontaneously organized into a moist, convecting patch surrounded by a large area of dry, non-convecting air. Such phenomenon has been referred to as 'self-aggregation'. (Figure 1.2). On the one hand, such aggregation adds complexity to the framework of RCE; On the other hand, it provides a good starting point to study convective organization, which is frequently observed in the tropics (Mapes and Houze, 1993; Futyan and Del Genio, 2007) and has important impacts on both tropical climate and weather (Nesbitt et al., 2000; Tobin et al., 2012, 2013).

In most applications of RCE, the flow is assumed to be non-rotating, but it is also interesting to study the rotating cases. By using a doubly-periodic f-plane, we achieve rotating radiative-convective equilibrium (RRCE) with convection organized into tropical cyclones (TCs). Such a framework can be used in two different ways to study tropical cyclogenesis and mature tropical cyclones respectively.

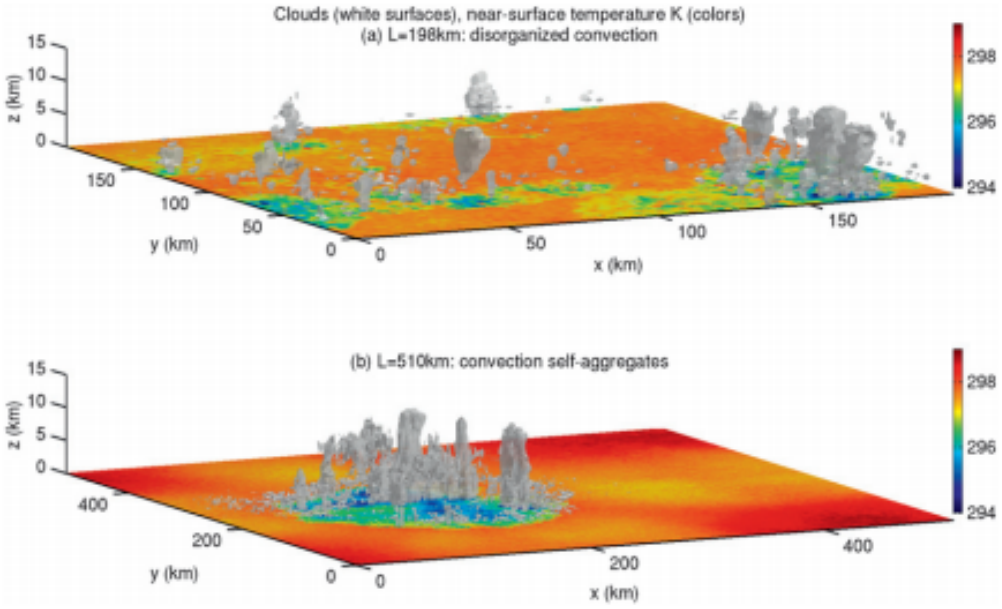

Figure 1.2: Instantaneous snapshots of clouds (0.4 g kg^{-1}) isosurface and near-surface temperature after 60 days in two simulations with the same resolution dx=2 km but different domain sizes: L=(a) 198 and (b) 510 km. Convection self-aggregates when the domain is large enough, resulting in an atmospheric state with one convectively active moist region (Muller and Held, 2012).

With a large domain, one can achieve an equilibrium with multiple long-lived tropical cyclones coexisting (Figure 1.3). Given that the characteristics of tropical cyclones are now intrinsically determined in such an equilibrium, it allows us to study the sensitivity of mature tropical cyclones to environmental parameters.

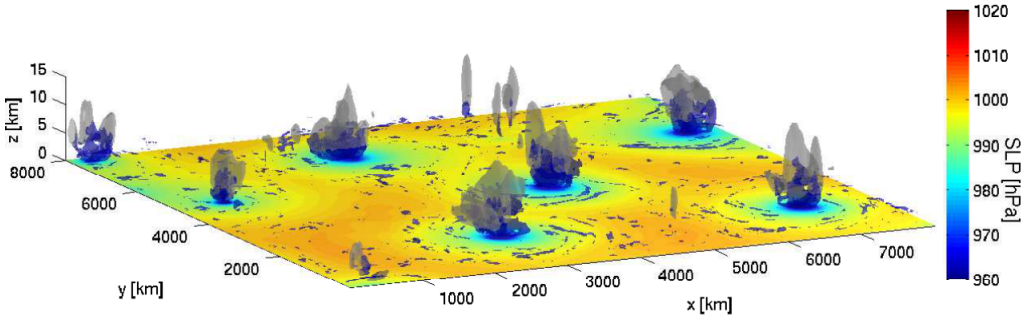

Figure 1.3: Rotating radiative-convective equilibrium simulated with the resolution and column physics of HiRAM at GFDL in a large domain. Surface shading: sea level pressure; Blue: liquid cloud; Gray: ice cloud.

With a small domain, one can study the genesis of tropical cyclone as the evolution of an idealized incipient vortex in favorable large-scale environment (Figure 1.4). Tropical cyclogenesis is one of the most intriguing yet poorly understood problems in tropical meteorology. Such an idealized framework allows one to study the dependency of tropical cyclogenesis on initial perturbation as well as large-scale environment parameters, such as, sea surface temperature (SST), vertical wind shear and environmental rotation.

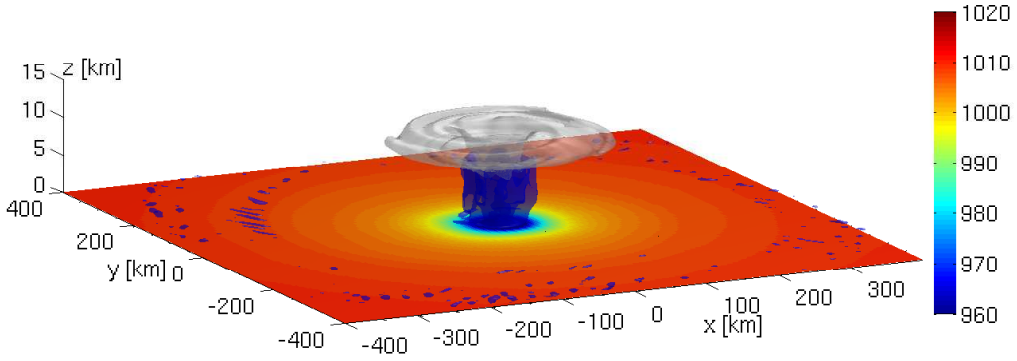

Figure 1.4: Rotating radiative-convective equilibrium simulated with the cloud-resolving model WRF in a small domain. Surface shading: sea level pressure; Blue: liquid cloud; Gray: ice cloud.

1.3 Outline

In this work, we study organized tropical convection in the framework of RCE simulated by both GCMs and CRMs (Table 1.1). Particularly, we seek to further our understanding of tropical cyclones and convective aggregation. The thesis is organized as follows:

Chapter	1 and 2	4	5
Topic	Matured tropical cyclones	Tropical Cyclogenesis	Self-aggregation of convection
Framework	RRCE with a large domain	RRCE with a small domain	Non-rotating RCE
Model	HiRAM fixed-SST/coupled SST	WRF/HiRAM	SAM/WRF

Table 1.1: Summary of thesis context and models in each Chapter.

In Chapter 2, motivated by HiRAM's success in tropical cyclone simulations, we achieve RRCE by coupling its column physics with rotating hydrostatic dynamics. A large doubly-periodic f-plane is used to allow multiple tropical cyclones to coexist. The sensitivity of tropical cyclones to environmental parameters is investigated in this idealized geometry with fixed SST. The parameter study helps in understanding the tropical cyclones simulated in the global model and also provides a reference point for future analogous studies with cloud resolving models.

In Chapter 3, we look at the effect of coupled SST on tropical cyclones by introducing a slab ocean model into RRCE. With coupled SST, we show that the eyewall region of tropical cyclones becomes cooler relative to the environment. The physics controlling the magnitude of this eyewall cooling are elucidated. We find that Potential-Intensity theory (Bister and Emanuel, 2002a) overestimates the impact of the eyewall cooling on the intensity of tropical cyclones and predicts a much weaker intensity compared to that in model simulations.

In Chapter 4, we explore the interactions between vertical shear, ambient rotation and thermodynamics during tropical cyclogenesis in a small doubly-periodic f-plane. Through idealized cloud-resolving simulations, we find that the sensitivity of tropical cyclogenesis to both the environmental rotation and thermodynamic state is affected by vertical shear. We show that such role of vertical shear is not fully represented in the analogous simulations with the resolution and column physics of HiRAM, which might affect the hurricane frequency simulated in the global simulation.

In Chapter 5, we investigate self-aggregation of convection by performing cloud-resolving simulations of non-rotating RCE with two CRMs, the System for Atmospheric Modeling (SAM) and the Weather and Research Forecasting Model (WRF). Self-aggregation is found to be sensitive to both the resolution and model. Such sensitivity adds complexity to the dependency of self-aggregation on SST and its implication on the variation of convective aggregation in the tropics with global warming.

In Chapter 6, we present a summary of our findings and discuss possible future directions.

Chapter 2

Rotating Radiative-Convective Equilibrium with fixed SST

This chapter is a reproduction of Zhou et al. (2014), except a few clarifying comments on references to literature that has appeared since the publication of that paper.

2.1 Introduction

Rotating radiative-convective equilibrium, achieved in a doubly periodic box on an f-plane with horizontally homogeneous forcing and boundary condition, is an informative idealized framework for studying the interactions between moist thermodynamics, radiation, and rotating dynamics. It can be studied in non-hydrostatic models in which deep convection is partly resolved and also in lower resolution hydrostatic models with parameterized convection. In the latter case, one can think of this framework as one of a hierarchy of idealized settings in which to study the implications of the assumptions made in GCMs.

Tropical cyclones (TCs) form within these rotating radiative-convective equilibria, and they provide simulations in which very long-lived mature TCs emerge. If run at the resolution and with the column physics (including boundary layer, radiation, microphysics, moist convection and cloud modules) of a global comprehensive model, this idealized framework

can help us evaluate the TC simulations in such models. Global models are moving to high enough resolution that aspects of their TC simulations are becoming more realistic, and these global models are one of the tools being used to try to predict the impact of climate change on TC statistics. Being able to study the model-generated TCs in this idealized geometry, eventually comparing to analogous simulations at cloud-resolving resolutions, should provide valuable information as to the limitations and strengths of the TC simulations in global models.

Held and Zhao (2008, hereafter HZ08) describe such a rotating radiative-convective equilibrium in which the column physics of a particular atmospheric model, GFDL's AM2 (Atmospheric Model version 2) is coupled to rotating hydrostatic dynamics in a doubly-periodic box. A similar equilibrium is achieved in Nolan et al. (2007) and Nolan and Rappin (2008) with higher cloud-resolving resolution in a study of tropical cyclogenesis. Schecter and Dunkerton (2009) and Schecter (2011) set up an idealized three-layer hurricane model under such a framework, with simplified radiative and convective parameterizations. The variability and predictability of hurricanes in rotating radiative-convective equilibrium is studied by Hakim (2011), Hakim (2013), and Brown and Hakim (2013) using both axisymmetric and three-dimensional models.

Besides their various choices for column physics and resolution, a major difference among these studies is that HZ08 considers a sufficiently large domain for multiple TCs to coexist while others use small domains within which only one TC develops. In those small-domain simulations, whether with a doubly-periodic domain or a rigid-wall box, the extent of TCs is explicitly set by the domain size. Because of this constraint, both the state of equilibrium achieved and its parameter sensitivity may be interfered with by the domain size. We refer to our doubly-periodic small-domain simulation as *lattice* equilibrium, in which duplicated TCs exist simultaneously at the grid points in a lattice that can be visualized by duplicating the doubly-periodic domain along its boundaries. The large-domain simulations avoid such finite-domain effects and can be regarded as *turbulent* equilibria in the sense that multiple

TCs interact with respect to each other in more complex ways. The extent of TCs is thus controlled by internal processes of the turbulent equilibrium instead of domain size. This allows for analysis of size and intensity of TCs as a function of environmental parameters, independent of domain size. Neither configuration is realistic in the sense that appropriate decay mechanisms (poleward drift and interactions with land and extratropical systems) and suppression factors (wind shear, subsidence and dry air entrainment) are not present, resulting in very long-lived storms.

In this study, both lattice and turbulent equilibria are achieved in doubly-periodic domains with column physics and resolution of a high-resolution global atmospheric model (HiRAM) at GFDL. Our study differs from the analogous work of HZ08 in that HiRAM has better simulations of hurricane compared to AM2, due to a higher horizontal resolution and modified convective parameterization (Zhao et al., 2009). Also, we investigate the dependency on the domain size systematically. The details of model formulation are presented in Section 2.2. We start by describing turbulent equilibrium achieved in a large domain (2×10^4 km on a side) in Section 2.3. The parameter sensitivity of TC structure and intensity in this turbulent equilibrium is studied by varying sea surface temperature, ambient rotation rate f and surface drag coefficient C_D. In Section 2.4, we explore the variation of lattice equilibrium as a function of domain size, and show how the natural extent of TCs in turbulent equilibrium is related to this domain size dependency of lattice equilibrium. A discussion and conclusion are offered in Section 2.5.

2.2 Model configuration and experiments setup

The column physics used here is that of HiRAM (GFDL High Resolution Atmospheric Model). HiRAM has been used in Zhao et al. (2009) to realistically simulate the observed global climatology and interannual variability of hurricane frequency at 50 km resolution, although few storms are simulated higher than category 2 as measured by the maximum sur-

face winds, especially in the N.Atlantic (Zhao and Held, 2010). Multiple simulations of the period 1979-2008, running over observed sea surface temperatures, with both 50 km and 25 km resolution versions of this model have been placed in the CMIP5 (Climate Model Intercomparison Project Version 5) archive. The seasonal and interannual variability of tropical storm genesis is not fundamentally different in the 25 and 50 km models. A 25 km version of the model with modified surface flux formulation and microphysics scheme has shown impressive skill for seasonal forecasts in the Atlantic (Chen and Lin, 2012).

HiRAM was developed starting from an earlier lower resolution model, AM2 (GAMDT, 2004). The prognostic cloud fraction scheme is changed to a simpler diagnostic scheme assuming a sub-grid scale distribution of total water. The relaxed Arakawa-Schubert convective closure (Moorthi and Suarez, 1992b) in AM2 has been replaced by a modified shallow convection scheme (Bretherton et al., 2004; Zhao et al., 2009), which results in a larger fraction of precipitation occurring at resolved scale rather than through the parameterization. All other physical schemes are the same as in AM2. Surface fluxes are computed using Monin-Obukhov similarity theory, with a gustiness component (1 m s^{-1}) to account for contribution from sub-grid wind fluctuation. For vertical diffusion, a K-profile scheme designed for cloud-topped boundary layers, with parameterized entrainment rates at the top of the boundary layer (Lock et al., 2000) is used. Stability functions with thresholds dependent on Richardson number are adopted for stable layers. We refer the reader to GAMDT (2004) and Zhao et al. (2009) for further details.

The doubly-periodic model has the same vertical level altitudes as the GCM with the lowest level at about 35 m. The horizontal resolution is 25 km. As in HZ08, there is no diurnal or seasonal cycle in the doubly periodic model, and the radiative forcing is configured using an equatorial annual mean solar zenith angle. Sea surface temperatures (SSTs) are homogeneously prescribed over a saturated (ocean) surface. Aerosols are absent in the atmosphere, while the stratospheric ozone is fixed at an observed tropically-averaged vertical profile.

2.3 Varying environmental parameters in turbulent equilibrium

Turbulent equilibrium is achieved using a large domain $(2\times10^4$ km$)^2$. The initial condition is an observed tropically-averaged temperature profile, with moisture artificially near saturation below 100 hPa. We have seen no indication in this rotating system of a dependency of the final equilibrium state on the initial condition (Unlike the non-rotating system of Chapter 5). The model is integrated 2.5 years to its equilibrium. Most statistics, such as hydrological balance, do not require this long an integration. After the initial genesis period a qualitative equilibrium is typically achieved in a few months, but the number of TCs usually decreases slowly with time until it is finally stable. For every 3-hourly output during the last 6 months of each simulation, TCs are collected by identifying points with surface pressure p_s satisfying two criteria: 1) p_s is less than a critical value of 990 hPa, and 2) p_s is a minimum at this point within the surrounding 10×10 grid box.

We first look at the sensitivity to SST, with ambient rotation rate set at 20°N. Snapshots of surface wind speed for two different SSTs are compared in Figure 2.1. As found in HZ08, the number of TCs decreases with SST. There are about 40 TCs within the domain for SST at 297 K but only about 15 TCs for SST at 305 K. The distribution of TC central surface pressure is shown in Figure 2.2a. The peak frequency of TC central surface pressure shifts towards a lower value as SST increases, indicating consistent higher intensity at warmer SST. The mean central surface pressure intensifies by about 3 hPa K^{-1} and the mean maximum surface wind speed (the wind in the lowest model layer, at roughly 35 m) increases roughly 1.5 m s^{-1} K^{-1} (Figure 2.3a and 2.3b). This is comparable to the sensitivity found in the global model, which indicates roughly a 4 m s^{-1} increase in the mean maximum surface wind between the case with climatological SST and that with 2 K increases in SST (Zhao and Held, 2010). This suggests that we may be able to study intensity change in response to SST .

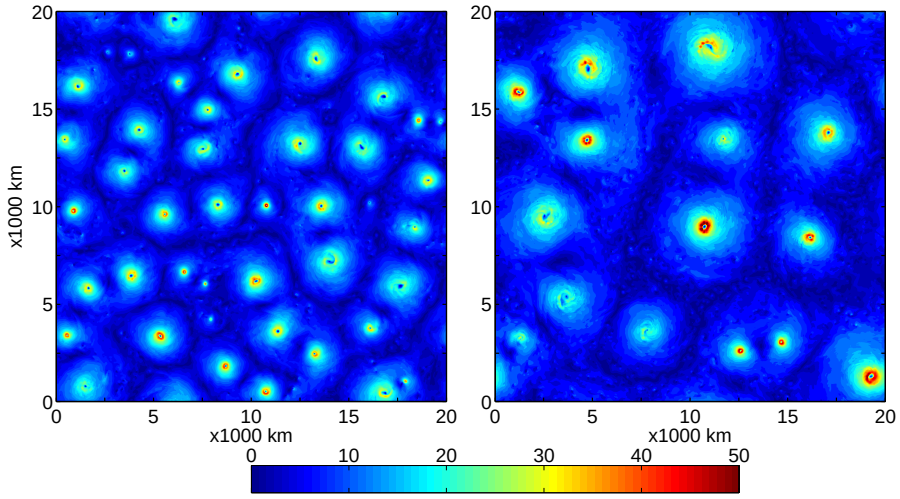

Figure 2.1: Snapshots of surface wind (m s^{-1}) for different sea surface temperatures. (left) SST= 297 K; (right) SST = 305 K. f is set at 20°N.

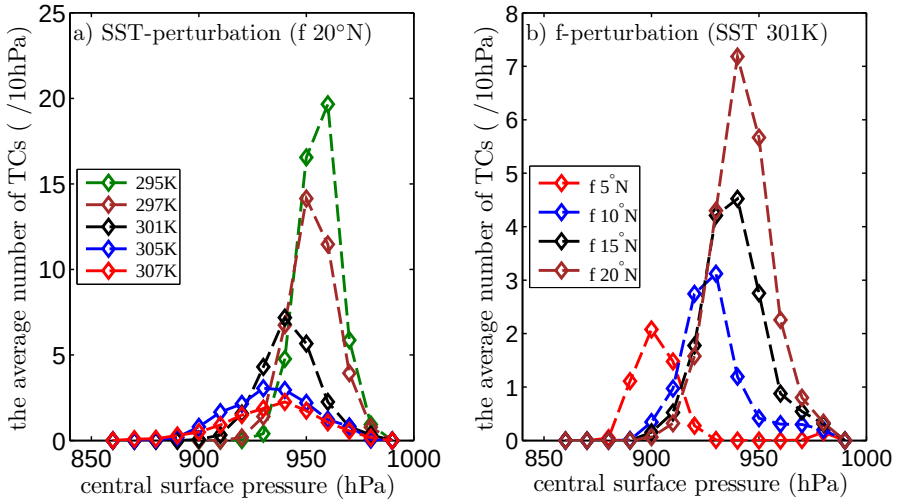

Figure 2.2: (a) The average number of TCs in the domain with their central surface pressures within the specified 10 hPa interval as a function of SST with f at 20°N. (b) As in (a), but for the sensitivity to f with SST fixed at 301 K. For both sets of experiments, surface exchange coefficients are calculated from Monin-Obukhov scheme.

Potential intensity (PI) is computed from the time- and domain-mean thermodynamic profiles, following Bister and Emanuel (2002b). Besides the environmental thermodynamic profile, the theory also requires choices regarding the moist adiabat, the inclusion of dissipative heating, and the rate of surface exchange coefficients. We choose the option of pseudo-adiabatic ascent and include dissipative heating (as in the GCM, the kinetic energy

dissipation in the boundary layer is returned as heat within the boundary layer). The ratio of surface exchange coefficient for enthalpy C_k to surface drag coefficient C_D is set at 0.6, to be consistent with the ratios produced in the model. A velocity reduction factor of 0.72 is applied as a way to extrapolate down through the frictional boundary layer. The theoretical maximum wind speed captures the slope of intensification with SST quite well except for very low SSTs (Figure 2.3). The explanation for this mismatch at lower SSTs may be that over such cold SST TCs are too weak to compete with random convection and have difficulty in maintaining their mature state.

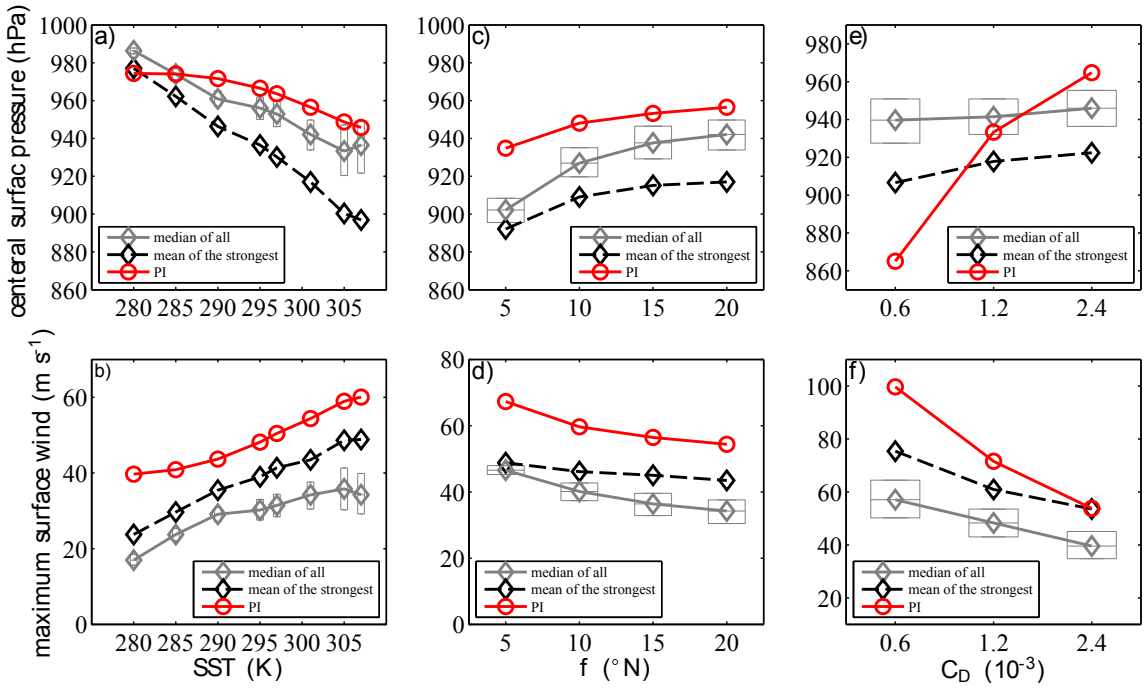

Figure 2.3: TC intensity and PI as function of SST (left), f (middle) and C_D. The gray line shows the median of all collected TCs. The first and third quartiles are indicated by the gray box. The black line shows the mean of the strongest storms at each instant of time. The red line shows the estimate from PI theory.

The sensitivity to ambient rotation rate f is investigated by varying f from 5°N to 20°N with fixed SST at 301 K. Snapshots of surface wind for f at 5°N and 20°N are compared in Figure 2.4. As found in HZ08, the number of TCs increases with ambient rotation rate. There are about 23 TCs within the domain for f at 20°N but only about 5 TCs for f at

5°N. The peak frequency of TC central surface pressure shifts towards higher value as f increases, indicating weaker intensity at larger f (Figure 2.2b). As f increases from 5°N to 20°N, the mean central surface pressure (Figure 2.3c) increases by 30∼40 hPa, and by the same measures the mean maximum surface wind (Figure 2.3d) decreases by 5∼10 m s^{-1}.

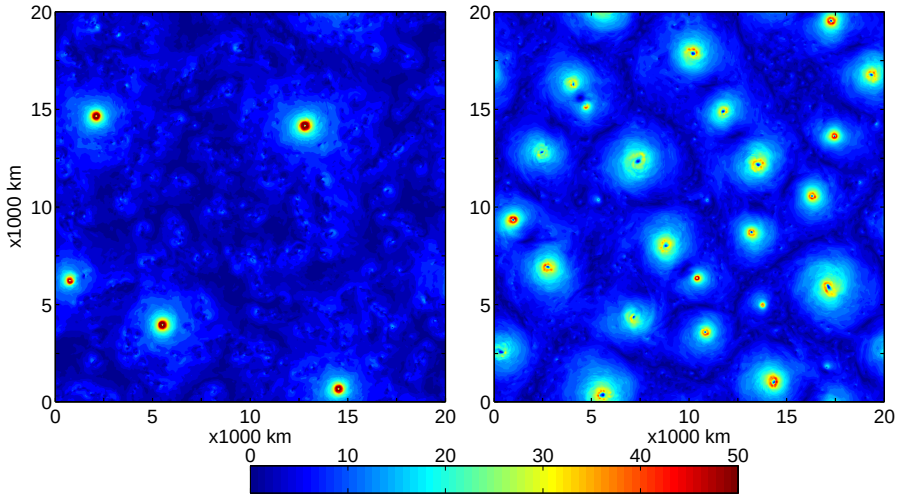

Figure 2.4: Snapshots of surface wind (m s^{-1}) for different ambient rotation rates with SST fixed at 301 K. (left) f at 5°N; (right) f at 20°N.

The difference in vertical profiles of temperature and specific humidity show a moister and warmer environment for larger ambient rotation rate (Figure 2.5). The increasing air temperature and humidity at the surface corresponds to a reduced surface moisture disequilibrium. The domain-averaged evaporation and precipitation do not change substantially, as expected from the close balance between radiation cooling and latent heat flux, but the average surface wind speed increases due to the increased density of TCs. We interpret the reduction in surface disequilibrium as determined by the need to maintain the same strength of hydrological cycle in the presence of stronger mean surface wind. The increasing of temperature is amplified upward, approximately following a moist adiabat. The pattern of temperature and humidity differences also indicates more aggressive shallow convection in the cases with larger ambient rotation rate. The potential intensity computed from this vertical profile satisfactorily captures the decreasing intensity with increasing f.

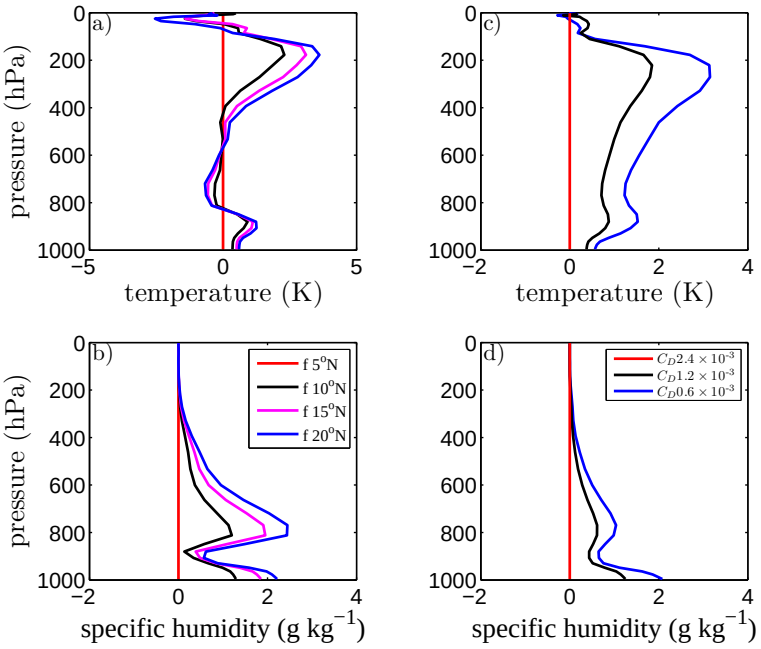

Figure 2.5: Differences in vertical profiles of temperature and specific humidity between (a, b) different f (vs 5°N case) with surface exchange coefficients calculated from Monin-Obukhov scheme; and (c, d) different C_D (vs 2.4x10^{-3} case) with f at 15°N and SST fixed at 301 K.

To study the sensitivity to surface drag coefficient, we bypass the Monin-Obukhov scheme in the model and prescribe surface exchange coefficients homogeneously within the domain. The surface drag coefficient C_D is varied from 0.6×10^{-3} to 2.4×10^{-3}, while the surface exchange coefficient for enthalpy C_k is fixed at 1.2×10^{-3}. Three sets of experiments are conducted with ambient rotation rate set at 10°N, 15°N and 20°N. The distribution of TC central surface pressure is shown in Figure 2.6. Interestingly, this curve shifts with C_D in opposite direction for different rotation rates. For smaller C_D, there are more intense TCs with f set at 10°N but more weak TCs with f set at 20°N. In spite of this difference, the number of TCs within the domain decreases with C_D in all three cases (as can be seen in Figure 2.6).

The sensitivity of TC intensity to C_D is summarized in Figure 2.3e and 2.3f, with ambient rotation rate chosen at 15°N. As C_D decreases from 2.4×10^{-3} to 0.6×10^{-3}, the mean central surface pressure intensifies by only about 10 hPa and the mean maximum surface wind

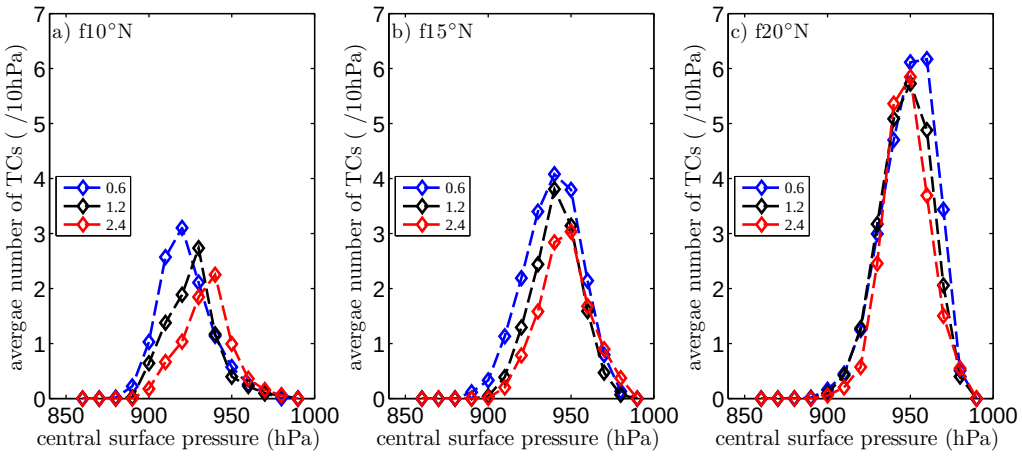

Figure 2.6: (a) The average number of TCs in the domain with their central surface pressures within the specified 10 hPa interval as a function of surface drag coefficient C_D (0.6, 1.2, 2.4 $\times 10^{-3}$) with f at 10°N. (b) (c) As in (a), but with f at 15°N and 20°N. C_k is fixed at 1.2×10^{-3} and SST is 301 K.

increases by roughly 50%. The difference in vertical profiles of temperature and specific humidity are shown in Fig 2.5, indicating a warmer and more humid environment for smaller C_D, similar to the cases with larger f. The potential intensity computed from this vertical profile shows a stronger sensitivity to C_D compared to the model results, especially for potential pressure intensity. Modifying the ambient rotation rate does not change this result. We note that the recent modification to PI theory by Emanuel and Rotunno (2011) weakens the sensitivity to C_D.

The mean radius-height structure of the strongest TC within the domain for two SSTs is shown in Figure 2.7. The boundary layer inflow and upper-tropospheric outflow characteristic of tropical cyclones is apparent, with an ascent region just inside of the radius of maximum surface wind (R_{mw}).

As shown in Figure 2.8, R_{mw} increases with SST, decreases with C_D and increases with f for small f (but saturates and probably decreases as f is increased further). The strongest storms that form for a given parameter setting have the smallest R_{mw}s. R_{mw}s simulated in this 25-km model are substantially larger than those observed (Stern and Nolan, 2012). However we feel that the systematic variation seen in this model is of interest for comparison with

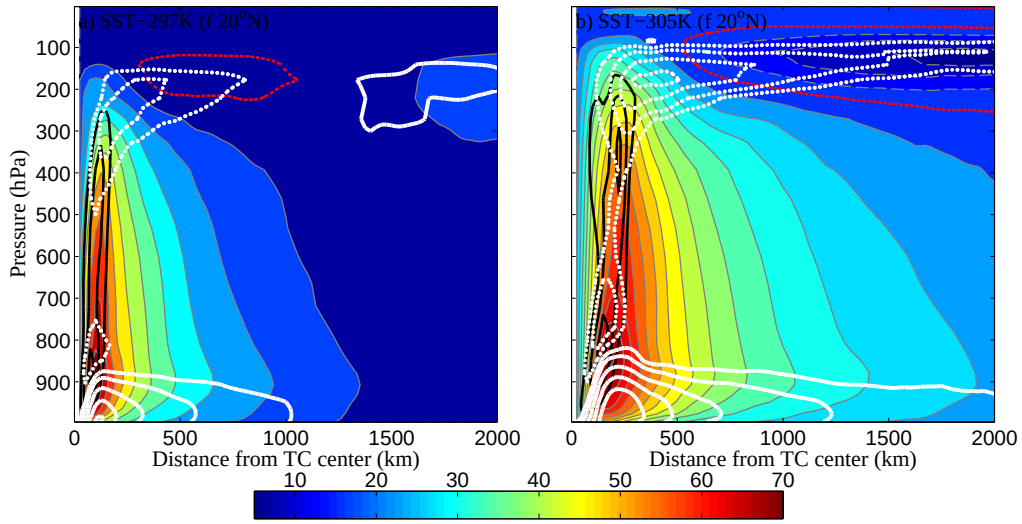

Figure 2.7: Time- and azimuthal-mean tangential (colors), radial (white) and vertical (black) velocities of the strongest tropical cyclone for sea surface temperature a) 297 K and b) 305 K with f at 20°N. Tangential winds are contoured at every 5 m s^{-1}. Positive (cyclone) values are solid, negative (anticyclone) values are dashed, and the zero contour is a red dashed line. Radial winds are contoured at [2, 5, 10, 15, 20] m s^{-1}. Positive (outflow) values are dashed, negative (inflow) values are solid. Vertical velocity is contoured (negative only) at [-1, -2, -3] Pa s^{-1}.

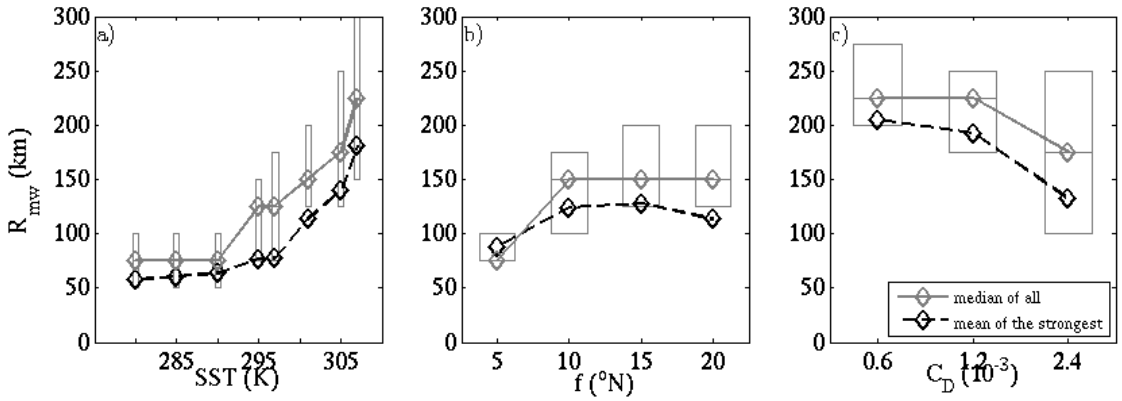

Figure 2.8: The radius of maximum surface wind (R_{mw}) as a function of SST (a), f (b) and C_D (c). The gray line is the median of all collected TC. The first and forth quartiles are indicated by the gray box. The black dash line shows the mean of the strongest storms at each instant of time.

high resolution simulation. We return to these results in Section 2.4 where quantitatively different results are obtained in smaller domains containing only one storm.

HZ08 explored the sensitivity of the natural extent of TCs to SST and f in the turbulent multi-storm equilibrium. With a higher resolution and a larger domain size, we hope to have a better estimate of this sensitivity. As shown in Figure 2.9, the average number of TCs, n, doubles or halves as SST is perturbed by 4 K from the reference SST (301 K) and increases nearly linearly with f. We estimate the natural extent of TCs (r_0) as

$$r_0 = \sqrt{\frac{A}{n}} \tag{2.1}$$

in which A is the domain area. Two simple theoretical scalings are considered for the size of tropical cyclones. One is the Rossby radius of deformation NH/f, and the other is a natural length scale from PI theory V_p/f, where V_p is the potential intensity (Emanuel, 1986). However, as shown in Figure 2.9, while both of these two scalings project the right trend, neither satisfactorily captures the sensitivity. Modifying some of the choices in the computation of potential intensity, or using actual model intensities for the V_p/f scalings does not affect this conclusion. We will return to this topic in Section 2.4.

2.4 Varying domain size

The sensitivity of rotating radiative-convective equilibrium to domain size is investigated by varying the domain size from $(1.25\times10^3$ km$)^2$ to $(1.25\times10^4$ km$)^2$, with SST at 301 K and f at 10°N. The composites of surface wind for different domain sizes are shown in Figure 2.10. When the domain is small, only one tropical cyclone develops. The tropical cyclone has some elasticity in the sense that it can expand to fill the domain until multiple storms finally appear. Particularly, the extent of the single TC in the $(7.5\times10^3$ km$)^2$ domain is nearly 20% larger than the natural extent of TCs in the $(1.25\times10^4$ km$)^2$ domain.

The behavior of TCs evolves through four regimes, as illustrated by the time series of minimum surface pressure in each simulation (Figure 2.11). When the domain is very small, only a tropical depression, with its central surface pressure at about 980 hPa, develops

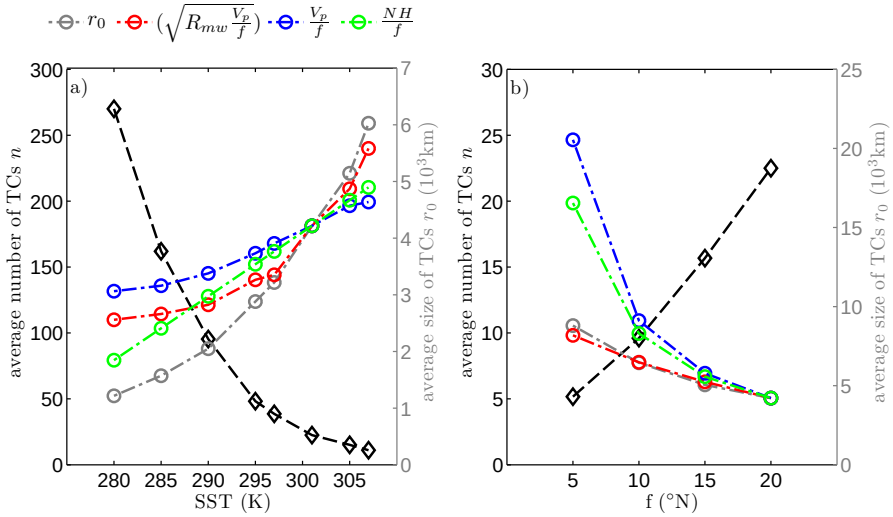

Figure 2.9: (a) The average number of TCs n (black-dash line with diamond) and the natural extent of TCs r_0 ($\sqrt{\frac{A}{n}}$, gray dash-dot line with circle) as a function of SST. Ambient rotation rate f is set at 20°N. Three possible scalings are shown. Red line: $\sqrt{R_{mw}\frac{V_p}{f}}$; blue line: $\frac{V_p}{f}$; green line: $\frac{NH}{f}$. (b) As in (a) but for the variation of ambient rotation rate f . The underlying SST is 301 K. The estimates from these three scalings are normalized to the natural extent of TCs with SST at 301 K and f at 20°N.

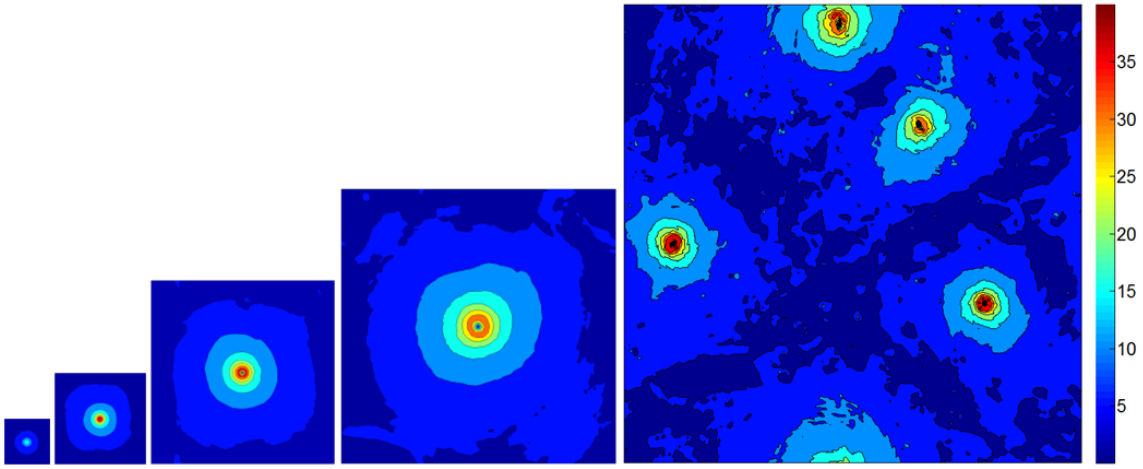

Figure 2.10: Composite of surface wind for simulations with domain sizes at 1250 km, 2500 km, 5000 km, 7500 km and snapshot of surface wind for domain size at 12500 km, all with SST at 301 K and f at 10°N.

within the domain. As the domain size increases, the depression evolves into an intermittent tropical cyclone with intensity varying widely over a cycle of approximately 50 days. Further

increase of the domain size avoids this collapse to weak intensity and leads to a sustained storm. Eventually, if the domain size becomes sufficiently large, multiple storms coexist.

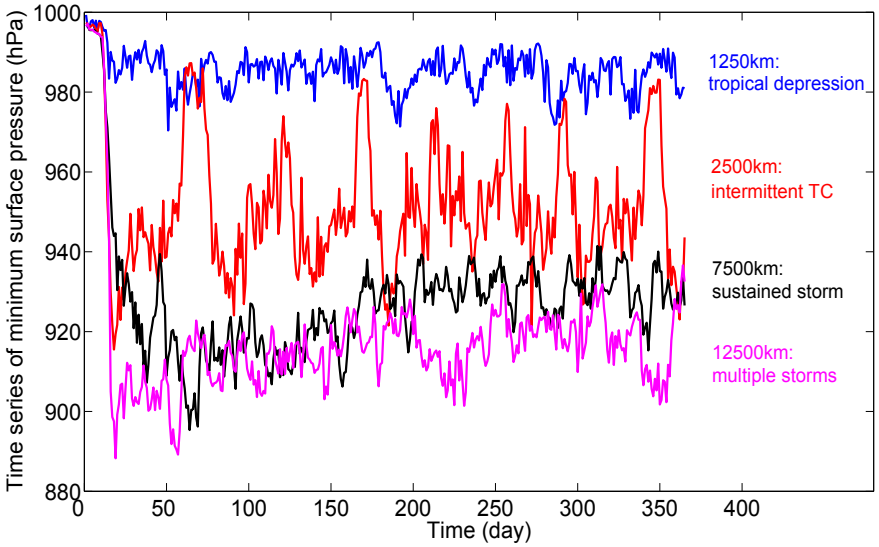

Figure 2.11: Time series of minimum surface pressure for different regimes. SST is 301 K and ambient rotation rate f is fixed at 10°N.

To see how the natural extent of TCs in turbulent equilibrium is related to this regime behavior, we conduct two series of experiments with : 1) different f at 5°N, 10°N and 20°N with SST at 301 K, and 2) different SST at 301 K and 305 K with f at 10°N. The time-mean central surface pressure is summarized in Figure 2.12a and 2.12b respectively. The intensity first increases with domain size and then levels off approximately at the beginning of the regime of a single sustained storm (marked with an O symbol). This regime shifts towards large domain size as SST increases or f decreases, the same as the natural extent of TCs in turbulent equilibrium. For different parameter settings, the natural extent of TCs in turbulent equilibrium (marked with a | symbol) always falls in this regime. The following simple picture is consistent with these results: If the number of TCs increases from its equilibrium value, the available space for a given TC must decreases into the intermittent storm regime. This TC become unstable, and is more likely to be eliminated by competition with surrounding storms when sufficiently weak. The number of TCs then returns to its

equilibrium value. On the other hand, if the number of TCs decreases, the suppression effect of TCs on its surrounding area becomes weak as TCs expand. With fewer but larger TCs randomly moving around, there is more free space for TC genesis. These two effects favor new TC genesis and bring the number of TCs back to its equilibrium.

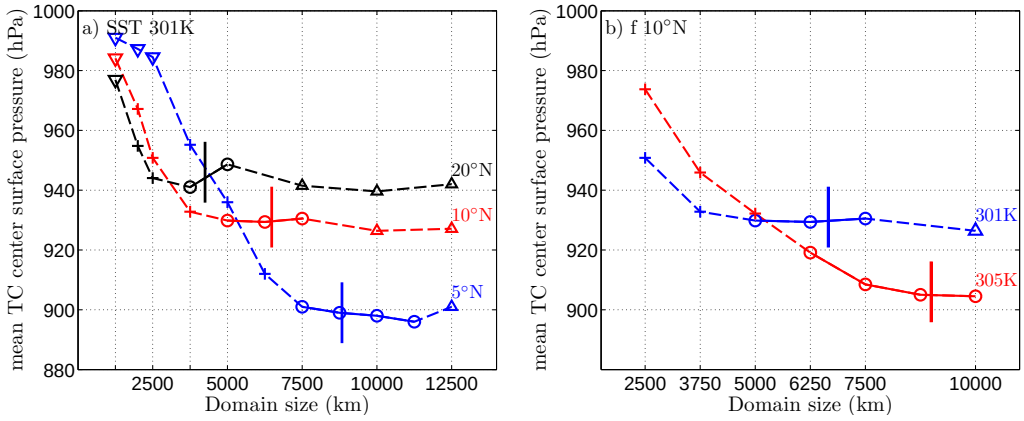

Figure 2.12: Time mean TC central surface pressure as a function of domain sizes at (a) different ambient rotation rates and (b) sea surface temperatures. The four regimes mentioned above are marked with different symbols, ∇ (tropical depression), $+$ (intermittent storm), $\circ$ (sustained storm) and $\triangle$ (multiple storms). The average scale of TCs in corresponding large domain simulation is marked with a $|$ symbol.

One explanation for this regime of a sustained storm is that the available space for TCs needs to be sufficiently large to provide enough angular momentum to support the inner vortex. In addition to the two scales mentioned in Section 2.3, a third candidate for the natural extent of TCs then comes up by relating the angular momentum at the outer radius r_0 to that at R_{mw}. For a reduction factor α between these two, this relationship can be written as $V_p R_{mw} = \frac{\alpha}{2} f r_0^2$. Assuming this reduction factor α is nearly invariant when SST or f varies, we have $r_0 \sim \sqrt{R_{mw}\frac{V_p}{f}}$. This is essentially the same relationship between R_{mw} and r_0 as in Emanuel and Rotunno (2011). As shown in Figure 2.9, this scaling nicely captures the variation of r_0 with both SST and f except at very low SSTs. As we mentioned previously, the equilibrium achieved at very low SSTs, with a large number of weak TCs, looks very different from those with higher SST. The above argument may only apply to the cases where mature storms dominate. This parameter fit is a good description of the model

results. However this relationship between r_0 and R_{mw} does not in itself provide a theory for r_0 or R_{mw}.

The variation of R_{mw} with parameters (SST, f and C_D) in lattice equilibrium, with domain size at 5000 km, is shown in Figure 2.13. R_{mw} increases with f and decreases with SST and C_D. This result is consistent with that of Schecter and Dunkerton (2009) in which a three-layer tropical cyclone model is used, but different from what we found in turbulent equilibrium, for SST in particular (Figure 2.8). The parameter sensitivity of R_{mw} in lattice equilibrium reflects the parameter sensitivity of the ratio between R_{mw} and TC extent r_0, since in a fixed size small domain r_0 is fixed, while the parameter sensitivity of R_{mw} in turbulent equilibrium takes into account both the parameter sensitivity of this ratio and that of r_0. As we discussed in Section 2.3, TC extent r_0 can vary significantly with parameters in turbulent equilibrium. In this interpretation, the increase of r_0 with SST dominates over the decrease of $\frac{R_{mw}}{r_0}$ and results in increasing R_{mw} with SST in turbulent equilibrium (Figure 2.8a), while the decrease of r_0 with f may offset the increase of $\frac{R_{mw}}{r_0}$ and leads to saturation or even decrease of R_{mw} for large f in turbulent equilibrium (Figure 2.8b).

2.5 Conclusions

Idealized models can be used to help fill the gap between theory and comprehensive climate model efforts. In much recent work, the spherical geometry is held fixed while the column physics and/or surface boundary condition are largely simplified. Instead, we choose to retain the column physics and simplify the geometry and surface boundary conditions. By coupling the column physics to the hydrostatic dynamics in a doubly-periodic domain, we can obtain a homogeneous doubly periodic rotating radiative-convective framework.

This study is along the line of Held and Zhao (2008), with the column physics of AM2 replaced by that of a mesoscale resolution global atmospheric model, HiRAM, which produces

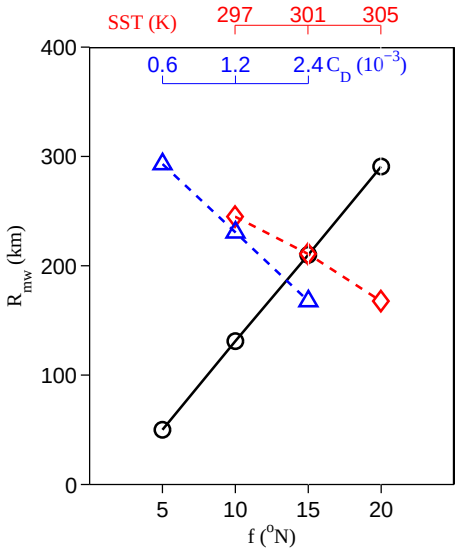

Figure 2.13: Sensitivity of R_{mw} to f (black line), SST (red line) and C_D (blue line) in a fixed-size small domain (5000 km on a side). In f and C_D perturbation experiments, SST is fixed at 301 K. In SST and C_D perturbation experiments, ambient rotation rate is set at 15°N.

quite realistic TC climatology when run with realistic boundary condition. A large domain $(2\times10^4$ km$)^2$ is used to obtain turbulent multi-storm equilibria. The parameter sensitivity is then studied by varying sea surface temperature, ambient rotation rate f and surface drag coefficient C_D. The mean TC intensity increases with SST and decreases with f and C_D. The potential intensity (Bister and Emanuel, 2002b) calculated from the thermodynamic environment captures the sensitivity to SST and f with reasonable accuracy but overestimates that to C_D, especially in terms of central surface pressure. Note that PI theory in itself doesn't depend on f so an understanding of the dependence of the intensity on f requires a theory for the sensitivity of the model's equilibrated thermodynamic profiles to f.

The natural extent of TCs, r_0, in turbulent equilibrium increases with SST and decreases with f. Although we have some difficulty in estimating r_0 by simple theoretical scalings, we find it related to a shift in the regime behavior of lattice equilibrium, from an unsteady to a relatively stable mature storm.

In turbulent equilibrium, the radius of maximum surface wind (R_{mw}) increases with SST, increases with f for small f but saturates or probably decreases as f is increased further. However in lattice equilibrium, R_{mw} decreases with SST and keeps increasing with f. This is because TC extent r_0 is constrained by the domain size in lattice equilibrium while in turbulent equilibrium r_0 varies systematically with environmental parameters. It is the relationship between R_{mw} and r_0 that is robust to change in domain size. Because of the poor resolution of the R_{mw} in this model, the results on the parameter sensitivity of R_{mw} are necessarily tentative.

We believe that simulations of rotating radiative-convective equilibrium such as these, with the resolution and column physics of a global atmospheric model being used to study the response of TCs to climate change, can provide a needed middle ground between the global model and non-hydrostatic cloud-resolving simulations in an idealized geometry that will help in establishing the strengths and limitations of the global simulations. Current computer resources still preclude systematic comparisons between cloud-resolving models and GCM column physics in RRCE. However, Khairoutdinov and Emanuel (2013) is a first attempt, using an unphysically large value of f to make the storm smaller and allow multiple storms to form in the domain. The qualitative similarity with the present study is encouraging. The domain-size dependency of some of the parameter sensitivities in our results implies that care needs to be taken when comparing to cloud-resolving simulations in small domains.

Chapter 3

Rotating Radiative-Convective Equilibrium with coupled SST

3.1 Introduction

In Chapter 2, we have studied the parameter sensitivity of tropical cyclones in the framework of rotating radiative-convective equilibrium with fixed SST. By prescribing a horizontally homogeneous SST over the domain, one however neglects the response of SST to tropical cyclones. It is well-known that tropical cyclones can induce substantial cooling at the surface along their paths, which in turn can have a profound impact on TC intensity (Leipper, 1967; Bender et al., 1993; Schade and Emanuel, 1999; Shen and Ginis, 2003; Zhu and Zhang, 2006; Lin et al., 2013). Shen and Ginis (2003) shows that the cooling is dominated by the effect of internal ocean dynamics in the deep and open ocean regions but by surface fluxes in the near-coastal shallow ocean regions. In this study, we achieve RRCE with the column physics of the High-resolution Atmospheric Model (HiRAM) at GFDL following the line of Zhou et al. (2014), but with the atmosphere coupled to a simple slab ocean layer. The sensitivity of tropical cyclones to the slab ocean layer is then studied by varying the layer depth H. By using a simple slab ocean layer, only the effect from surface fluxes is included. However,

we feel that it is the natural place to start when approaching the problem of RRCE with interactive SST.

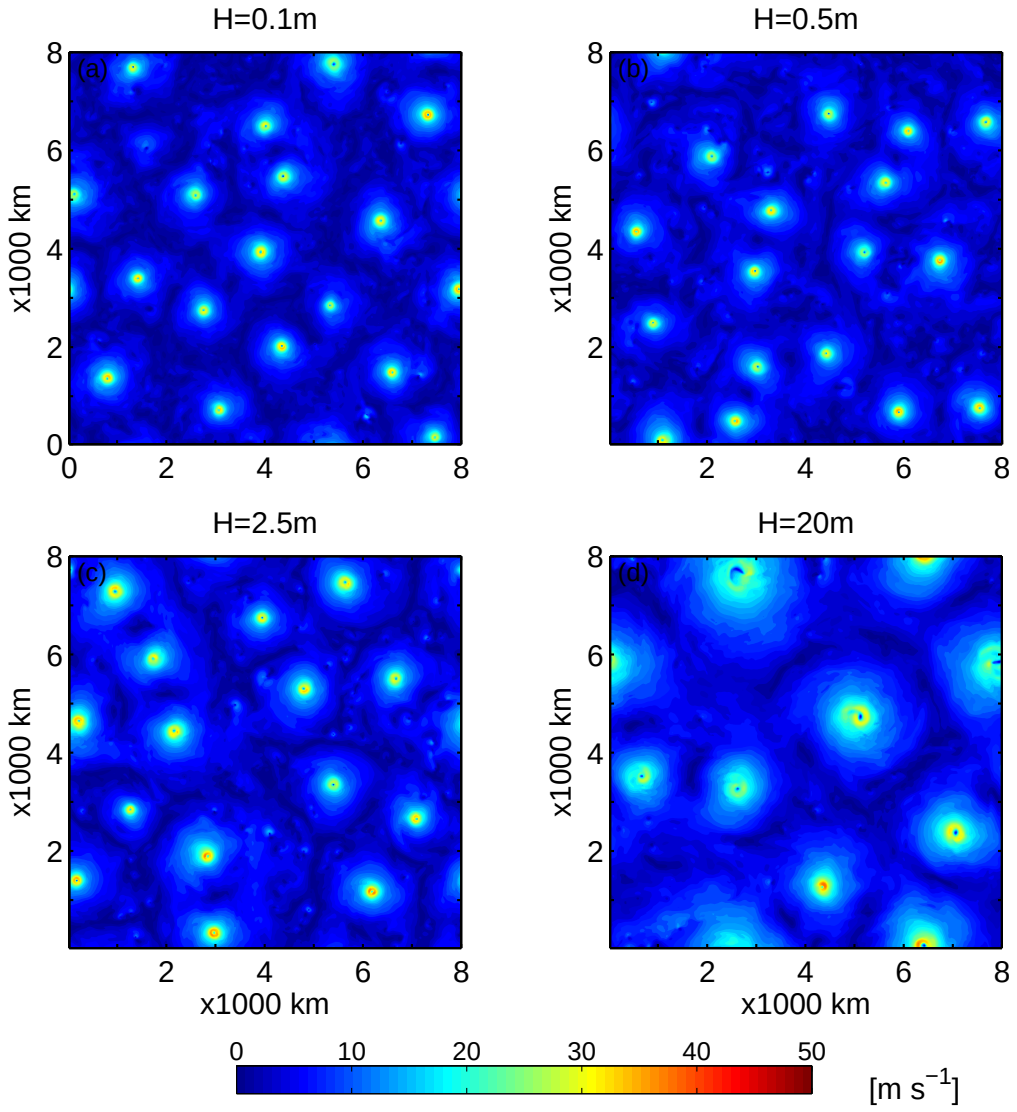

Figure 3.1: Snapshots of instantaneous surface winds (m s^{-1}) for simulations with (a) H=0.1 m, (b) H=0.5 m, (c) H=2.5m and (d) H=20m.

The Chapter is organized as follows: The model configuration and experiments are described in Section 3.2. We briefly depict the achieved RRCE with coupled SST in Section 3.3. The physics for the eyewall cooling is studied in Section 3.4. The variations of the intensity and structure of tropical cyclones with H are investigated respectively in Section 3.5 ans 3.6. Conclusions are offered in Section 3.7.

3.2 Model Configuration and Experiments

We achieve rotating radiative-convective equilibrium (RRCE) by coupling the column physics of the High-resolution Atmospheric Model at GFDL (HiRAM) to rotating hydrostatic dynamics in a doubly-periodic domain. HiRAM has been used in Zhao et al. (2009) to realistically simulate the observed global climatology and interannual variability of hurricane frequency. The atmospheric model used in this study has 32 vertical levels with the lowest level at about 35 m. The horizontal resolution is 25 km. The GFDL interactive radiation scheme is used for radiative processes with no diurnal or seasonal cycle. The cloud fraction is estimated by a simple diagnostic scheme assuming a sub-grid scale distribution of total water. A shallow convection scheme (Bretherton et al., 2004; Zhao et al., 2009) is used for parameterized convection, with entrainment rate optimized for the global simulation. Surface fluxes are computed using Monin-Obukhov similarity theory, with a gustiness component of 1 m s^{-1}. The vertical diffusion is handled by a K-profile scheme (Lock et al., 2000). A large domain (8000 km x 8000 km) is used to allow multiple storms to exist simultaneously.

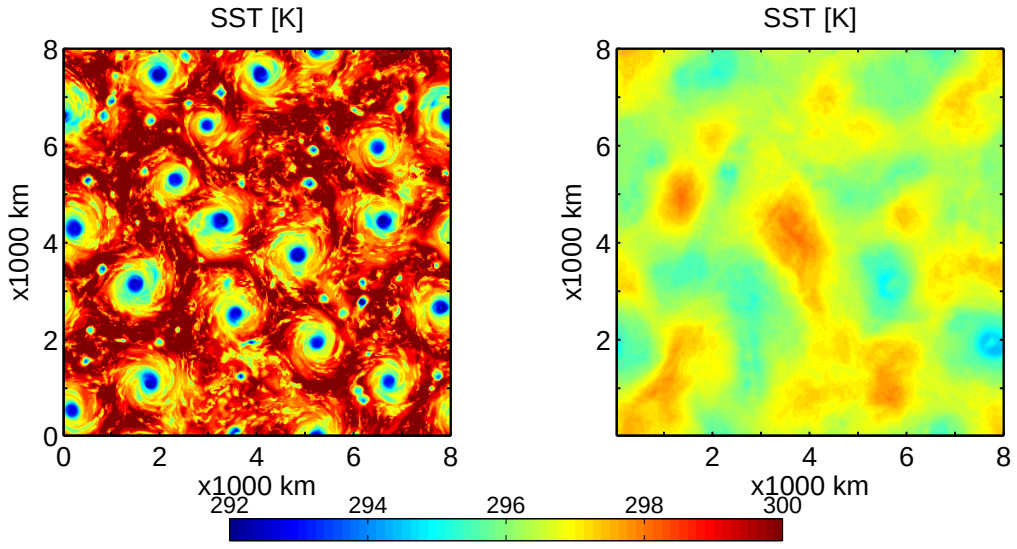

Figure 3.2: Snapshots of instantaneous sea surface temperature (K) for simulations with H=0.1 m (left) and H=20 m (right).

Unlike previous RRCE studies (Held and Zhao, 2008; Khairoutdinov and Emanuel, 2013; Zhou et al., 2014) which prescribe a fixed SST homogeneously over the domain, a slab ocean layer is used to predict the SST, such that at each grid point we have

$$\frac{\partial SST}{\partial t} = \frac{F_s}{\rho_w C_{pw} H} \tag{3.1}$$

where ρ_w is the density of water, C_{pw} is the heat capacity of water, H is the depth of the ocean layer and F_s is the net surface energy flux into the ocean. The incoming solar radiative flux is tuned using an annual-mean zenith angle corresponding to latitude 35° such that the simulated SST is close to the observed tropical-mean value.

The sensitivity of tropical cyclones to the underlying heat capacity is investigated by varying the depth H from 0.1 m to 20 m. We first achieve an equilibrium with a layer depth of 1.25 m and then restart from this equilibrium with different depths for another 10 years to reach full equilibrium. For comparison, one additional simulation is conducted with fixed SST. The fixed SST is set at 296.35 K by extrapolating the simulated domain-mean SST along the axis of H^{-1} (see Figure 3.4). The output at every three hours from the last four months is used for analysis. Tropical cyclones are identified over the domain by finding points with surface pressure satisfying two criteria: 1) less than a critical value of 990 hPa, and 2) a minimum at this point within the surrounding 10×10 grid box.

3.3 Description

Similar to RRCE with fixed SST, the domain still fills up with long-lived tropical cyclones (Figure 3.1). One distinct difference from RRCE with fixed SST is that the eyewall region of tropical cyclones is now cooler relative to the environment (Figure 3.2). The magnitude of the eyewall cooling increases as H decreases. With H=0.1 m, SST in the eyewall region is about 7 K cooler compared to that in the environment. The cooling at the surface extends upward and produces a shallow cold core under the typical warm core of tropical cyclones

(Figure 3.3). It is interesting that that tropical cyclones are still able to sustain themselves despite the substantial cooling at the eyewall.

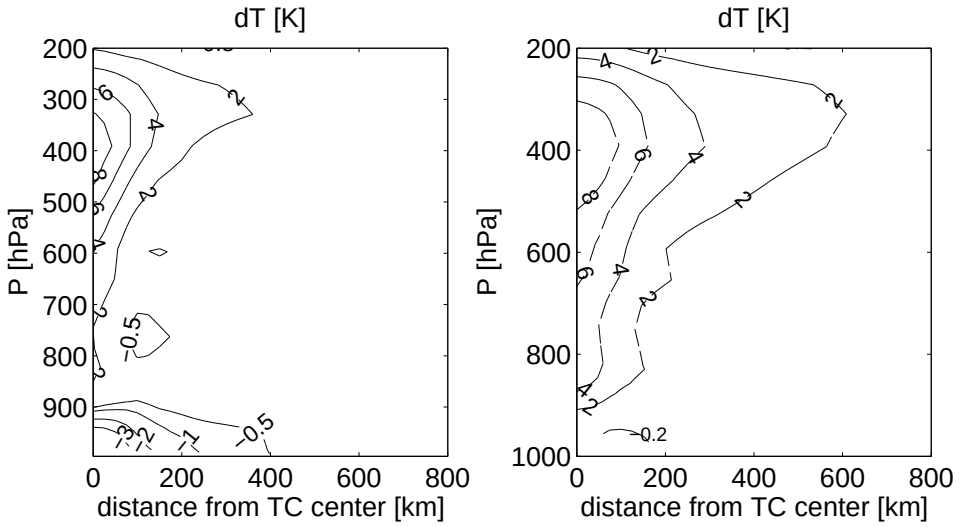

Figure 3.3: Time and azimuthal-mean height-radius cross-section of horizontal temperature anomaly (K) for simulations with H=0.1 m (left) and H=20 m (right).

The domain-mean SST increases from H=20 m to H = 0.5 m but decreases from H= 0.5 m to 0.1 m (Figure 3.4). This non-monotonic variation is mainly due to the effects of cloud. As shown in Figure 3.5a, the amount of low clouds increases as H decreases, while the amount of mid-level and high clouds decreases from H=20 m to H=1.25 m due to the reduced size of tropical cyclones (see Figure 3.13 in Section 3.6). Since the shortwave cloud radiative effect is sensitive to clouds at all levels, this variation of cloud amounts leads to a non-monotonic variation of the shortwave cloud radiative effect (Figure 3.5b). The longwave cloud radiative effect decreases slightly as the high clouds amount decreases from H=20 m to H=1.25 but the variation in total cloud radiative effect is still dominated by the shortwave part.

There is also an interesting lapse rate effect that could contribute to the variation of SST. In the tropics, the temperature in the upper troposphere is flattened due to the weak-temperature-gradient constraint (Sobel et al., 2001) and mostly controlled by SST in the deep-convection areas through the moist-adiabatic process. In our f-plane, we expect a weak-

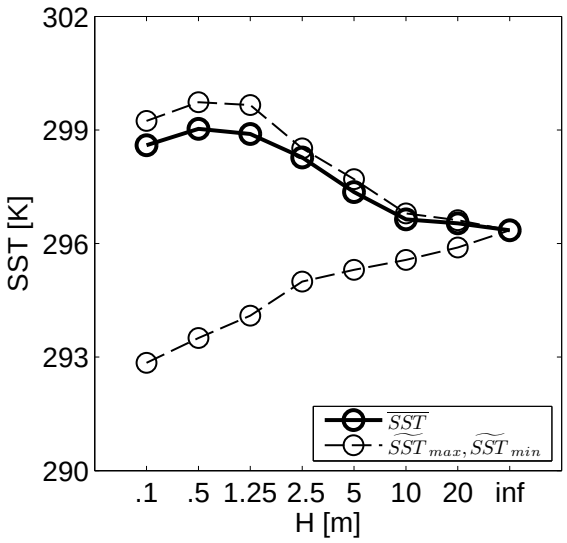

Figure 3.4: The domain-mean SST (black solid line), the maximum and minimum of the azimuthally-mean SST ($\widetilde{SST}_{max}$ and $\widetilde{SST}_{min}$, thin black dash lines) around tropical cyclones.

temperature-gradient constraint over the length scale of the Rossby radius of deformation. However, unlike in the tropics where deep convection is concentrated in the warm pool, deep convection is now located in the eyewall region of tropical cyclones which is cooler than the environment. This implies that the upper troposphere should also be cooler if compared to that in RRCE with the fixed domain-mean SST (Figure 3.6a). Since the cooling of the eyewall increases as H decreases, the relative cooling of the upper troposphere also increases. As a result, the lapse rate increases as H decreases and is anti-correlated with SST in the eyewall region (Figure 3.6b). The increased lapse rate will increase the domain-mean SST by reducing the outgoing longwave flux if everything else is fixed.

As H decreases, the domain -mean relative humidity (RH) increases in the upper troposphere but decreases at the surface (Figure 3.6c). The decreasing RH at the surface corresponds to an enhanced surface thermodynamic disequilibrium. As expected from the close balance between radiation cooling and latent heat flux, the domain-mean evaporation does not change substantially, but the mean surface wind speed decreases as the area of high winds decreases (Figure 3.1). Thus we interpret the increase in surface disequilibrium as a

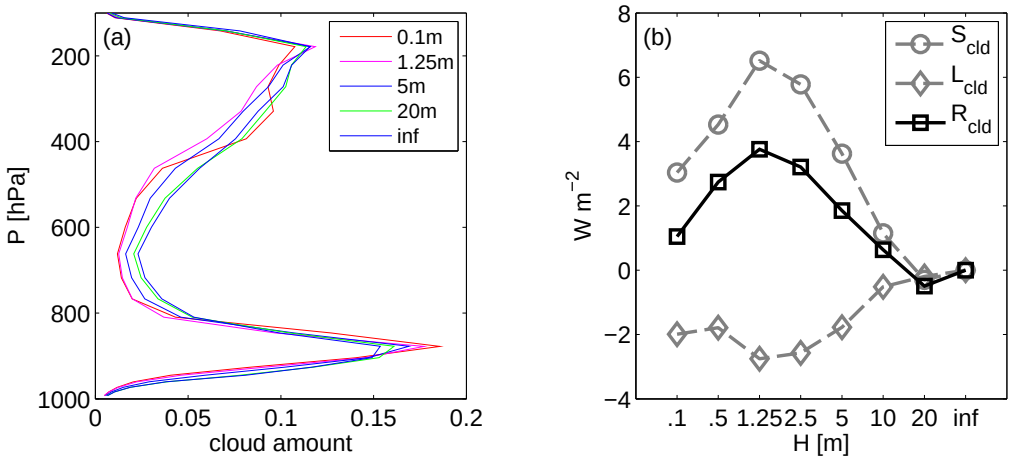

Figure 3.5: (a) The vertical profile of the domain-mean cloud amount; (b) The differences in the cloud radiative forcing at TOA for shortwave (gray line with circle symbol), longwave (gray line with diamond symbol) and total (black line) between simulations with coupled SST and the simulation with fixed SST.

mechanism to maintain the approximate strength of hydrological cycle in the presence of weaker mean surface wind.

The non-monotonic variation in the domain-mean SST could be seen as originating from the non-monotonic variation in cloud radiative effect and mediated by the lapse rate and water vapor effects. Particularly, the slight mismatch between the maximum domain-mean SST occurring at H=0.5 m and the maximum cloud-radiative forcing occurring at H=1.25 m highlights the effect from the increasing lapse rate.

3.4 Eyewall cooling of tropical cyclones

As shown in Figure 3.7, the magnitude of the relative eyewall cooling $\triangle SST$, measured as the difference between the maximum and minimum azimuthal-mean SST around tropical cyclones (Figure 3.8a), increases as H decreases but levels off as H approaches zero. The cooling in the eyewall region is found to be related to the negative net surface energy flux there (Figure 3.8b). By decomposing the surface flux into radiative and non-radiative components, we can see that two factors contribute to the negative value. First, the surface

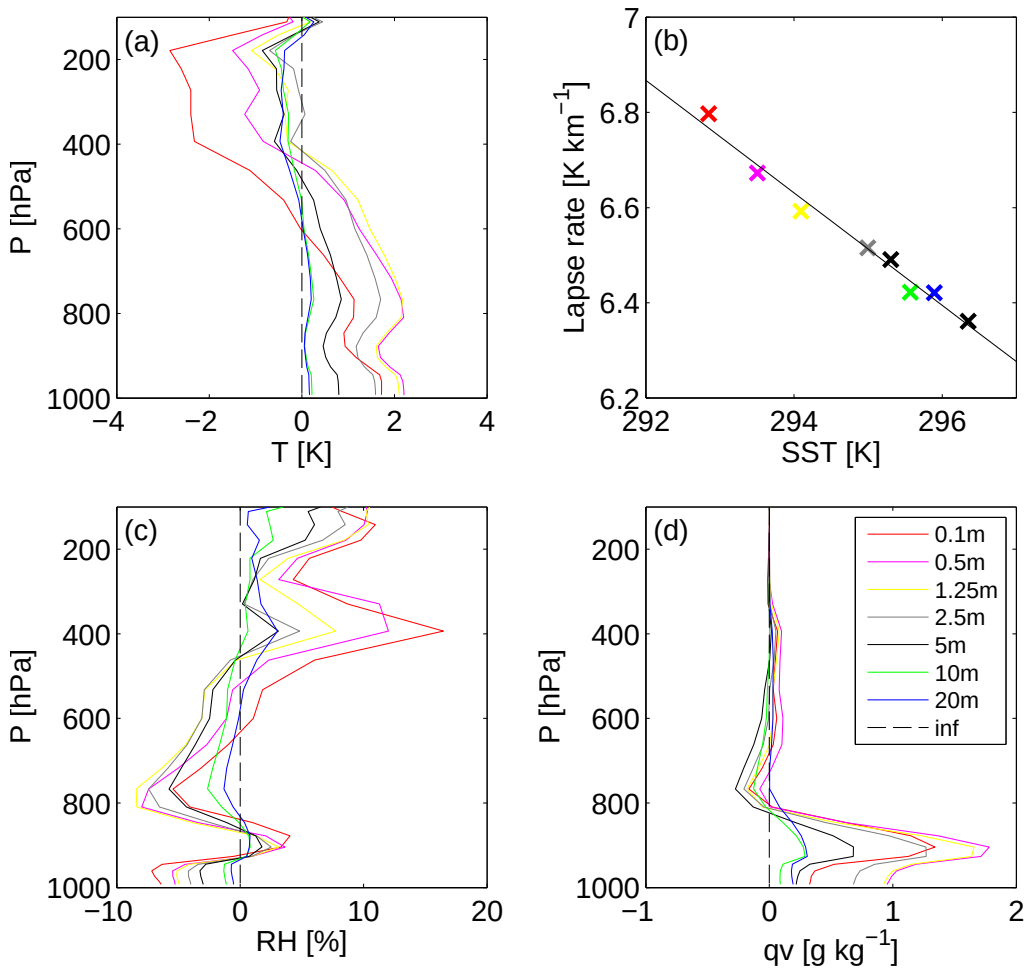

Figure 3.6: (a) The differences in vertical profiles of domain-mean temperature between simulations with coupled SST and the simulation with fixed SST. (b) The correlation between SST in the eyewall region and the mean lapse rate between 250 hPa and 950 hPa, computed as $-(T_{250} - T_{950})/(Z_{250} - Z_{950})$. (c) The same as (a) but for relative humidity. (d) The same as (a) but for specific humidity.

receives less shortwave radiative flux because of the excessive clouds in the eyewall region. The magnitude of this negative cloud radiative effect is almost insensitive to H (Figure 3.8c). Second, for a large H, the surface also transfers more heat flux into the atmosphere in the eyewall region due to the stronger surface wind there; For a small H, surface heat flux is, however, suppressed in the eyewall region as the surface disequilibrium decreases with the strong surface cooling (Figure 3.8d). The negative surface energy flux can then be seen as originating from the shortwave cloud radiative effect and strong winds in the eyewall region

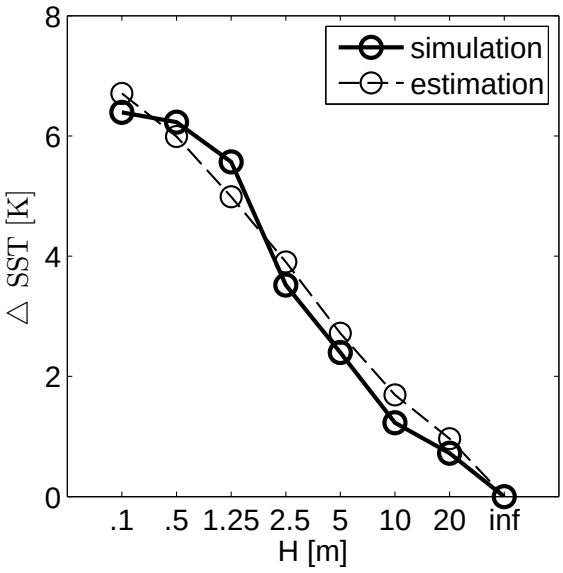

Figure 3.7: The relative cooling of the eyewall, $\triangle SST = \widetilde{SST}_{max} - \widetilde{SST}_{min}$, simulated by the model (black solid line) and estimated by Eqn. 3.9 (thin black dash line).

but is also mediated by a negative SST-surface-disequilibrium feedback. Particularly, the maximum magnitude of the negative surface flux decreases from 200 W m^{-2} at H=20 m to 25 W m^{-2} at H= 0.5 m, and eventually becomes zero as H approaches zero.

To better understand what controls the magnitude of the eyewall cooling, we develop a minimalist model as described below. First, we would like to address the case as H approaches zero. At the limit of zero H, no energy is allowed to be stored in the ocean so the surface energy balance equation for the environment can be written as

$$R = V_E C_k C_{pa} \rho_a \delta k_o \tag{3.2}$$

where R, V_E and δk_o are the surface radiative flux, the wind speed and the surface disequilibrium (in temperature unit) in the environment, C_k is the surface exchange coefficient for enthalpy, ρ_a and C_{pa} are the density and heat capacity of air.

For the eyewall, we have

$$R - R' = V_C C_k C_{pa} \rho_a (\delta k_o - \beta \triangle SST) \tag{3.3}$$

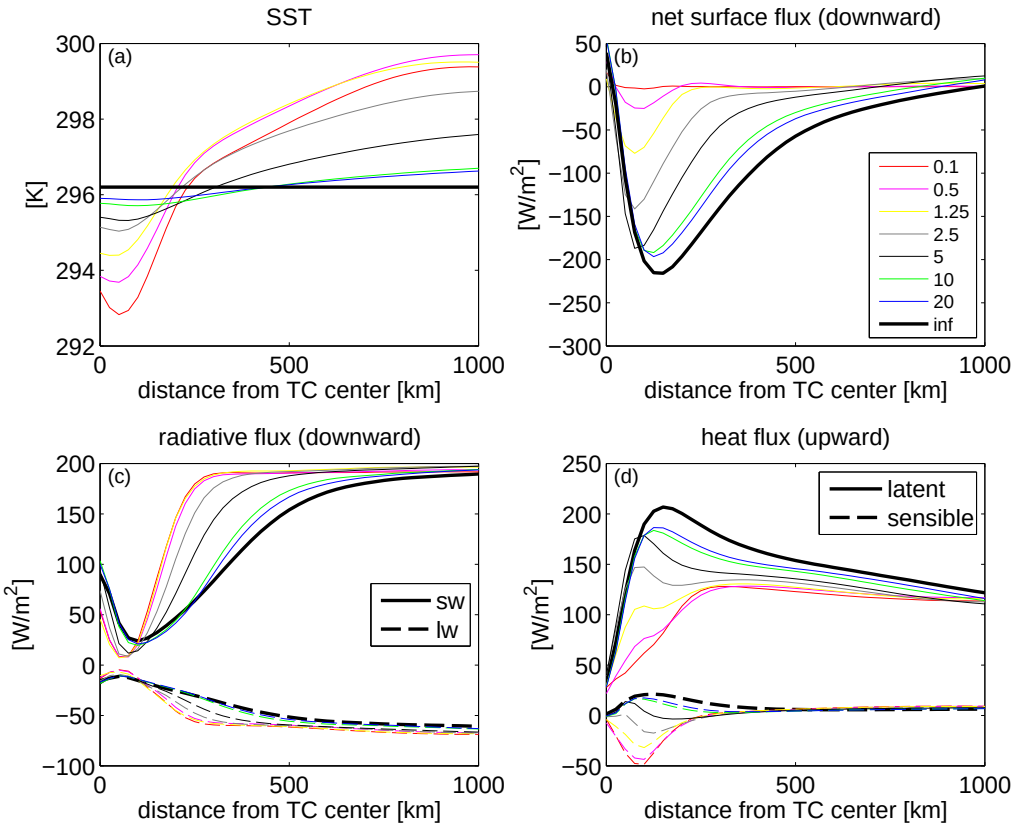

Figure 3.8: The time- and azimuthal-mean surface fluxes and SST as a function of the distance from TC center for different depths of slab ocean layer. (a) SST; (b) The net surface energy flux; (c) The net shortwave (solid) and net longwave flux (dash) at the surface; (d) The latent (solid) and sensible (dash) heat flux at the surface.

where R' and V_C are the radiative effect of cloud and the wind speed at the eyewall, and β represents the strength of SST-surface-disequilibrium feedback.

Combining the above two equations, we have an estimation for $\triangle SST$ at the limit of zero H as

$$\triangle SST = \frac{\delta k_o}{\beta}[1 - (1 - \frac{R'}{R})\frac{V_E}{V_C}] \tag{3.4}$$

We can see the radiative effect of cloud is represented by the term $1 - R'/R$ while the effect of strong winds is represented by the term V_E/V_C. $\triangle SST$ increases as either effect increases its strength.

Next, we would like to address the effect of the finite-depth slab ocean layer on the eyewall cooling. In the reference frame following tropical cyclones, there is a 'flow' in the stagnant

slab ocean layer in the opposite direction to the translation of the tropical cyclone. This flow transport energy from the environment, which is heated by the positive net surface flux, into the area underlying the cold core of tropical cyclones, which is cooled by the negative net surface flux. The energy transport can be approximated as

$$\rho_w H C_{pw} \frac{\triangle SST}{\tau_o} \tag{3.5}$$

where τ_o is the characteristic time scale of communication between the warmer environment and the cold core of tropical cyclones, which can be roughly estimated as $\tau_a = \frac{V_S}{L_C}$ where V_S and L_C are the translation speed of tropical cyclone and the length scale of the cold core. One can then rewrite Eqn. 3.3 by including this effect into the surface energy balance at the eyewall

$$R - R' + \rho_w H C_{pw} V_S \frac{\triangle SST}{L_C} = V_C C_k C_{pa} \rho_a (\delta k_o - \beta C_{pa} \triangle SST) \tag{3.6}$$

Combining Eqn. 3.2 and Eqn. 3.6, we derive a relationship between $\triangle SST$ and H as

$$\triangle SST = \frac{\delta k_o}{\beta + \alpha \frac{H}{L_C}} [1 - (1 - \frac{R'}{R}) \frac{V_E}{V_C}] \tag{3.7}$$

where

$$\alpha = \frac{1}{C_k} \frac{\rho_w}{\rho_a} \frac{C_{pw}}{C_{pa}} \frac{V_S}{V_C}. \tag{3.8}$$

The magnitude of the eyewall cooling $\triangle SST$ is then related to the depth of the slab ocean H as the following form

$$\triangle SST \propto \frac{\triangle T_o}{1 + H/H_o} \tag{3.9}$$

As shown in Figure 3.7, this formula estimates the variation with H fairly well with a best-fit estimations of $\triangle T_o \simeq 7$ K and $H_o \simeq 2$ m according to the values of parameters listed in Table 3.1

Parameters	Values	Parameters	Values
δk_o	18 K	V_E/V_C	0.1
β	2.5	V_S/V_C	0.15
α	5×10^5	C_k	0.0012
R'/R	0.9	L_C	400 km

Table 3.1: Approximate values of parameters in the minimalist model for the eyewall cooling.

3.5 Intensity of tropical cyclones

Despite the substantial eyewall cooling, TC intensity barely decreases as H decreases (Figure 3.9). As argued in Khairoutdinov and Emanuel (2013), TC intensity in RRCE scales with the cube root of the net radiative cooling of the troposphere. Given that the net radiative cooling is invariant in our coupled-SST experiments, one expects TC intensity to stay approximately constant. The widely-accepted Potential Intensity (PI) theory (Emanuel, 1991), however, disagrees with this, as it would predict a very weak intensity of tropical cyclones given that the surface disequilibrium is nearly zero at the eyewall due to the substantial cooling there (Figure 3.10). To confirm this, we compute the potential intensity of tropical cyclones according to the CAPE algorithm in Bister and Emanuel (2002a). The original PI algorithm[1] (PI-O) does not consider the effect of the eyewall cooling by assuming the surface conditions are the same between the eyewall region and the environment. We therefore introduce a modified PI algorithm (PI-E), described in Appendix, which includes the effect of the eyewall cooling as simulated in the model. One can then see PI-O as the intensity tropical cyclones could achieve without eyewall cooling and PI-E as the intensity that could achieve with eyewall cooling. The results from both the original and modified PI algorithms are shown in Figure 3.9. As H decreases, PI-O increases due to the increasing surface disequilibrium in the environment while PI-E decreases due to the decreasing surface disequilibrium at the eyewall (Figure 3.10). The effect of the eyewall cooling on TC intensity can be seen by comparing PI-E or simulated intensity with PI-O. Both PI theory and model simulations indicate an increased reduction of TC intensity as the eyewall cooling increases. However, the reduction

[1]obtained from ftp://texmex.mit.edu/pub/emanuel/TCMAX/

in model simulations is smaller than that estimated by PI theory, as PI-E predicts a much weaker intensity for tropical cyclones in cases with substantial eyewall cooling.

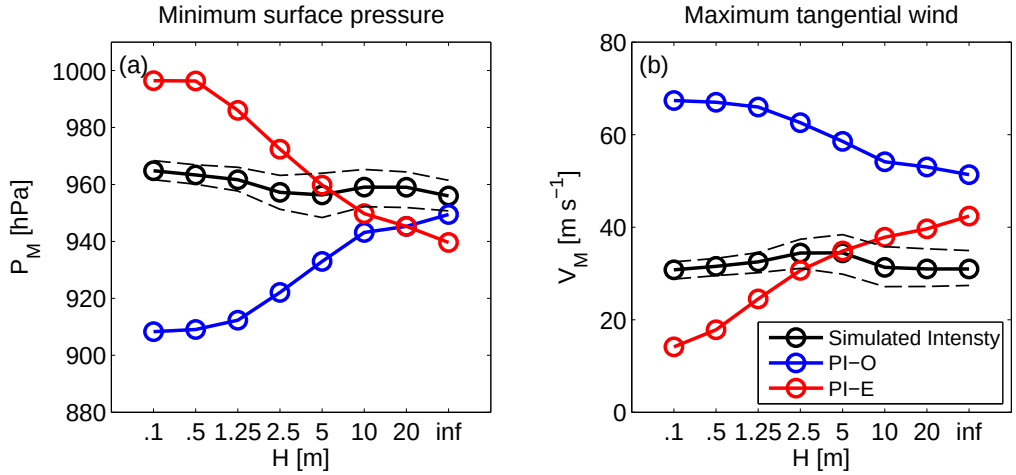

Figure 3.9: Intensity and PIs as a function of H. The gray solid lines show the median intensity of tropical cyclones and the gray dash lines indicate the first and third quartiles; The red lines show PI computed from the original algorithm (PI-O); The blue lines show PI computed from the modified PI algorithm considering the eyewall cooling (PI-E).

To understand why PI theory underestimates the simulated intensity of tropical cyclones in cases with substantial eyewall cooling, we examine certain assumptions made in PI theory. A key assumption is that moist entropy s is well-mixed along surfaces of angular momentum M in both the free troposphere and the atmospheric boundary layer. This assumption ultimately allows one to write moist entropy S as a function of angular momentum M.

Integrating along the slantwise neutral vortex in the free troposphere, Emanuel (1986) formulates the derivative of moist entropy to angular momentum at the top of the boundary layer as

$$\frac{dS}{dM}|_b = -\frac{V_b}{(T_b - T_o)r} \tag{3.10}$$

where V_b and T_b are the azimuthal wind speed and temperature at the top of the boundary layer; T_o is the outflow temperature along an angular momentum surface where it passes through the point of V = 0.

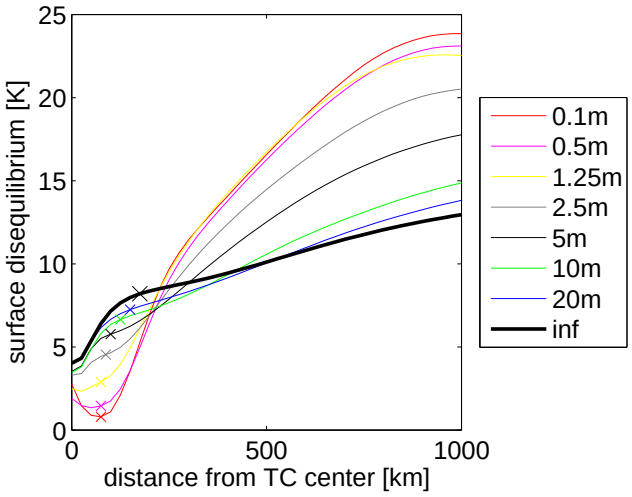

Figure 3.10: The time- and azimuthal-mean surface disequilibrium of enthalpy as a function of the distance from TC center in simulations with different depths of slab ocean layer. The surface disequilibrium is computed as $\delta k = \delta t + L_v \delta q / C p_a$ where δt and δq are the differences in temperature and specific humidity between the saturated surface and the surface air (at the first model level). The cross symbols indicate the locations of the eyewall.

Integrated through the depth of the boundary layer, the total derivative of moist entropy and angular momentum can be written respectively as

$$D\frac{d\overline{S}}{dt} = C_k|\mathbf{V}|\frac{k^* - k}{T_s}$$

$$D\frac{d\overline{M}}{dt} = -C_d r|\mathbf{V}|V$$

where $\overline{s}$ and $\overline{M}$ are the entropy and angular momentum averaged through the depth D of the boundary layer, C_k and C_d are exchange coefficients for energy and momentum, $|\mathbf{V}|$ is the wind speed at the flux reference level, and V is the azimuthal velocity, $k^* - k$ is the surface disequilibrium of enthalpy. The turbulent flux of entropy and the entropy source from dissipative heating have been neglected.

The mean derivative of moist entropy to angular momentum through the depth of the boundary layer can then be written as

$$\overline{\frac{dS}{dM}} = -\frac{C_k}{C_d}\frac{k* - k}{rT_sV} \tag{3.11}$$

With the assumption that moist entropy is well-mixed along angular momentum surfaces in the boundary layer, one has

$$\overline{\frac{dS}{dM}} = \frac{dS}{dM}|_b \tag{3.12}$$

The combination of Eqn. 3.10, 3.11, 3.12 leads to the well-known theoretical formula of PI theory as

$$V_{PI} \simeq \sqrt{\frac{C_k}{C_d}\frac{T_b - T_o}{T_s}(k^* - k)} \tag{3.13}$$

Dropping the assumption that moist entropy is well-mixed along angular momentum surfaces within the boundary layer, one should instead have

$$V = \alpha V_{PI} \tag{3.14}$$

where

$$\alpha = \sqrt{\frac{dS}{dM}|_b / \overline{\frac{dS}{dM}}} \tag{3.15}$$

is the parameter measuring how well moist entropy is mixed along angular momentum surfaces in the boundary layer.

As shown in Figure 3.11, the assumption that moist entropy is well-mixed along angular momentum surfaces in the eyewall region is roughly satisfied in the case with H=20 m. But for the case with substantial eyewall cooling at H=0.1 m, such an assumption is violated within the boundary layer. That means Eqn. 3.12 is no longer justified for H=0.1 m. Particularly, the parameter α should be larger than 1 in Eqn. 3.14, given $\frac{dS}{dr}$ at the eyewall decreases from nearly zero at the surface to the negative value at the top of the boundary layer. This helps explain why PI theory underestimates TC intensity in the cases with substantial eyewall cooling.

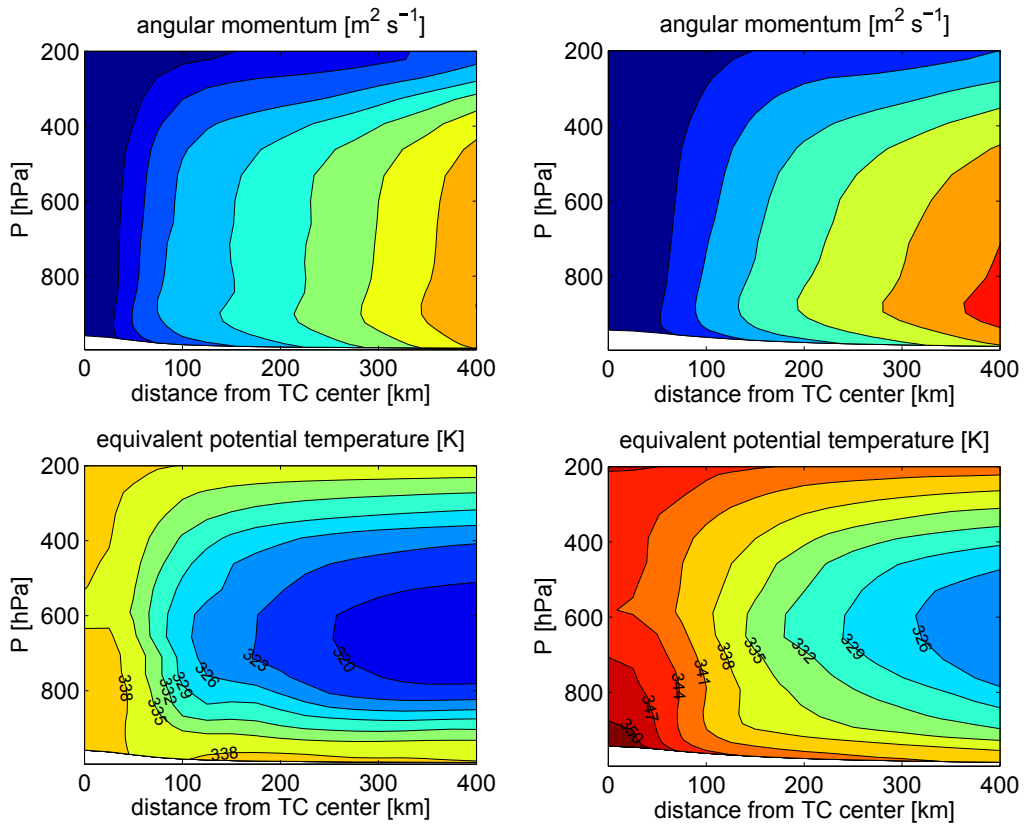

Figure 3.11: Time and azimuthal-mean height-radius cross-section of angular momentum (m^2 s^{-1}, top) and equivalent potential temperature (K, bottom) for simulations with H=0.1 m (left) and H=20 m (right).

3.6 Structure of tropical cyclones

While a 25-km resolution is not adequate to resolve more detailed aspects of the tropical cyclone structure, a well-defined eyewall with deep ascent is apparent, as well as the characteristic inflow in the boundary layer and outflow in the upper troposphere (Figure 3.12). The size of tropical cyclones is computed as $L \sim \sqrt{A/n}$ where A is the area of the doubly-periodic domain and n is the average number of tropical cyclones within the domain. This is the scale over which a cyclone suppress other storms. It is larger than a scale determined by a particular azimuthal wind speed such as in Chavas and Emanuel (2014). The radius of maximum wind, R_{MW}, is defined as the radius of the maximum azimuthal surface wind.

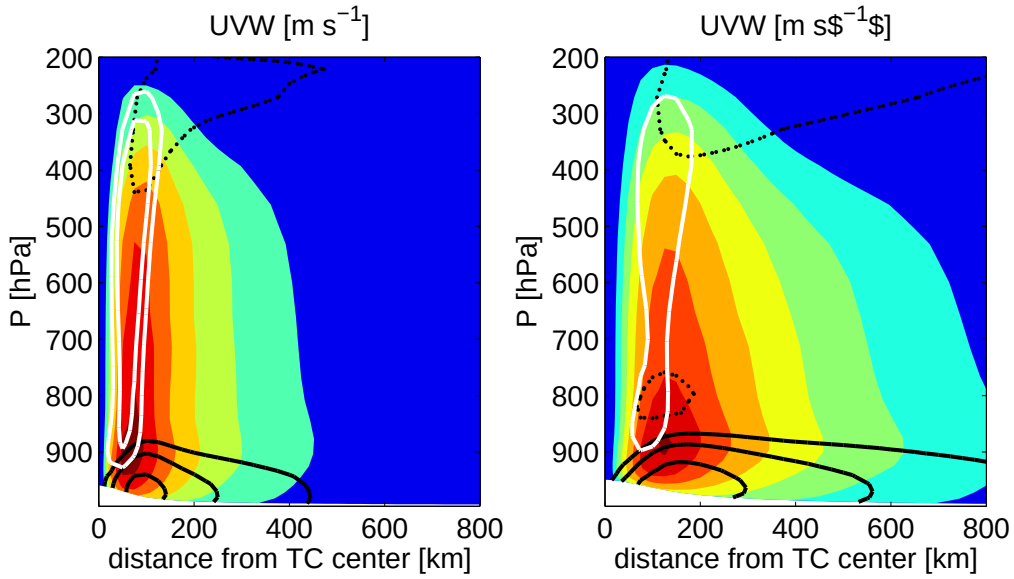

Figure 3.12: Time and azimuthal-mean height-radius cross-section of tangential wind (color shade), radial wind (black contour) and vertical velocity (white contour) for simulations with H=0.1 m (left) and H=20 m (right). Radial winds are contoured at 2, 5, 10, 15 m s^{-1}. Positive (outflow) values are dotted, negative (inflow) values are solid. Vertical velocity is contoured at 0.2, 0.3 m s^{-1} (K).

As shown in Figure 3.13a, R_{MW} decreases continuously from H=20 m to H=1.25 m and stays nearly unchanged as H further decreases. The variance of R_{MW}, estimated as the difference between the first and third quartiles among all tropical cyclones, increases with H but curiously is very small with fixed SST. As we see in Figure 3.4, there is still an considerable SST variation (0.5^oC) with a slab ocean of 20 m which might lead to the variation of R_{MW}. Such a transition between simulations with coupled SST over a large H and fixed SST implies the importance of the ocean coupling in realistic tropical cyclone simulations. The constant R_{MW} with very small H could be an artifact of the model resolution (25 km). If so, the decreasing cloud radiative effect as H decreases from H=1.25 m (Figure 3.5) could also be artificial such that the domain-mean SST would increase monotonically as H decreases.

Along with R_{MW}, L also decreases from H=20 m to H=1.25 and stays nearly unchanged as H further decreases. Two theoretical scalings for the size of tropical cyclones are compared to the simulation results. One is the Rossby radius of deformation NH/f, where N is the static stability parameter and H is the scale height of the atmosphere. The other is the storm-

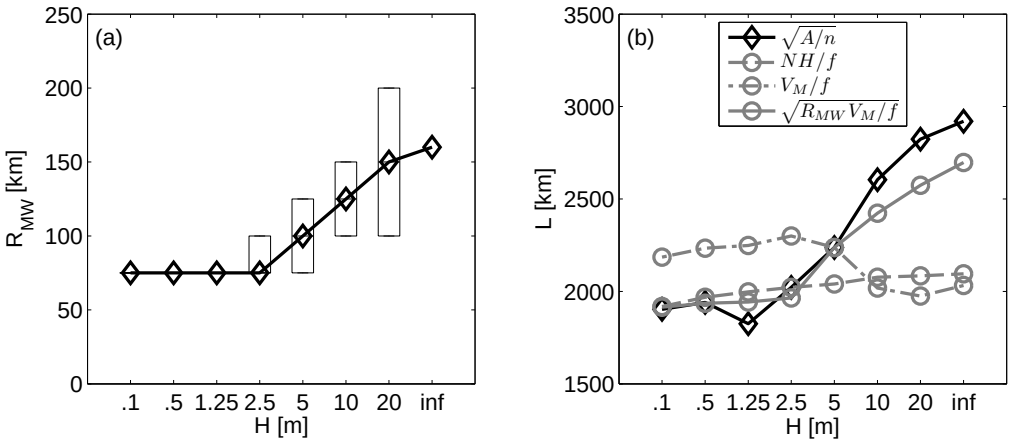

Figure 3.13: (a) The variation of the radius of the maximum wind (R_{MW}) as a function of H. The black solid lines with diamond maker show the median value. The gray box indicates the first and third quartiles. (b) The size of tropical cyclones calculated as $L = \sqrt{A/n}$ (black solid line). Rossby radius of deformation $\sqrt{NH/f}$ is shown as the gray dash line. The stratification stability is calculated as $N^2 = g/\theta_o \delta\theta/\delta_z$, where θ_o is the potential temperature at 500 hPa, $\delta\theta$ is the difference in potential temperature between 200 hPa and 900 hPa. The scaling height of atmosphere is set as a constant of 8 km. The scaling of $\sqrt{V_M/f}$ is shown as the gray dash-dot line and $\sqrt{R_{MW}V_M/f}$ is shown as the gray solid line.

related length scale $L \sim V_M/f$, where V_M is the maximum wind. As shown in Figure 3.13b, both scalings fail to capture the variation of L with H. By assuming a constant reduction factor of angular momentum from the environment to R_{MW}, Zhou et al. (2014) show that the scaling $L \sim \sqrt{R_{MW}V_M/f}$ works rather well in RRCE with fixed-SST. It is found that, in RRCE with coupled SST, this scaling also gives a better fit than the other two. Although this relationship between L and R_{MW} does not in itself provides a theory for L or R_{MW}, it implies that L and R_{MW} are highly correlated.

3.7 Conclusions

In this study, rotating radiative-convective equilibrium (RRCE) with coupled SST is achieved by coupling the column physics of HiRAM at GFDL to rotating hydrostatic dynamics in a large doubly-periodic domain. Unlike previous studies that prescribe a homogeneous fixed SST over the domain, we have used coupled SST to a simple slab ocean layer. The sensitivity

of tropical cyclones to the depth of this slab ocean layer H is then investigated by varying H in a wide range.

With coupled SST, the eyewall region of tropical cyclones becomes cooler relative to the environment. This cooling originates from the negative shortwave cloud radiative effect and strong winds at the eyewall but is also strongly modulated by a negative SST-surface-disequilibrium feedback. The magnitude of the eyewall cooling increases as H decreases but levels off eventually as H approaches zero. A minimalist model suggests the form of, $\triangle SST \simeq \frac{\triangle T_o}{1+H/H_o}$, for the dependence of this cooling on the ocean depth H.

The intensity of tropical cyclones is reduced from the potential intensity they might achieve without the eyewall cooling, but they are still able to sustain themselves, even in cases with substantial eyewall cooling. The intensity reduction in model simulations is found to be smaller than that estimated by Potential-Intensity theory, which underestimates the intensity of tropical cyclones in cases with substantial eyewall cooling. The weaker intensity predicted by PI theory is directly correlated with the small surface thermodynamic disequilibrium at the eyewall by assuming that moist entropy is well-mixed along angular momentum surfaces in the boundary layer. However, we find that this assumption is no longer valid in our simulations with substantially eyewall cooling. PI theory then underestimates the simulated intensity as the parameter $\alpha = \sqrt{\frac{dS}{dM}|_b / \overline{\frac{dS}{dM}}}$ becomes larger than one. A qualitative understanding of this parameter α is desired to include the effect of the eyewall colling into Potential-Intensity index in future studies.

3.8 Appendix: A modified PI algorithm considering the eyewall cooling

The widely-used PI algorithm is written as below (Bister and Emanuel, 2002b; Garner, 2014):

$$R\overline{T_{ve}}\ln\left(\frac{P_e}{P_c}\right) = CAPE_c - CAPE_e + \beta(CAPE_c^* - CAPE_c) \tag{3.16}$$

$$V_P^2 = 2\beta(CAPE_c^* - CAPE_c) \tag{3.17}$$

Here R is the ideal gas constant, P_e is the environmental surface pressure and P_c is the potential minimum pressure at the outer eyewall, $\overline{T_{ve}}$ is the mean environmental virtual temperature between the surface and $P = P_c$, $\beta = \frac{C_k}{2C_d}\frac{T_b}{T_o}$ where C_k and C_d are exchange coefficients for energy and momentum, T_b and T_o are the inflow and outflow temperature. $CAPE_e$ is the environmental convective available potential energy. $CAPE_c$ and $CAPE_c^*$ refer to hurricane $CAPE$, which is defined by the potential energy of a parcel lifted from the outer eyewall surface pressure. Respectively, $CAPE_c$ is associated with the surface air parcel, $CAPE_c^*$ is associated with the saturated parcel at SST. The original algorithm assumes that surface conditions are the same between the outer eyewall and the environment such that $CAPE_c$, $CAPE_c^*$ are computed from the environmental profile as following:

$$CAPE_c(P^e, T^e, RH^e; P_c, T_s^e, RH_s^e) \tag{3.18}$$

$$CAPE_c^*(P^e, T^e, RH^e; P_c, SST^e) \tag{3.19}$$

where P^e, T^e, RH^e are the environmental vertical profiles of pressure, temperature and relative humidity, SST^e, T_s^e and RH_s^e are the environmental SST, surface air temperature and surface relative humidity.

The above assumption is no longer valid in simulations with significant eyewall cooling. To account for the effect of the eyewall cooling, we modify the original algorithm by using the simulated SST at the radius of maximum wind (SST^c) for $CAPE^*_c$, and simulated surface air temperature and relative humidity at the radius of maximum wind (T^c_s, RH^c_s) for $CAPE_c$.

$$CAPE_c(P^e, T^e, RH^e; P_c, T^c_s, RH^c_s) \tag{3.20}$$

$$CAPE^*_c(P^e, T^e, RH^e; P_c, SST^c) \tag{3.21}$$

Chapter 4

The impact of vertical shear on the sensitivity of tropical cyclogenesis to environmental rotation and thermodynamic state

4.1 Introduction

Tropical cyclogenesis is one of the most intriguing yet poorly understood problems in tropical meteorology. Given the extreme catastrophe tropical cyclones could bring to human society, it is important for us to understand and predict their genesis. Particularly, one would like to know the sensitivity of tropical cyclogenesis to environmental parameters, e.g., vertical wind shear, ambient rotation, thermodynamic state, which might vary in the scenario of future climate change. Idealized cloud-resolving simulations have been increasingly used to study such problems.

The suppression effect of vertical shear on tropical cyclogenesis has been well appreciated (Gray, 1968; McBride and Zehr, 1981; Bracken and Bosart, 2000). A robust paradigm

of tropical cyclogenesis from a preexisting disturbance in vertical shear has been revealed through idealized simulation of the intensification of an incipient vortex (e.g. Rappin and Nolan, 2012; Zhang and Tao, 2013). The vertical shear first develop a vertical tilt of vortex with the mid-level vortices advected into the downshear direction of the surface center. The tilted vortex then undergoes a precession process, with the mid-level vortices rotating cyclonically around the surface center, as a result of the vertically penetrating flow associated with the lower portion of the tilted vortex. Rapid intensification occurs once the mid-level vortices have precessed into the up-shear flank, with both the tilt magnitude and the effective (local) vertical wind shear considerably decreased. The time to genesis is intimately tied to the duration of this precession process, which is found to be sensitive to the magnitude and orientation of vertical shear (Rappin and Nolan, 2012), the intrusion of dry air (Ge et al., 2013) as well as the upscale grow of random noise from moist convection (Zhang and Tao, 2013).

The dependency of tropical cyclogenesis on environmental rotation has been studied in a quiescent environment (Rappin et al., 2011; Smith et al., 2014; Miyamoto and Takemi, 2015). An initial weak vortex is found to intensify faster with a lower Coriolis parameter (Figure 4.1). Although the conclusion seems to be robust across these four studies, there are two things worth noting. First, all these studies assumed a quiescent environment such that the effect of vertical shear is not considered. Given the crucial role of vertical shear in regulating the intensification process, it is worthwhile to investigate its impact on the sensitivity of tropical cyclogenesis to ambient rotation. Second, they all use some tropical observational sounding to initialize the environment. Radiative process is neglected given that the environment is not in simple radiative-convective balance with the surface. The other way to initialize the environment in literature is the so-called radiative-convective equilibrium (RCE) framework (Nolan et al., 2007; Nolan and Rappin, 2008; Rappin et al., 2010). One first achieves RCE in a small domain. The mean sounding of this RCE is then used to initialize the environment in the large-domain genesis simulations. This RCE

framework assures that the environment will not drift during the genesis simulation. It is not clear whether these two approaches will always lead to consensus, and more generally, whether the dependency of tropical cyclogenesis on ambient rotation will be sensitive to the environmental thermodynamic state.

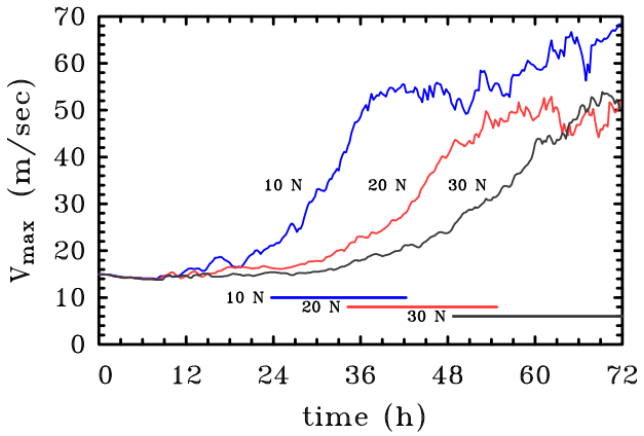

Figure 4.1: Time series of maximum azimuthal-mean wind in simulations of tropical cyclogenesis in a quiescent environment with the Coriolis parameter at 10^oN, 20^oN, and 30^oN (Smith et al., 2014).

The sensitivity of tropical cyclogenesis to the environmental thermodynamic state has been investigated in Nolan et al. (2007) and Rappin et al. (2010). They found that the time to genesis in environments without vertical shear is correlated with the potential intensity of tropical cyclones, V_p, which indicates the theoretical maximum intensity tropical cyclone could achieve given the environmental vertical sounding (Emanuel, 1986; Bister and Emanuel, 2002b); while the time to genesis in environments with vertical shear is correlated to the incubation parameter, χ_b, which measures the relative importance of subsidence across the boundary-layer top as compared to the effect of surface fluxes on the boundary-layer entropy. The different parameters here again highlight the importance of the vertical shear. These two studies use the RCE framework mentioned above. It is thus worthwhile to investigate the cases initialized from some observational soundings. One would also like to know whether a thermodynamic state that is favorable for tropical cyclogenesis in environment without vertical shear will also be favorable with vertical shear.

In this study, we first study the following questions through idealized cloud-resolving simulations:

Q1: Will the dependency of tropical cyclogenesis on ambient rotation be sensitive to vertical shear?

Q2: Will the dependency of tropical cyclogenesis on ambient rotation be sensitive to environmental thermodynamic state?

Q3: Will the thermodynamically favorability of an environment for tropical cyclogenesis be sensitive to the presence of vertical shear?

We also conduct analogous simulations with the resolution and column physics of HiRAM at GFDL, which is able to realistically simulate the observed global climatology and internal variability of hurricane frequency (Zhao et al., 2009). Such comparison provides an idealized framework to evaluate the ability of GCMs to simulate tropical cyclogenesis.

The Chapter is organized as follows: The model configuration and experiment setup are described in the Section 4.2. In Section 4.3, we look at Q1 by investigating tropical cyclogenesis in RCE environments with various vertical shear. In Section 4.4, Q2 and Q3 are then studied by varying environmental thermodynamic states. The results with HiRAM is presented in Section 4.5. Discussion and conclusion are offered in Section 4.6.

4.2 Model and Experiments

4.2.1 WRF

Idealized cloud-resolving simulations are conducted with the Weather Research and Forecasting Model (WRF v3.6, Skamarock et al., 2008). WRF is a fully compressible atmospheric model designed for mesoscale and convective-scale simulations of real and idealized weather. The model we used has 43 terrain-following vertical levels with 9 of them below 850 hPa and the model top at about 50 hPa. The horizontal grid resolution is 5 km and no convective parameterization is used. The genesis simulation is performed in a doubly-periodic

domain with a size of 2400 km × 2400 km. The Yonsei University (YSU) boundary layer scheme (Hong et al., 2006) is applied for vertical turbulent mixing and the two-dimensional Smagorinsky subgrid scheme is applied for horizontal mixing. The surface fluxes are computed based on Monin-Obukhov theory. The WRF single-moment six-class scheme (Hong and Lim, 2006) is used for microphysics processes. If used, radiation physics is handled by the Rapid Radiative Transfer Model (RRTM-G, Mlawer et al., 1997; Iacono et al., 2008), with a fixed zenith angle $u_o = 50.5^o$ and solar constant $S_o = 650.83\ Wm^{-2}$.

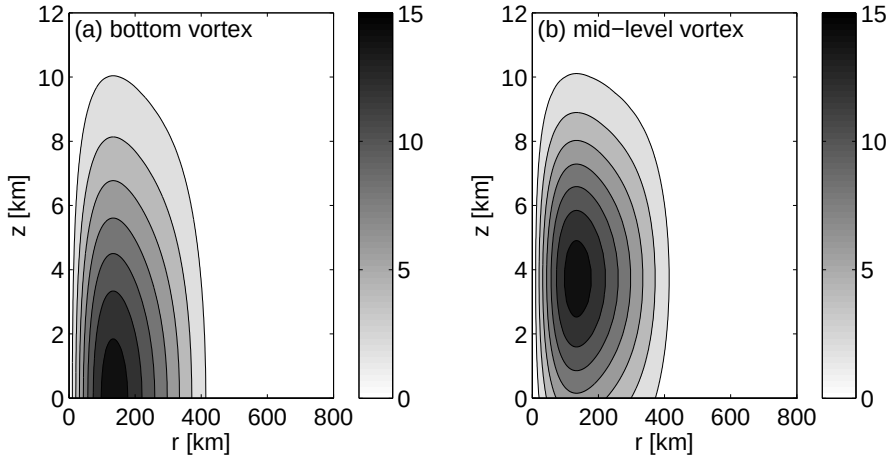

Figure 4.2: Radius-height cross-section of the azimuthal wind field (m s^{-1}) for the initial (a) bottom vortex with z_0=0 m, L_z=5000 m and (b) mid-level vortex with z_0=3720 m, L_z=3175.23 m. We use b=120 km and R = 4000 km for both vortexes.

We first investigate the impact of vertical shear using the RCE framework. RCE is achieved in a small domain (160 km × 160 km). Its mean sounding is then used to initialize the environmental thermodynamic state in genesis simulations. The genesis simulations are initialized from either a bottom or a mid-level vortex (Figure 4.2). The azimuthal wind profile of the initial vortex is calculated from the radial integration of a Gaussian vorticity distribution following Nolan et al. (2007),

$$v_0(r) = \frac{1}{r}\int_0^r r\zeta dr$$

where the relative vorticity ζ is defined as $\zeta(r) = Ae^{-\left(\frac{r}{b}\right)^2}$. The wind velocity goes smoothly to zero beyond some radius R and decay vertically following

$$V(r,z) = v_0(r)e^{-\left(\frac{r}{R}\right)^6} e^{-\frac{|z-z_0|^\alpha}{\alpha L_z^\alpha}}$$

The parameters for vortex configuration are listed in the caption of Figure 4.2. The radius of maximum surface wind is at about 125 km. The temperature and humidity fields are adjusted towards thermal wind balance assuming unchanged relative humidity.

Six different vertical shear profiles are considered, varying from a 7 m s^{-1} easterly shear to a 5 m s^{-1} westerly shear between 850 hPa and 200 hPa (Figure 4.3). The surface wind is 3 m s^{-1} westerly. We name the wind shear profile by two parameters, the mean surface wind and the large-scale vertical shear, such that, SF3–SH3 corresponds to a westerly mean surface flow of 3 m s^{-1} and westerly vertical shear of 3 m s^{-1}. The method introduced in Rappin et al. (2010) is used to incorporate vertical shear in a doubly-periodic domain without large-scale temperature gradient.

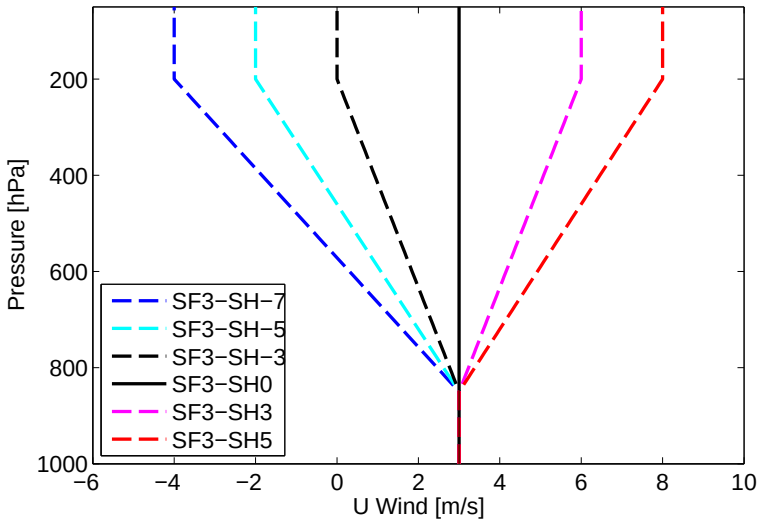

Figure 4.3: Six environmental wind profiles used in this study.

In order to investigate the sensitivity to the environmental thermodynamic state, three additional tropical soundings (Figure 4.4) are considered for simulations initialized from a

bottom vortex in both a quiescent environment and that with a 3 m s^{-1} westerly vertical shear (SF3-SH3): **RE**: the neutral sounding from Rotunno and Emanuel (1987) with SST at 27 ^{o}C; **Jordan**: the hurricane season sounding from Jordan (1958) with SST at 27.5 ^{o}C; **MT**: the moist tropical sounding from Dunion (2011) with SST at 28 ^{o}C.

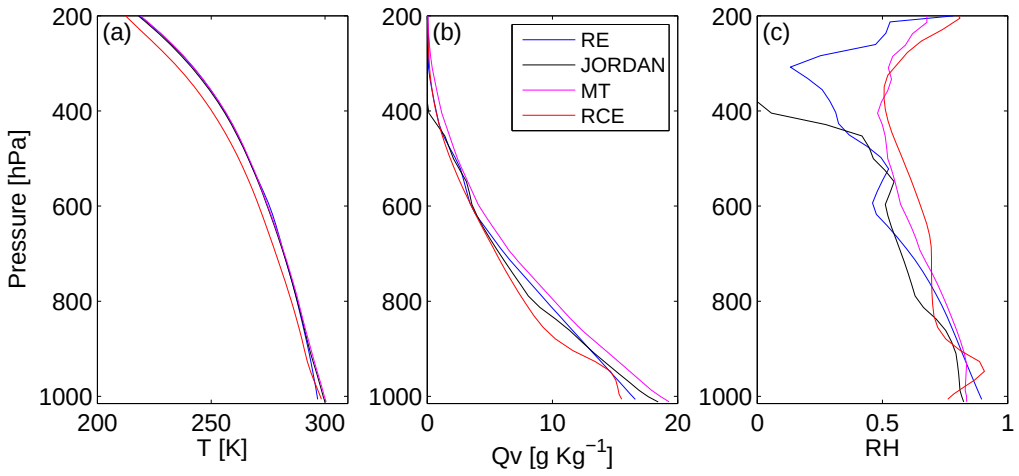

Figure 4.4: Vertical profiles of (a) temperature, (b) specific humidity and (c) relative humidity in differet soundings.

4.2.2 HiRAM

Analogous genesis simulations with the resolution and column physics of HiRAM, as described in Section 2.2, are conducted in a doubly-periodic domain of 2400 km x 2400 km. The same bottom and mid-level vortex have been used to initializ the genesis simulations in an environment with the Jordan sounding.

4.3 Varying vertical shear in a RCE framework

The time evolutions of the minimum surface pressure are shown in Figure 4.5 for WRF simulations initialized from a bottom vortex and in Figure 4.6 for simulations initialized from a mid-level vortex. A few features revealed by other studies are consistently presented in our simulations: First, compared to the case with a uniform environmental flow (Figure

4.5d and 4.6d), the maximum intensity reached by the tropical cyclone is reduced by the vertical shear, irrespective of its direction. Second, tropical cyclogenesis is more efficient with a bottom vortex, in terms of both intensification rate (Ge et al., 2011) and the sustainability to wind shear. For example, the bottom vortex succeeds to intensify in a 5 m s^{-1} westerly vertical shear with f at 15^oN (Figure 4.5f), while the mid-level vortex fails (Figure 4.6f). Third, the suppression effect of wind shear on tropical cyclogenesis depends not only on the magnitude of vertical shear but also the orientation of vertical shear relative to the surface wind. As elucidated in Rappin and Nolan (2012), a counter-aligned vertical shear relative to the surface wind is less detrimental to tropical cyclogenesis compared to an aligned vertical shear with the same magnitude. By taking both magnitude and orientation into consideration, SH3-SH-5 is similar to SH3-SH3 in terms of its effect on suppressing tropical cyclogenesis. With this brief review, we then focus on the impact of vertical shear on the sensitivity of tropical cyclogenesis to ambient rotation.

It is found that tropical cyclogenesis is nearly insensitive to ambient rotation when the vertical shear is absent or very weak (Figure 4.5c,d and Figure 4.6c,d) but favored with a higher f when the vertical shear is strong (Figure 4.5a,b,e,f and Figure 4.6a,b,e,f).

The varying dependency on f emphasizes the role of vertical shear in regulating the intensification process. As discussed in the introduction, there is a precession process due to vertical shear and tropical cyclogenesis is intimately tied to the duration of this precession process. To see how this precession process is affected by ambient rotation, we show the evolutions of the vortex tilt in simulations initialized from a mid-level vortex in a 5 m s^{-1} westerly shear for different f. For f at 10^oN, the initialized vortex fails to intensify as the mid-level vortices rotate too slow and are advected away by the vertical shear (Figure 4.7); For f at 20 ^{o}N, the mid-level vortices rotate continuously against the vertical shear and succeed to realign with the lower-level vortices by Hour 120 (Figure 4.8); For f at 30^oN, the lower-level and mid-level vortices are already realigned by Hour 76 (Figure 4.9). This is consistent with the faster rotation rate of an adiabatic vortex with higher f found in

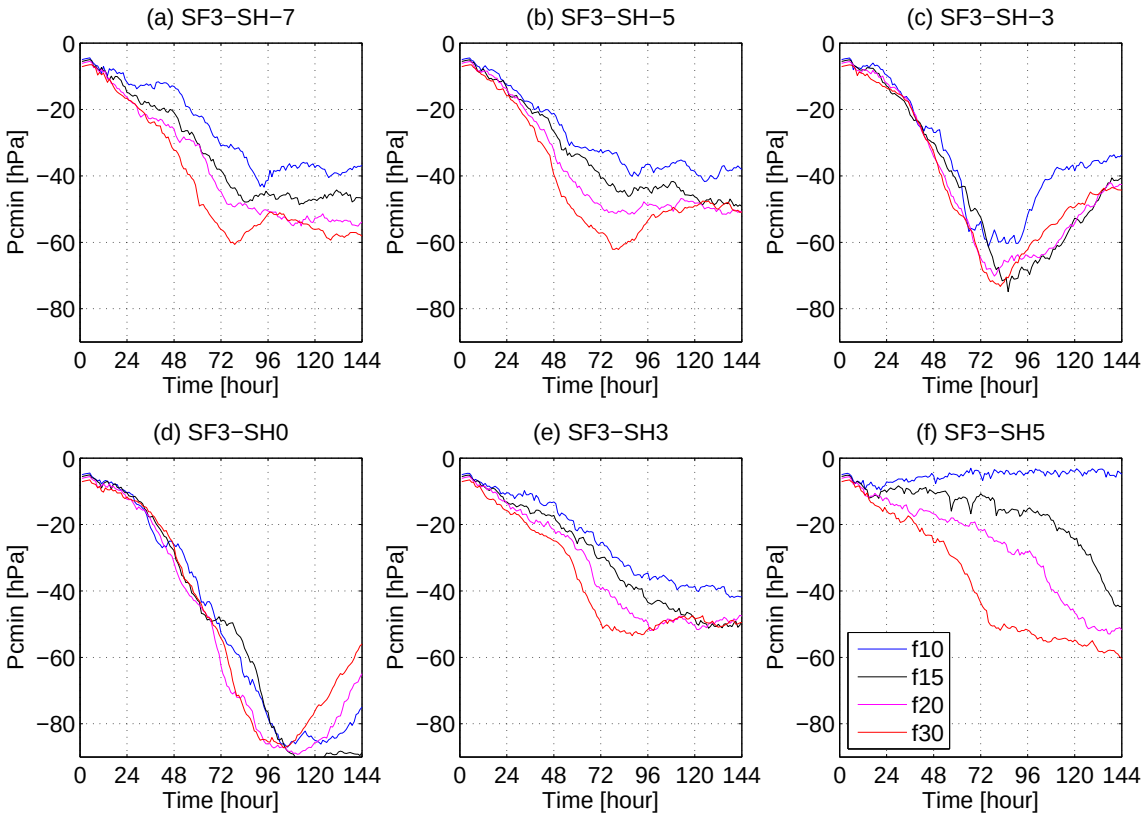

Figure 4.5: Time evolution of the minimum surface pressure in simulations initialized from a bottom vortex with a vertical shear of (a) easterly 7 m s^{-1}; (b) easterly 5 m s^{-1}; (c) easterly 3 m s^{-1}; (d) 0 m s^{-1}; (e) westerly 3 m s^{-1}; (f) westerly 5 m s^{-1}. The surface wind is 3 m s^{-1} westerly.

Jones (1995, 2000), due to the enhanced dynamical coupling between the low and mid-level vortices, as the Rossby penetration depth, $D_R = \frac{IL}{N}$ where I is the inertial instability, L is the length scale of the potential vorticity anomaly and N is the stratification stability, increases with f .

The magnitude and angle of vortex tilt and the local vertical shear are shown systematically for simulations initialized from the bottom and mid-level vortex (Figure 4.10). Following Zhang and Tao (2013), the centers of the lower-level (900 hPa) and mid-level (500 hPa) circulations are defined as the weighted center of the relative vorticity, and the local vertical shear is calculated as the difference between horizontal winds at the 900 hPa and 500 hPa levels averaged within a 300 km-radius circle centered on the 700-hPa circulation center. It

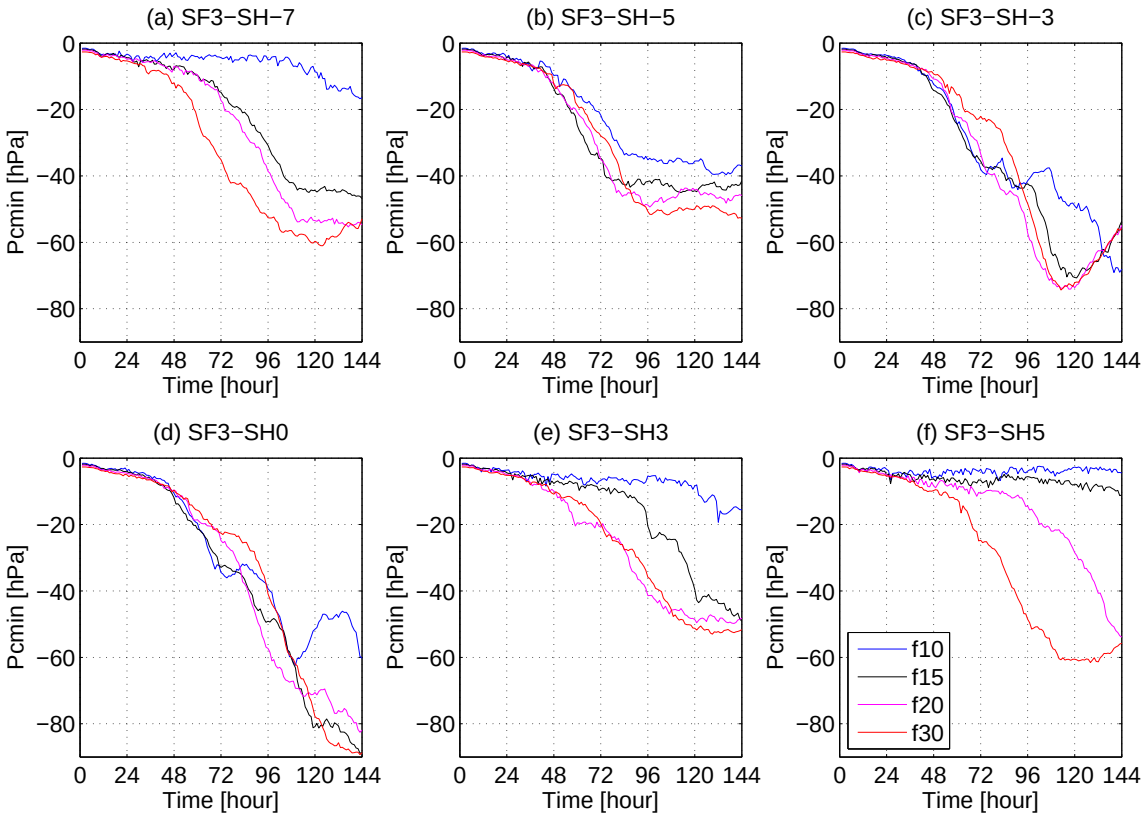

Figure 4.6: As in Figure 4.5 but for simulations initialized from a mid-level vortex.

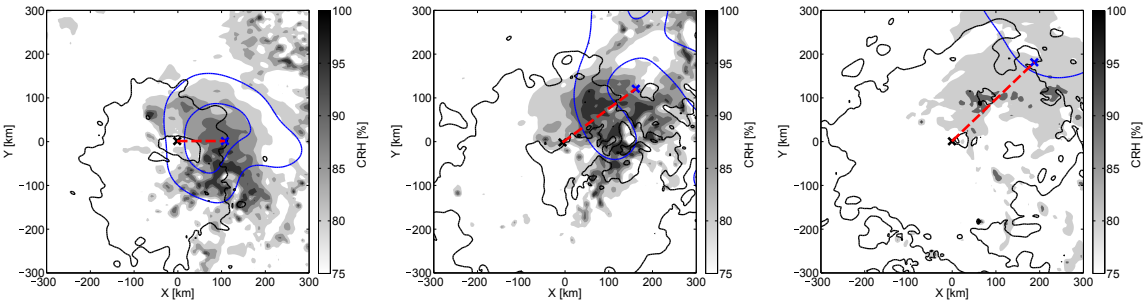

Figure 4.7: Surface pressure (black contour at each 5 hPa from 1010 hPa), smoothed relative vorticity at 500 hPa (blue contour at each 0.25 s^{-1} from 0.25 s^{-1}), and column-integrated relative humidity (shading) at Hour 24, 48 and 72 in the simulation with f at 10°N and initialized from a mid-level vortex in an environmental flow with a westerly surface wind of 3 m s^{-1} and a westerly wind shear of 5 m s^{-1}. The circulation center at 900 hPa is denoted as a black cross symbol and the circulation center at 500 hPa is denoted as a blue cross symbol.

is confirmed that the cyclonic rotation rate increases with f in both cases. Consistent with the finding in Rappin and Nolan (2012) and Zhang and Tao (2013), both the vortex tilt and the local wind shear felt by the vortex decrease rapidly when the mid-level vortices rotate

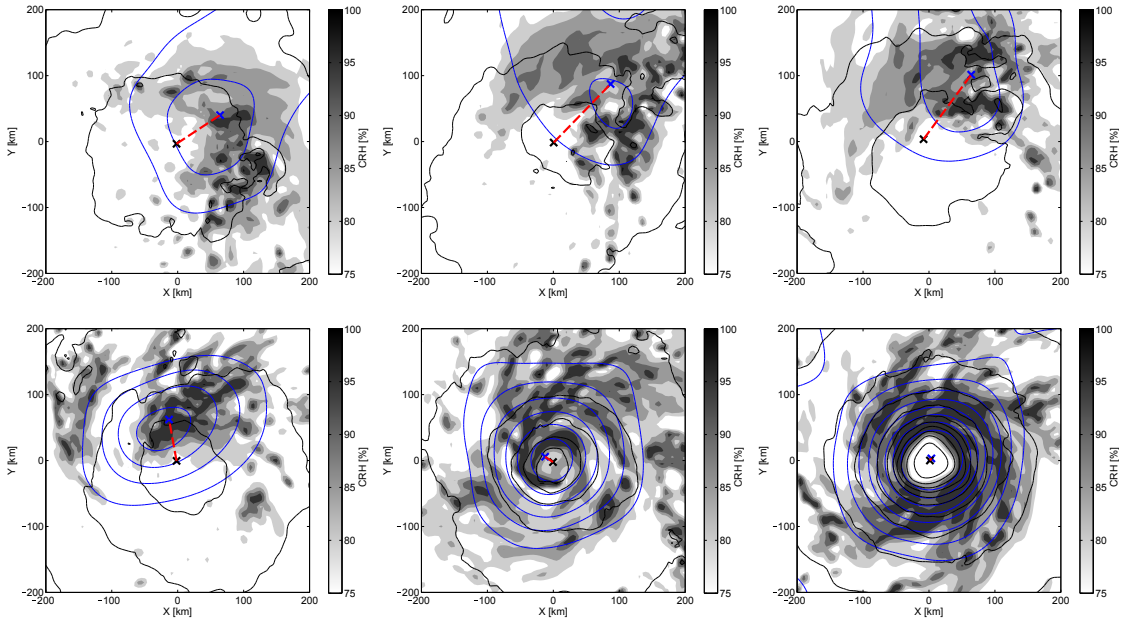

Figure 4.8: As in Figure 4.7 but with f at 20°N at Hour 24, 48, 72, 96, 120, 144 (from left to right; from top to bottom).

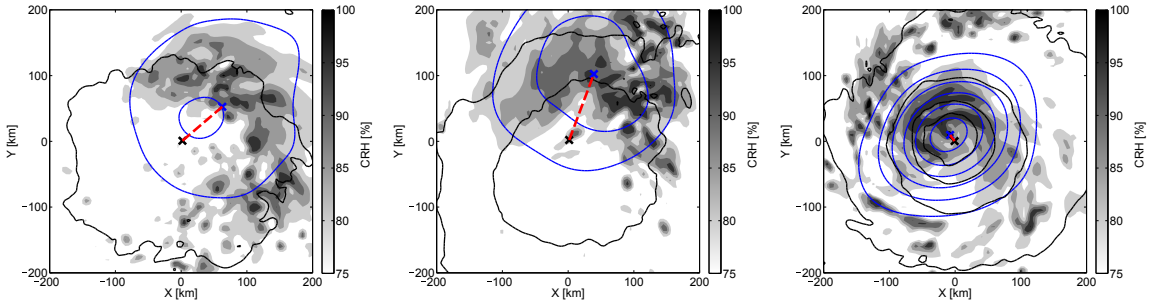

Figure 4.9: As in Figure 4.7 but with f at 30°N at Hour 24, 48, 72.

close to the left 90° of the wind shear direction, leading to the realignment of the vortex and rapid intensification.

4.4 Varying environmental thermodynamic state

The fact that tropical cyclogenesis is insensitive to ambient rotation in the environment without vertical shear (Figure 4.5d and Figure 4.6d) seems to be inconsistent with previous studies, which show tropical cyclones intensify faster with a lower f in a quiescent environment (Rappin et al., 2011; Smith et al., 2014; Miyamoto and Takemi, 2015). One might

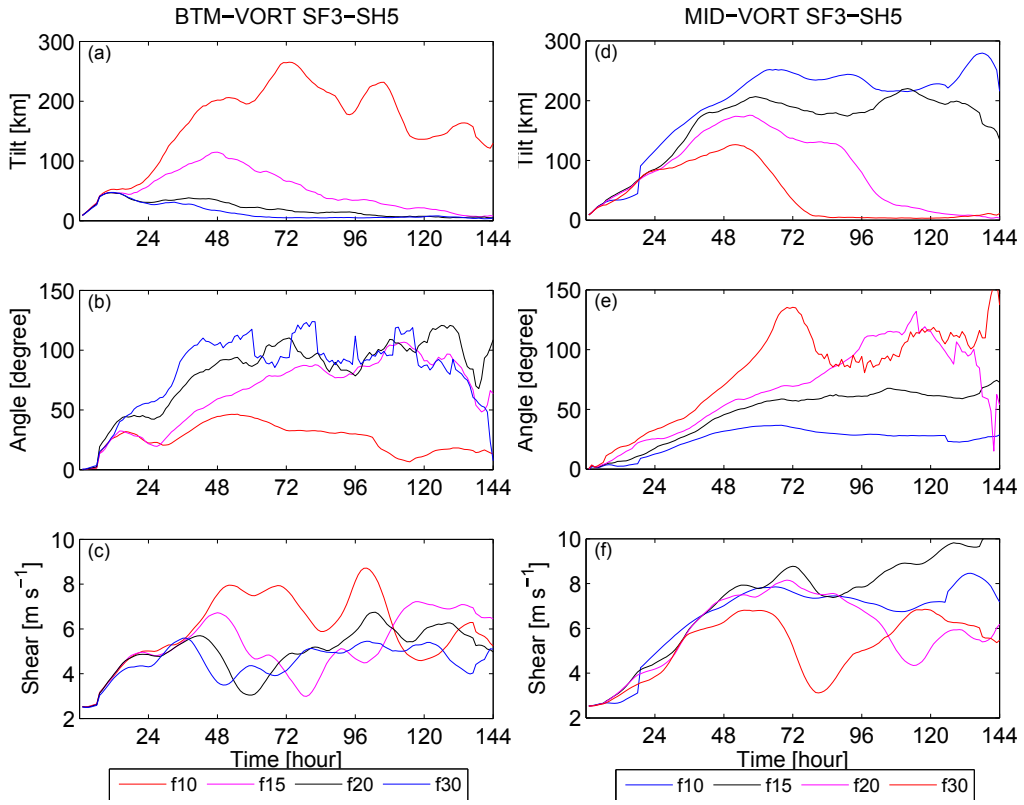

Figure 4.10: The magnitude (top) and angle (middle) of the tilt between the surface and the mid-level vortices and the magnitude of the local wind shear (bottom) in simulations with a 5 m s^{-1} westerly vertical shear initialized from a bottom (left) or mid-level (right) vortex.

think that the radiation and the mean flow make the difference here. However, as shown in Figure 4.12d, there is still no obvious sensitivity to f with the mean flow and radiation removed, as long as the environment is initialized from the RCE sounding. This leads us to investigate the sensitivity to the environment state in more detail. Particularly, three additional observational tropical soundings are considered for simulations initialized from a bottom vortex both in a quiescent environment and that with a 3 m s^{-1} westerly vertical shear.

It is confirmed that the intensification of tropical cyclones in vertical shear is always favored with a higher f, irrespective of the environmental thermodynamic state (Figure 4.11). Without vertical shear, the dependency of tropical cyclogenesis on ambient rotation is indeed sensitive to the environmental thermodynamic state (Figure 4.12). Tropical cyclones

intensify faster with a low f only when the environment is initialized with RE or Jordan sounding while there is no obvious sensitivity to ambient rotation for the MT and RCE soundings. It is worth noting that previous studies use the RE or Jordan sounding to initialize the environment (Rappin et al., 2011; Smith et al., 2014).

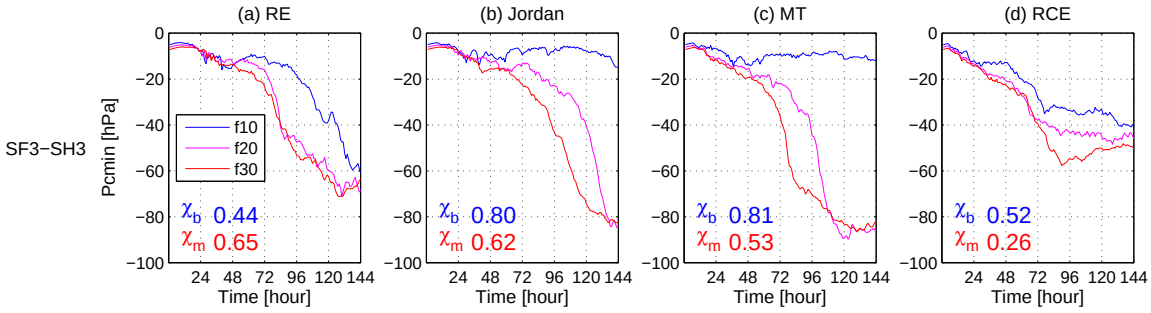

Figure 4.11: Time evolution of the minimum surface pressure in simulations with a 3 m s^{-1} westerly vertical shear for various initial environmental thermodynamic states.

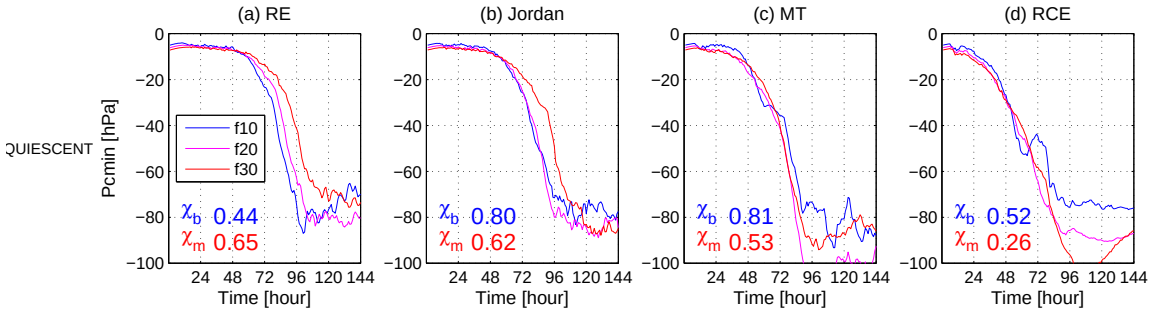

Figure 4.12: Time evolution of the minimum surface pressure in simulations with a quiescent environment for various initial environmental thermodynamic states.

As shown in Figure 4.4, one outstanding feature is that MT and RCE are significantly moister in the mid-troposphere compared to RE and Jordan, such that MT and RCE should be more thermodynamically favorable for convection. In order to describe the difference among these soundings more quantitatively, we have computed two characteristic parameters related to tropical cyclogenesis for each sounding: $\chi_b = \frac{s_b - s_m}{s_o^* - s_b}$ and $\chi_m = \frac{s_m^* - s_m}{s_o^* - s_b}$ where s_m^* is the saturation entropy in the mid-troposphere, s_m is the entropy in the mid-troposphere, s_o^* is the saturation entropy at sea surface temperature and s_b is the entropy in the boundary layer. Their values are listed in table 4.1.

Soundings	χ_b	χ_m
RE	0.44	0.65
Jordan	0.80	0.62
MT	0.81	0.53
RCE	0.52	0.26

Table 4.1: Characteristic parameters related to tropical cyclogenesis, χ_b and χ_m, computed from soundings.

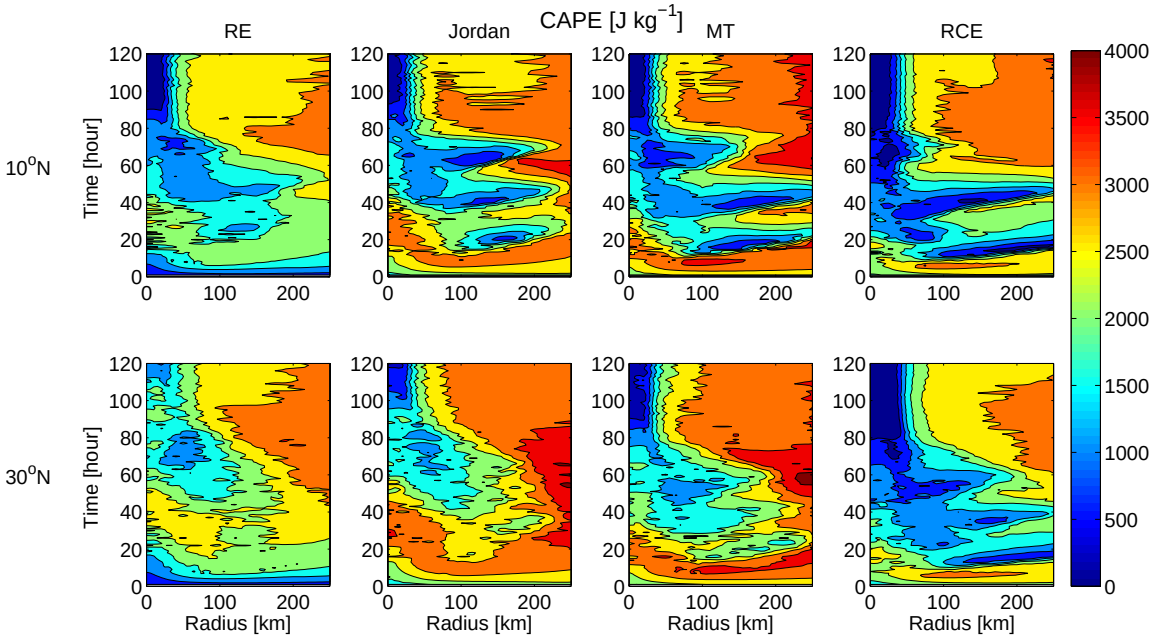

Figure 4.13: Time-radius cross-section of convective available potential energy (CAPE) in simulations with f at 10^0N (top) and 30^oN (bottom) for different environmental thermodynamic states.

Rappin et al. (2010) found that the time to genesis of tropical cyclones in environments of radiative-convective equilibrium with vertical shear is highly correlated with χ_b. Our simulations with observational tropical soundings confirm their conclusion, showing that the intensification of tropical cyclones in vertical shear is suppressed for those soundings with a larger χ_b (Figure 4.11). It is known that, with vertical shear, the low-entropy downdraft air from convection originating outside the eyewall can infiltrate the eyewall more efficiently through a low-level path (Tang and Emanuel, 2010; Riemer et al., 2010). In that sense, $\chi_b = \frac{s_b - s_m}{s_o^* - s_b}$ might be seen as a parameter measuring the destructive effect from the low-

entropy air to ventilate the eyewall, as indicated by the numerator, normalized by the effect of surface fluxes, as indicated by the denominator.

In literature, χ_m is sometimes considered equivalent to χ_b by assuming that the boundary layer entropy s_b is nearly equal to the saturation entropy of the mid-troposphere s_m^*. However, as shown in table 4.1, they are not always the same in these soundings due to the difference between s_b and s_m^*. Particularly, the ratio between χ_b and χ_m increases as the sounding becomes moister from RE to RCE. We then interpret χ_m as a different parameter from χ_b as follows. With the assumption of boundary-layer quasi-equilibrium (Raymond, 1995; Emanuel, 1995) and neglecting the large-scale vertical velocity at the cloud-base, the net convective updraft mass flux at the cloud base can be written as

$$M_u = \frac{C_k V_b (s_o^* - s_b)}{s_b - s_m}$$

where C_k is the surface exchange coefficient and V_b is the near-surface wind speed. One can then relate the time it takes for surface fluxes to moisten the mid-troposphere to saturation to χ_m as

$$\tau \simeq \frac{s_m^* - s_m}{M_u(s_b - s_m)} \sim \frac{s_m^* - s_m}{s_o^* - s_b} = \chi_m$$

Previous studies showed that the rapid development of deep convection in the inner region only occurs after the air column is sufficiently moistened and thermodynamically favorable for deep convection (Bister, 2001; Wang, 2014). A smaller χ_m indicates a shorter incubation time for this process of moisture precondition and thus speeds up the intensification process. However, a smaller χ_m should also enhance peripheral convection. The effect of peripheral convection on the intensification of tropical cyclones is studied in Bister (2001). They found that convection outside the eyewall leads to an increase of tangential wind in the outer region, a decrease of tangential wind and heating of the inner region. These changes will suppress the inner convection and delay the rapid intensification. In our simulations, the time to rapid intensification of tropical cyclones in a quiescent environment is positively

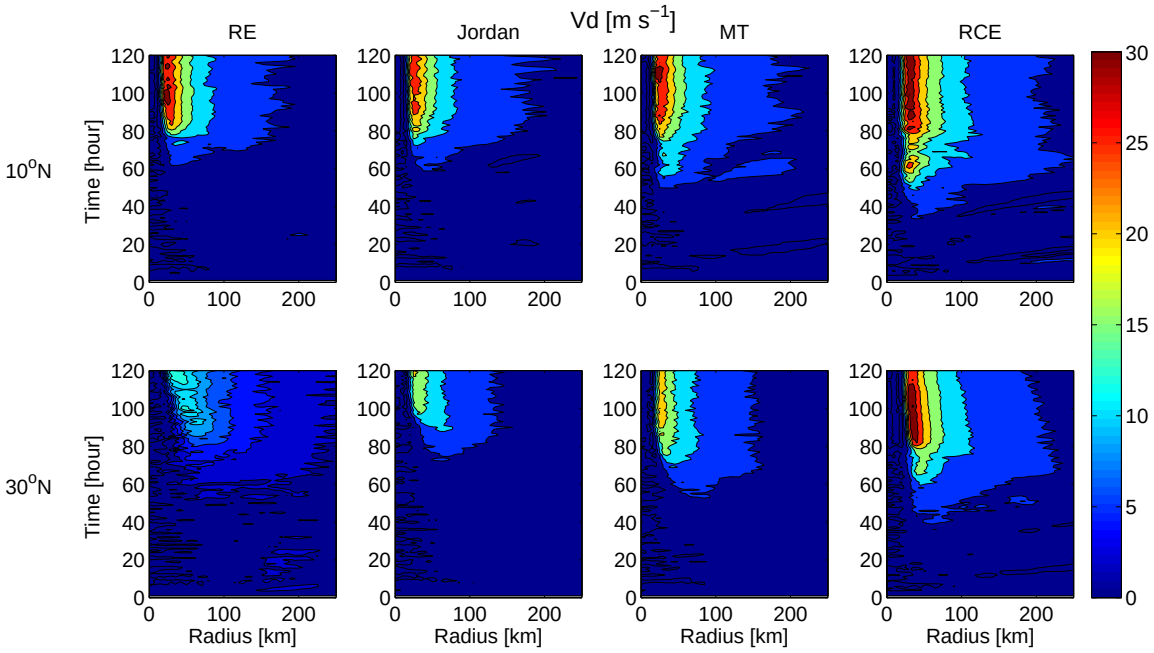

Figure 4.14: Time-radius cross-section of the radial flow in the boundary layer in simulations with f at 10^0N (top) and 30^oN (bottom) for different environmental thermodynamic states.

correlated with the parameter χ_m (Figure 4.12), which indicates the direct effect in the inner region dominates over the effect from peripheral convection. With this, we regard χ_m as an important parameter regulating the intensification of tropical cyclones in a quiescent environment.[1]

The physical mechanism for the more rapid intensification of tropical cyclones in a quiescent environment with a lower f has been comprehensively studied in Smith et al. (2014). It is found that, with a lower f, the boundary layer dynamics results in a stronger boundary layer inflow, which in turn leads to a stronger ascent of air exiting the boundary layer. The consequent larger diabatic heating rate and radial gradient at the eyewall induce enhanced convergence of angular momentum and thus more rapid intensification. For the RE sounding used in their simulations, the environmental thermodynamic state is not favorable

[1]We are aware that Tang and Emanuel (2012) actually use the same parameter to derive the ventilation index for tropical cyclones in wind shear. However, their interpretation of the numerator however is very different from us. In their formula, the numerator represents the entropy mixing between the environment and the core of TC in the mid-troposphere such that χ_m becomes an indicator for the strength of mid-level ventilation with wind shear.

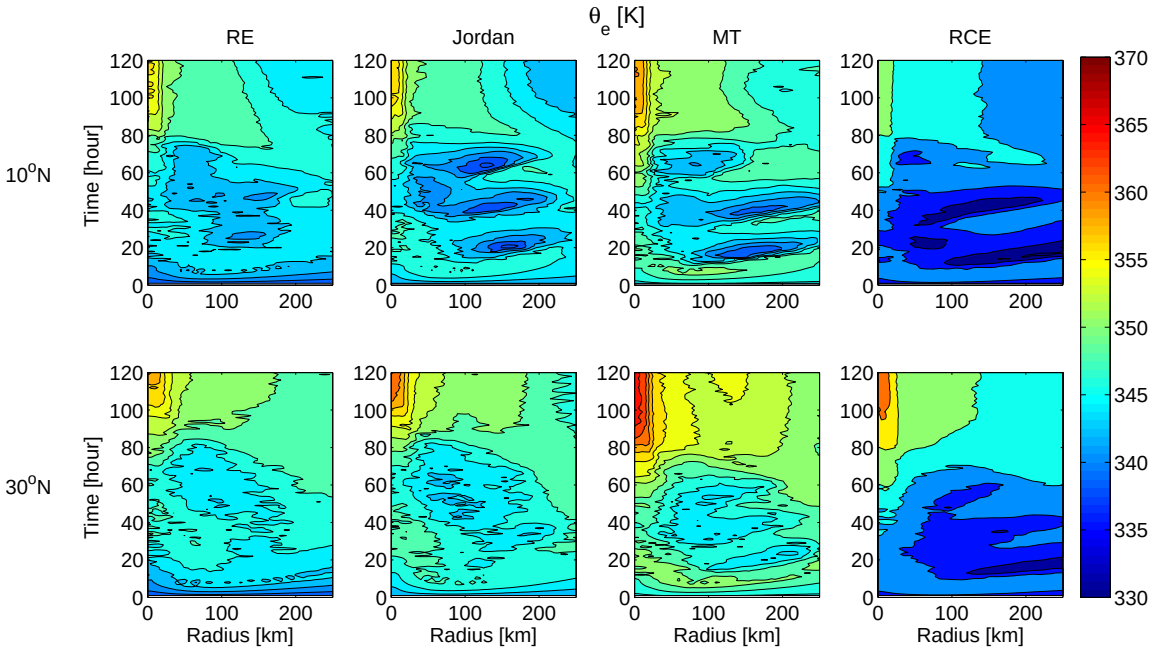

Figure 4.15: Time-radius cross-section of the equivalent potential temperature in the boundary layer in simulations with f at 10^0N (top) and 30^oN (bottom) for different environmental thermodynamic states

for convection as indicated by a large χ_m, such that the effect of peripheral convection is inactive in their simulations and thus not considered in their argument. For the RCE and MT soundings, the environment thermodynamic state is however favorable for convection as indicated by a smaller χ_m. The stronger ascent of air existing the boundary layer with a lower f (see Figure 2b in Smith et al. (2014)) will then also lead to enhanced peripheral convection outside the eyewall. Indeed, there is stronger activity of peripheral convection with a lower f, indicated by significant cycles of CAPE restoration and consumption (Figure 4.13), convection-triggered inflow pulses (Figure 4.14) and cooling of the boundary layer by strong downdrafts (Figure 4.15). Given the delay effect from peripheral convection, the faster tropical cyclogenesis with a lower f is neutralized. Particularly, we can see a significant slowdown of intensification for the simulation with the MT and RE sounding between Hour 60 and 80, when there is an active convection outside the eyewall.

To further verify the impact of χ_m on tropical cyclogenesis in a quiescent environment, we have performed two additional series of experiments initialized from: (1) the RE sounding

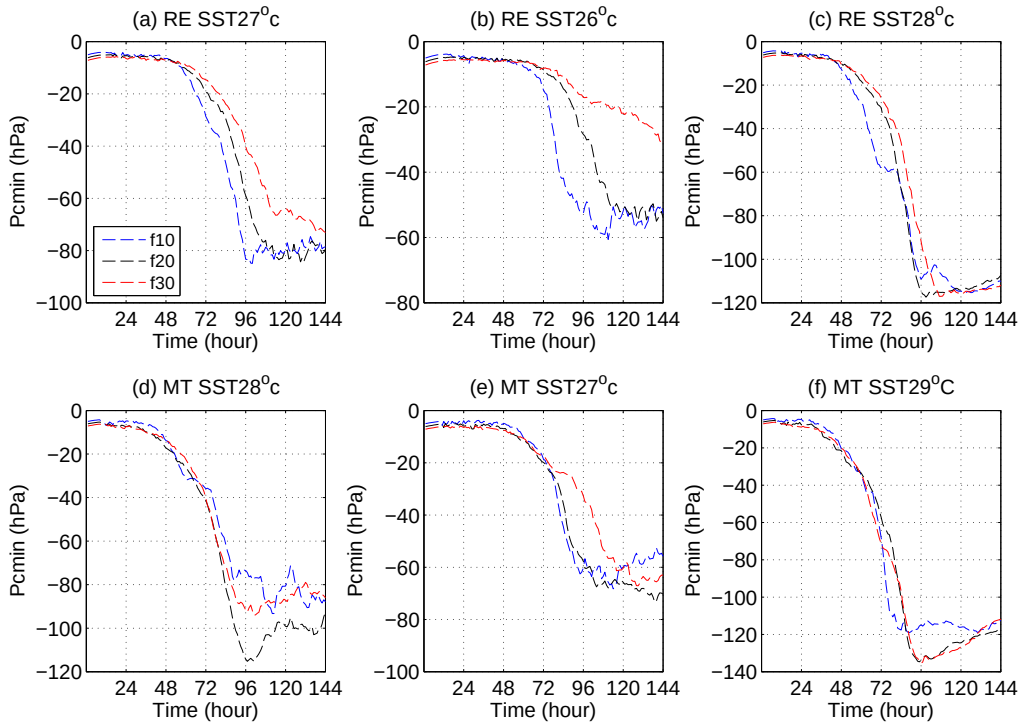

Figure 4.16: Time evolution of the minimum surface pressure in simulations initialized from the RE (top) and MT (bottom) soundings with varying SST. The environment is quiescent.

but with SST at 26°C and 28°C; (2) the MT sounding but with SST at 27°C and 29°C. As shown in Figure 4.16, since χ_m becomes smaller (larger) with a higher (lower) SST, tropical cyclones intensify faster (slower) and the faster intensification with a lower f is neutralized (enhanced). It is thus consistently found here that, for tropical cyclones in a quiescent environment, a smaller χ_m will not only result in a faster intensification due to a shorter time period of moist precondition in the inner region but also diminish the more rapid intensification with a lower f due to the effect from enhanced peripheral convection.

4.5 Preliminary results with the resolution and column physics of HiRAM

With a resolution of 50 km, Zhao et al. (2009) found that HiRAM is able to realistically simulate the observed global climatology and interannual variability of Hurricane frequency

(Figure 4.17). This promising result implies that the processes during tropical cyclogenesis could be well captured with the resolution of column physics of a mesoscale-resolution GCM.

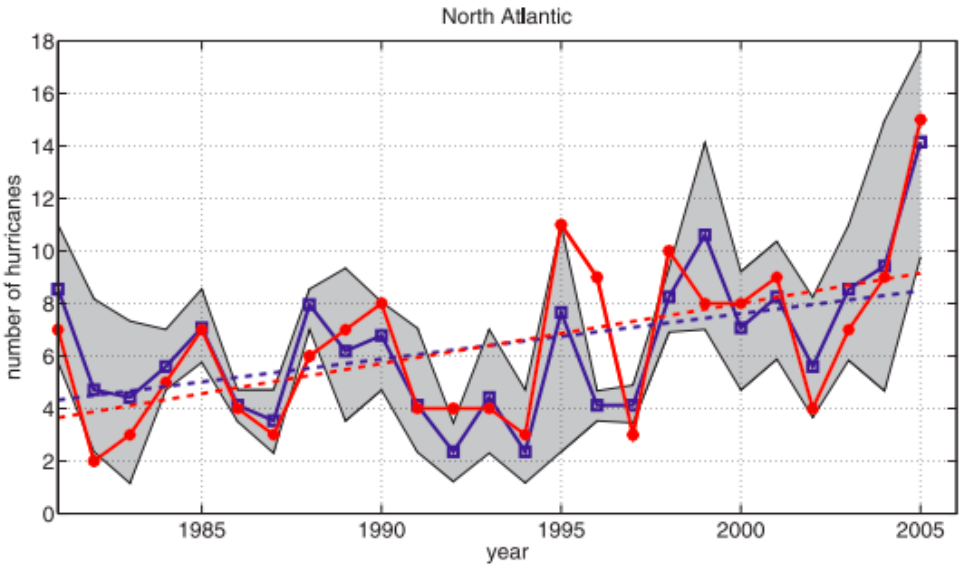

Figure 4.17: Interannual variation of hurricane numbers for North Atlantic from 1981 to 2005. IBTrACS observations (red) and four-member ensemble mean (blue); shaded area shows the simulated maximum and minimum number for each year. Model time series are normalized by time independent multiplicative factors so as to reproduce the observed total number. Dotted lines show observed and model linear trends (Zhao et al., 2009).

To provide further insights, analogous idealized simulations of tropical cyclogenesis with the resolution and column physics of HiRAM are conducted to be compared with WRF simulations. The time evolutions of the minimum surface pressure are shown in Figure 4.18 for simulations in a quiescent environment and in Figure 4.19 for simulations in an environment with a 3 m s^{-1} westerly shear.

By comparing Figure 4.18a with Figure 4.12b for the case initialized with a bottom vortex in a quiescent environment with the same Jordan sounding, we can see that there are considerable differences in the evolution of TC intensity between WRF and HiRAM run. Nevertheless, the faster intensification of tropical cyclones with a bottom vortex and a lower f is consistently captured (Figure 4.18). However, instead of the varying dependency on the Coriolis parameter due to vertical shear as found with cloud-resolving simulations, tropical cyclones still tend to intensify faster with a lower f initially with the vertical shear (Figure

4.19). It is also worth noting the curious result that, with vertical shear, tropical cyclogenesis is suppressed with f=10°N and 30°N but succeed to occur with a medium f=20°N.

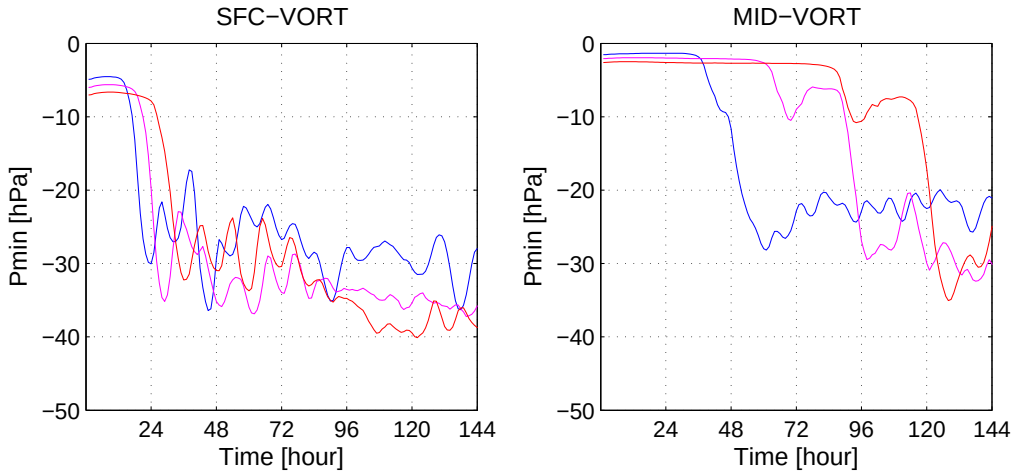

Figure 4.18: Time evolution of the maximum surface wind in simulations with the resolution and column physics of HiRAM at GFDL, initialized from a bottom (left) and mid-level (right) vortex in a quiescent environment.

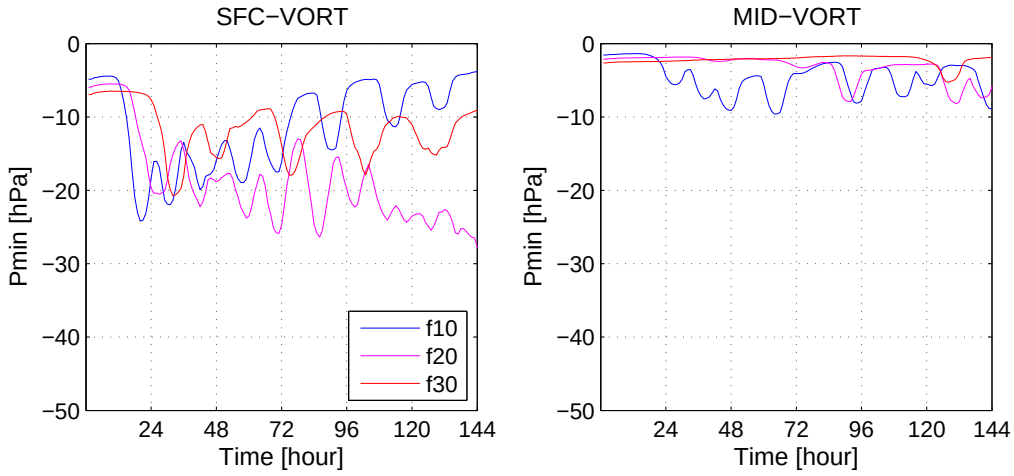

Figure 4.19: Time evolution of the maximum surface wind in simulations with the resolution and column physics of HiRAM at GFDL, initialized from a bottom (left) and mid-level (right) vortex in an environment with a 3 m s^{-1} westerly surface wind and a 3 m s^{-1} westerly vertical shear between 200 hPa and 850 hPa.

Such inconsistency between simulations of CRMs and GCMs implies the potential weakness of GCMs to capture certain aspects of tropical cyclogenesis, which might affect the

hurricane frequency simulated in their global simulations. Future work is desired to investigate the reasons for such inconsistency and how they are related to the behavior of tropical cyclogenesis in the global simulation.

4.6 Conclusions

Every year about 90 tropical cyclones develops over oceans. There is however no satisfactory theory to explain this number of tropical cyclones, or, to predict its response to future climate change. Alternatively, two different methods have been used to explore this question. First, empirical Genesis Potential Indexes (GPIs) have been developed according to the dependency of tropical cyclogenesis on large-scale environmental parameters (Gray, 1979; Emanuel and Nolan, 2004; Camargo et al., 2007; Emanuel, 2013; Camargo et al., 2014). One example introduced by Emanuel (2010) is shown below:

$$GPI = |\eta|^{3/2} \chi_b^{-4/3} MAX(V_P - 35, 0)^2 (25 + V_S)^{-2}$$

where η is the absolute vorticity at 850 hPa, χ_b is the same parameter discussed above in Section 4.4, V_P is the potential intensity, and V_S is the magnitude of the vertical wind shear between 850 hPa and 200 hPa. Second, for those GCMs that are able to realistically simulate the hurricane frequency in the current climate, one can use them to directly simulate the response of tropical cyclogenesis to climate change (Bengtsson et al., 2007; Zhao et al., 2009; Knutson et al., 2010; Bell et al., 2013; Kim et al., 2014b; Wehner et al., 2015). There are however limitations for both methods.

For the first method, while some GPIs work reasonably well in current climate to indicate the spatial and temporal variation of tropical cyclogenesis, there is no guarantee that these empirical GPIs fully capture the sensitivity of tropical cyclogenesis to large-scale environmental parameters that might be altered under future climate change. It is thus important to have a better physical understanding of the interactions between different large-scale envi-

ronment parameters during tropical cyclogenesis. In this study, tropical cyclogenesis from a preexisting disturbance is studied through idealized cloud-resolving simulations of the intensification of an incipient vortex in environments with various wind shear, ambient rotation and thermodynamics states.

We first investigate the sensitivity of tropical cyclogenesis to environmental rotation.

- With vertical shear, tropical cyclones intensify faster with a higher f, irrespective of the environmental thermodynamic state. The vertical shear develops a vertically tilted vortex, which undergoes a precession process with the mid-level vortices rotating cyclonically around the surface center. The rotation rate is controlled by the Rossby penetrating parameter, $\frac{IL}{N}$ (Jones, 1995). With a higher f, the mid-level vortices are able to rotate continuously against the vertical shear, leading to the re-alignment of the tilted vortex and rapid intensification of tropical cyclones. With a lower f, the cyclonic rotation is too slowly such that the mid-level vortices are advected away from the surface center by the vertical shear and tropical cyclogenesis is delayed or suppressed.

- Without vertical shear, the dependency of tropical cyclogenesis on f is sensitive to the environmental thermodynamic state. In an environment whose thermodynamic state is unfavorable for convection, tropical cyclones intensify faster with a lower f, in consistent with previous studies; while in an environment that is thermodynamically favorable for convection, there is no obvious sensitivity to f. The original faster intensification with a lower f is found to be offset by the delay effect from the enhanced peripheral convection.

The faster intensification of tropical cyclogenesis with a high f provides some physics basis for the positive dependency of GPI on f. We would also like to highlight that the dependency on f is sensitive to the vertical shear and such sensitivity is generally not considered in current GPIs.

We then consider the sensitivity of tropical cyclogenesis to environmental thermodynamic state.

- With vertical shear, tropical cyclogenesis is found to be regulated by the parameter $\chi_b = \frac{s_b - s_m}{s_o^* - s_b}$ which could be seen as an indicator of the effect of the low-entropy downdraft air ventilating the eyewall through the low-level path (Tang and Emanuel, 2010; Riemer et al., 2010).

- Without vertical shear, tropical cyclogenesis is found to be regulated by the parameter $\chi_m = \frac{s_m^* - s_m}{s_o^* - s_b}$ which measures the time it takes surface fluxes to moisten the mid-troposphere and thus the environmental thermodynamic favorability for deep convection. We also show that a smaller χ_m will not only lead to a faster intensification due to a shorter time period for moist precondition of the inner region but also diminish the more rapid intensification with a lower f due to the influence of enhanced peripheral convection.

It is worth noting that, in our experiments, an environment whose thermodynamic state is favorable for tropical cyclogenesis with vertical shear is not necessarily favorable for genesis without vertical shear.

Both incubation parameters, χ_b and χ_m, have been used in GPIs. For example, Emanuel (2010) use χ_b as in the above example, while Tang and Emanuel (2012) derive a ventilation index with χ_m. It is thus important to understand the response of these incubation parameters to future climate change. Rappin et al. (2010) show that χ_b in a radiative-convective equilibrium state increases with SST, as the increase in the saturation deficit in the mid-troposphere dominates over the increase of the surface disequilibrium. This increase of χ_b helps explain the general decrease of tropical cyclogenesis simulated by high resolution GCMs (Zhao et al., 2009; Knutson et al., 2010; Bell et al., 2013; Kim et al., 2014b; Wehner et al., 2015).

Held and Zhao (2011) investigate the correlation between the change in tropical cyclogenesis with global warming simulated by HiRAM and three large-scale environmental parameters, the vertical velocity at 500 hPa w_{500}, the Potential Intensity index and the vertical wind shear. They find the change in tropical cyclogenesis is best correlated with w_{500}. The correlation with w_{500} might be explained through the dependency of tropical cyclogenesis on the incubation parameter χ_m or χ_b as follows: First, w_{500} is usually positively correlated with the local SST relative to the tropical mean, which is further correlated with the surface disequilibrium; Second, w_{500} is negatively correlated with the saturation deficit in the mid-troposphere as argued in Held and Zhao (2011), and thus positively correlated with the nominator.

For the second method, despite the fact that more GCMs are able to realistically simulate the interannual variability and climatology of tropical cyclone frequency, it is not clear whether the various physical processes during tropical cyclogenesis with complex interactions between radiation, surface, moist convection and large-scale forcing can be fully simulated with the resolution and column physics of GCMs such that their predictions for future climate change would be reliable, assuming that accurate prediction of changes in large-scale environmental feasures were available. One way to test GCMs' ability in simulating tropical cyclogenesis is to perform analogous idealized simulations of tropical cyclogenesis from an incipient vortex and compare them with the cloud-resolving results.

We show some preliminary results from idealized simulations of tropical cyclogenesis with the resolution and column physics of HiRAM at GFDL in environments without and with vertical shear. Considerable differences are found between the simulation with HiRAM and that with WRF. For example, instead of the varying dependency on the Coriolis parameter due to the vertical shear as found in cloud-resolving simulations, tropical cyclones always intensify faster with a lower f with the resolution and column physics of HiRAM irrespective of the vertical shear. Future study is desired to investigate the reason for such inconsistency and how they are related to the behavior of tropical cyclogenesis in the global simulations.

One possibility, given the quality of the global simulations, is that the idealized initial condition of a weak vortex, might not be as relevant as other processes such as the evolution from tropical easterly waves or the breakdown of the intertropical convergence zone.

Chapter 5

Self-aggregation of convection

5.1 Introduction

We now return to non-rotating radiative-convective equilibrium (RCE) above a horizontally homogeneous surface, the simplest model for studying the statistically steady state of tropical convection. Such RCE is naturally assumed to be horizontally homogeneous, with convective cells randomly distributed. However, cloud-resolving simulation studies with both two-dimensional (e.g., Held et al., 1993; Tompkins, 2000) and three-dimensional geometries (e.g., Bretherton et al., 2005; Muller and Held, 2012; Wing and Emanuel, 2014) indicate that RCE with horizontally homogeneous convection can be unstable and yield spontaneous development of large-scale convective organization within tens of days, featuring a moist, convecting patch and a dry, non-convecting patch. Such phenomenon has been referred to as 'self-aggregation'. The aggregation of convection profoundly affects the domain-mean thermodynamic profile, thus adding more complexity to the RCE framework. Such spontaneous aggregation of convection however also provides an idealized framework to help us understand the frequently observed convective aggregation in the tropics, which has important impacts on both climate and weather. For example, Tobin et al. (2012) found a systematic dependence of water vapor, surface fluxes, and radiation on the degree of convective

aggregation in observations. Aggregated convection is found to be associated with lower free tropospheric humidity and reduced low- to mid-level cloudiness in the environment. Convective aggregation also plays an important role in processes such as squall lines (e.g. Houze, 1977), mesoscale convective system (e.g. Maddox, 1980), tropical cyclones (e.g. Simpson et al., 1997) and the Madden-Jullian Oscillation (e.g. Madden and Julian, 1971).

The mechanism for self-aggregation has been investigated in many studies. For two-dimensional geometry, Held et al. (1993) find that the water vapor field provides the memory to localize the convection. Tompkins (2000) shows that two-dimensional geometry encourages spontaneous large-scale organization, as areas far away from convection become very dry and thus inhibit convection there. For three-dimensional geometry, Bretherton et al. (2005) interpret self-aggregation as driven by the convection-water vapor-radiation feedbacks which dry the drier air columns and moisten the moister air columns while Muller and Held (2012) highlight the up-gradient energy transport by a large-scale circulation from the dry area to moister area induced from low-cloud top radiative cooling in the drier area. Moreover, Craig and Mack (2013) show that the moisture-convection feedback would lead to upscale growth of organization through a coarsening process. Emanuel et al. (2014) propose a theory of radiative-convective instability to explain the multi-equilibrium RCE with dry and moist state. The contribution of various feedbacks during the evolution of self-aggregation has been elucidated in Wing and Emanuel (2014) through the budget analysis for the spatial variance of column-integrated frozen moist static energy.

Self-aggregation has been found to be sensitive to both the domain size, horizontal grid resolution and sea surface temperature, with aggregation favored by larger domains, coarser horizontal grid resolution and higher SST (Muller and Held, 2012; Jeevanjee and Romps, 2013; Wing and Emanuel, 2014; Emanuel et al., 2014). Considering the domain size sensitivity, Muller and Held (2012) interpret it as due to the dependence of low clouds on domain size, while Jeevanjee and Romps (2013) conclude that cold pools are responsible for the domain size threshold. The favorability with higher SST is consistent with the theory of

radiative-convective instability (Emanuel et al., 2014) which suggests that above a critical SST, the ordinary RCE state with homogeneous convection becomes linearly unstable to large-scale overturning circulations and migrates toward one of the two stable equilibria, as the variations of the radiative cooling of the lower troposphere becomes governed principally by variations in upper tropospheric water vapor with a very large clear-sky infrared opacity of the lower troposphere. This dependency of self-aggregation on SST might have significant influence on climate change. As argued in Mauritsen and Stevens (2015), if precipitating convective clouds are more likely to cluster into larger clouds as temperatures rise, this process could constitute a plausible physical mechanism for an "iris effect" (Lindzen et al., 2001), which tends to enhance the hydrological change and decrease the climate sensitivity. It is however largely unknown how the temperature threshold for self-aggregation to occur will be sensitive to numerical models. Also, not much attention has been paid to the sensitivity to grid resolution. All the previous cited three-dimensional studies use the same cloud-resolving model except Jeevanjee and Romps (2013), who uses Das Atmosphrische Modell (DAM) (Romps, 2008). But the Romps (2008) simulation is initialized with an aggregated distribution of water vapor instead of a homogeneous state. It is thus worthwhile to investigate the sensitivity of self-aggregation to horizontal grid resolution and numerical models. In this paper, non-rotating radiative-convective equilibrium is simulated using both the System for Atmospheric Modeling (SAM, version 6.10.1) and the Weather Research and Forecasting Model (WRF, version 3.6). A full list of our experiments are summarized in Table 5.1.

Table 5.1: A list of our experiments

MODEL	INIT	RAD	SGS	SFC	MP	SA
SAM/res3km/29^oC/768km	RP	RRTM	TKE-Smag	MO	SAM1M	Y
	RP	RRTM	TKE-Smag	Const. Ck,d	SAM1M	Y
	RP	RRTM	TKE-Smag	Const. Ck,d	M2005	Y
SAM/res1km/29^oC/768km	RP	RRTM	TKE-Smag	MO	SAM1M	N
WRF/res3km/29^oC /768km	RP	RRTM-G	TKE-Smag	Const. Ck,d	WSM6	N
	RP	RRTM-G	TKE-Smag	MM5	WSM6	N
	RP	RRTM-G	PBL+HSmag	Const. Ck,d	WSM6	N
	RP	RRTM-G	TKE-Smag	Const. Ck,d	LIN	N
	RP	CAM	TKE-Smag	Const. Ck,d	WSM6	N
	MB1.5	RRTM-G	TKE-Smag	Const. Ck,d	WSM6	Y
	MB1	RRTM-G	TKE-Smag	Const. Ck,d	WSM6	N
WRF/res3km/31^oC/768km	RP	RRTM-G	TKE-Smag	Const. Ck,d	WSM6	N
WRF/res3km/33^oC/768km	RP	RRTM-G	TKE-Smag	Const. Ck,d	WSM6	N
WRF/res3km/35^oC/768km	RP	RRTM-G	TKE-Smag	Const. Ck,d	WSM6	N
WRF/res3km/29^oC/1536km	RP	RRTM-G	TKE-Smag	Const. Ck,d	WSM6	N
WRF/res3km/31^oC/1536km	RP	RRTM-G	TKE-Smag	Const. Ck,d	WSM6	N
WRF/res3km/33^oC/1536km	RP	RRTM-G	TKE-Smag	Const. Ck,d	WSM6	N
WRF/res3km/35^oC/1536km	RP	RRTM-G	TKE-Smag	Const. Ck,d	WSM6	Y

INIT: initial condition; **RP**: random temperature perturbation at the lower model levels; **MB1.5**: a moist bubble ($\triangle q_v$ =1.5 g kg^{-1}); **MB1**: a moist bubble ($\triangle q_v$ =1.0 g kg^{-1}); **RAD**: radiation scheme; **SGS**: subgrid mixing scheme; **SFC**: surface layer scheme; **MP**: microphysics scheme; **SA**: whether self-aggregation occurs or not.

The Chapter is organized as follows: We first review the self-aggregation behavior in the SAM model in Section 5.2. The sensitivity to microphysics, surface layer scheme and horizontal grid resolution is also discussed. The WRF results and sensitivity study are presented in Section 5.3. Discussion and conclusion are offered in Section 5.4.

5.2 SAM

SAM solves the anelastic mass continuity, momentum and tracer conservation equations. The prognostic thermodynamic variables are total non-precipitating water (vapor + cloud liquid + cloud ice), total precipitating water (rain snow and graupel) and liquid/ice water static energy (See details in Khairoutdinov and Randall (2003)).

The model uses 64 vertical levels with the model top at about 28 km and the lowest model level at about 37.5 m. The horizontal doubly-periodic domain has a size of 768 km $\times$ 768 km. The model is initialized from a mean sounding achieved in a small-domain (96 km $\times$ 96 km) RCE simulation and with random temperature perturbation at the lower model levels.

A one-moment microphysics scheme is used to handle the microphysical processes, with the cloud condensate and total precipitating water partitioned into hydrometer mixing ratio as a function of temperature. Radiative fluxes are computed using the RRTM radiation scheme (Mlawer et al., 1997; Clough et al., 2005), with a fixed zenith angle $u_o = 50.5^o$ and an incident solar flux $S_o = 650.83\ Wm^{-2}$. The subgrid mixing is computed using a TKE-Smagorinsky parameterization, with eddy diffusivity and viscosity coefficients related to the turbulence mixing length and the local subgrid turbulent kinetic energy (TKE). The turbulence mixing length is determined by the grid resolution and the local stratification, and TKE is diagnosed from the quasi-steady TKE budget. The underlying boundary is a saturated (ocean) surface with constant sea surface temperature at 29^oC. A simple surface layer scheme based on Monin-Obukhov similarity theory is used to compute the surface

fluxes. With all the above configurations, our experiment is identical to that in Wing and Emanuel (2014).

5.2.1 Control experiment

The control experiment uses a coarse resolution of 3 km following previous studies (Bretherton et al., 2005; Wing and Emanuel, 2014). Consistent with previous studies, self-aggregation occurs spontaneously in this SAM run. The instantaneous isosurfaces of condensate water content (precipitating + non-precipitating) and the column precipitable water (PW) throughout the 60-days simulation are shown in Figure 5.1.

The procedure of self-aggregation from homogeneous condition can be divided into three steps: (1) the spontaneous trigger of a sustainable area with drier columns (Figure 5.1a, b); (2) the expansion of the drier area and the concentration of the remaining moister area (from Figure 5.1c to 5.1d); (3) the maintenance of the separation. Following Wing and Emanuel (2014), the physical mechanisms responsible for each step can be quantitatively identified by estimating their contributions to the spatial variance of column-integrated frozen moist static energy (FMSE) according to the equation below:

$$\frac{1}{2}\frac{\partial \hat{h}'^2}{\partial t} = \hat{h}'SFX' + \hat{h}'LW' + \hat{h}'SW' + \hat{h}'CONV' \tag{5.1}$$

where $\hat{h}'$ is the anomaly to the domain mean of the column-integrated FMSE $h = C_pT + gz + L_vq - L_fq_{ice}$ which is conserved during moist processes in the model including the freezing and melting of precipitation, SFX' is the surface flux anomaly, SW' and LW' are the shortwave and longwave flux convergence anomalies and $CONV'$ is the horizontal FMSE convergence anomaly. The time evolution of contributions from various mechanisms, estimated by domain mean of terms in the $\hat{h}'^2$ budget, is shown in Figure 5.2. A positive value indicates a positive feedback to amplify convective aggregation with an increased variance of column-integrated FMSE. For the first step from Day 0 to about Day 30, small patches of drier columns are

produced where deep convection events decay as they condense out moisture within the columns. Within the drier patch, surface fluxes are reduced as a result of stagnant surface wind and radiative cooling is enhanced because of drier columns. A fortunate drier patch could then sustain itself against moistening from surrounding mixing through these positive feedbacks from surface fluxes and radiation during this period, as shown in Figure 5.2. For the second step from Day 30 to about Day 60, the drier patch expands because of the up-gradient energy transport by a large-scale circulation from the dry area to moister area induced from low-cloud top radiative cooling in the drier area (Muller and Held, 2012). This positive feedback from the up-gradient energy transport is also shown in Figure 5.2. Finally, the mature state is maintained by both shortwave and longwave feedbacks, with reduced shortwave heating and enhanced clear-sky longwave cooling due to warm and dry condition in the drier area (Bretherton et al., 2005).

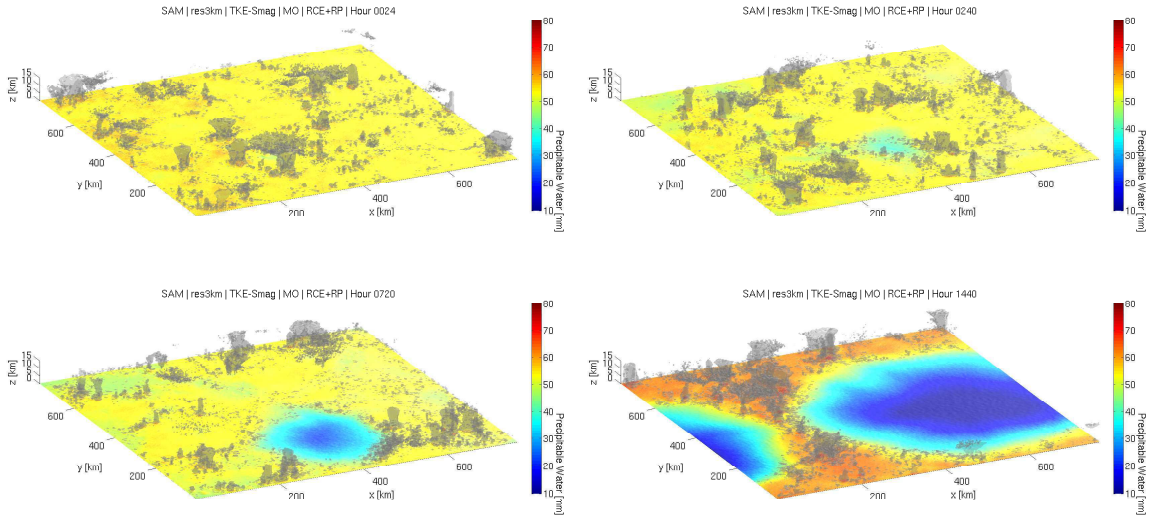

Figure 5.1: The instantaneous isosurface of condensate water content (0.05 g kg^{-1}) with column precipitable water (PW, in mm) for Day 1, 10, 30 and 60 in the control experiment using SAM model.

The variance of column relative humidity at 'aggregated' scale ($\triangle$**CRH**) is computed as an indicator of the degree of convection aggregation. Specifically, the domain has been divided into 64 boxes, each with 32×32 grids. A mean column relative humidity **CRH**, defined as the ratio of water vapor path in the column to the saturated water vapor path,

is then computed for each box. The difference between the maximum and minimum **CRH** can be used as an indicator of the degree of convection aggregation. As shown by the black solid line in Figure 5.3a, $\triangle$**CRH** for the control experiment continuously increases as the drier patch expands and reaches as large as 80% by the end of the 60-days simulation.

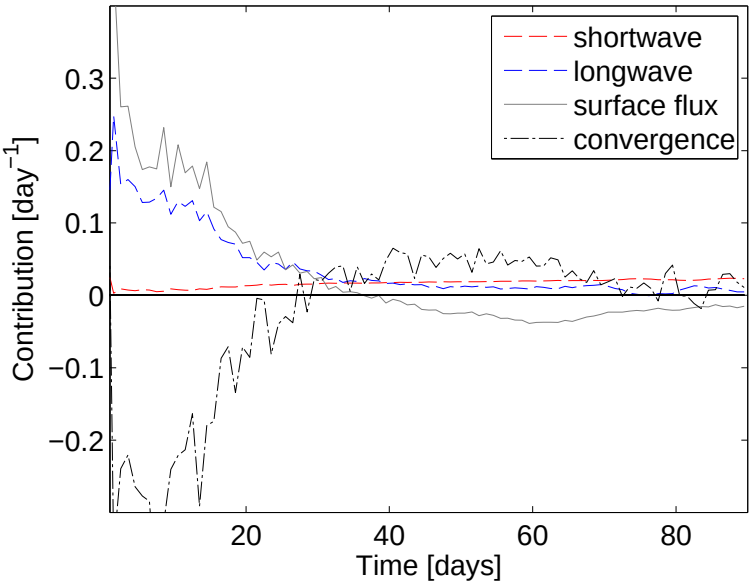

Figure 5.2: Time evolution of domain mean of terms in the $\hat{h}'^2$ budget, each normalized by $\hat{h}'^2$, with the unit of day^{-1}. Plotted is the correlation between vertically integrated column FMSE anomalies and column longwave flux convergence (blue), column shortwave flux convergence (red), surface enthalpy flux (black), and horizontal convergence of flux of FMSE (black dashed).

5.2.2 Sensitivity to horizontal grid resolution

As shown in Muller and Held (2012), the spontaneous aggregation of convection can be eliminated in this model in some cases with a finer horizontal grid resolution. This indicates the spontaneous aggregation of convection from homogeneous initial condition might be a numerical artifact that occurs at coarse resolutions. The largest domain used in Muller and Held (2012) is 512 km $\times$ 512 km and it is not clear whether self-aggregation will be recovered if a larger domain is used. Here a larger domain of 768 km $\times$ 768 km is used with horizontal

resolution of 1 km. As shown by the black dash line in Figure 5.3a, $\triangle$**CRH** keeps relatively small through our 60-day simulations and no self-aggregation occurs.

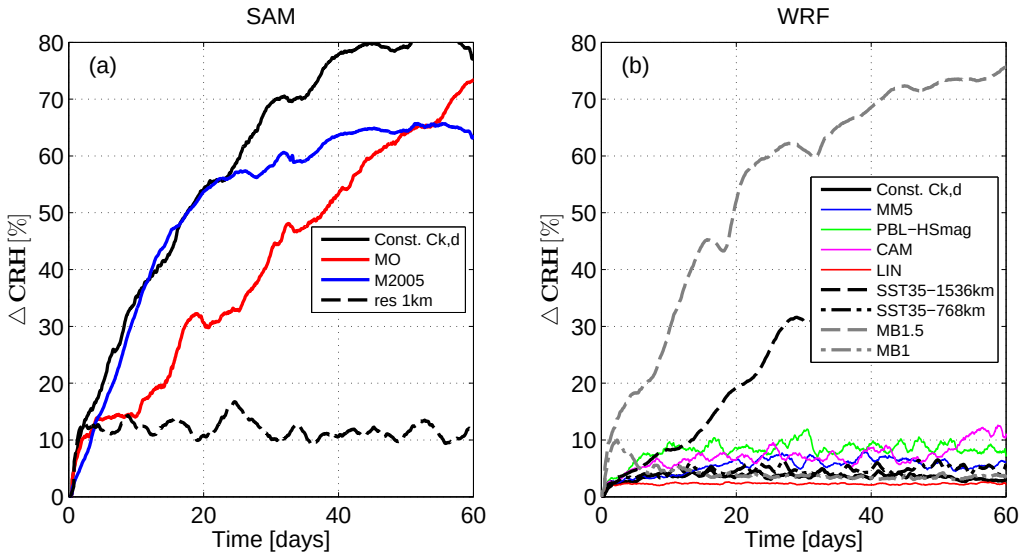

Figure 5.3: The variance of column relative humidity at 'aggregated' scale ($\triangle$**CRH**) as a function of time in various runs for (a) SAM and (b) WRF model.

The following picture helps explain this sensitivity to horizontal grid resolution. Whether a drier patch can sustain itself and allow for the following growth or otherwise be smoothed out by mixing should depend on two competing factors: the strength of the surrounding mixing and the size of the drier patch. An enhanced mixing will help smooth out the drier patch while a larger drier patch is more invulnerable to peripheral mixing and allows positive feedbacks to compete against the mixing. As shown in Figure 5.4, the size of convective cells becomes smaller with a finer grid resolution, and consequently the initial random drier patches will be smaller. Moreover, with finer resolution, we expect the flow to be more turbulent and more mixing from surrounding areas. It is thus less likely for a drier patch to sustain itself and self-aggregation is avoided.

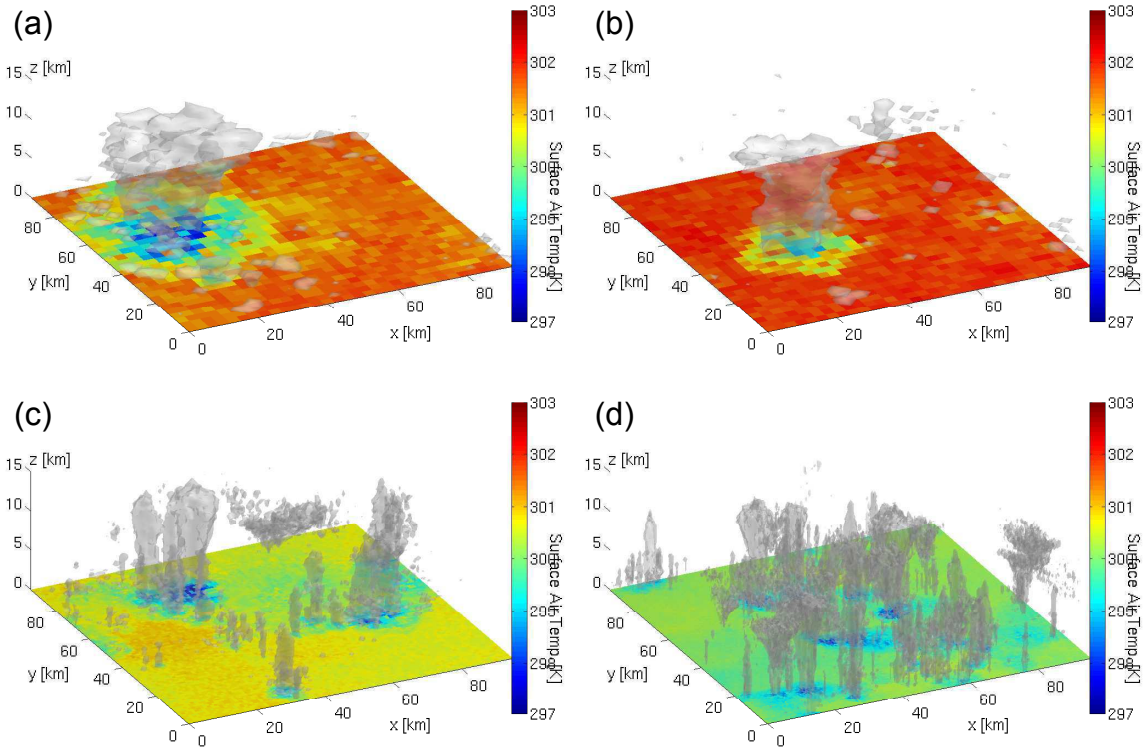

Figure 5.4: The instantaneous isosurface of condensate water content (0.05 g kg^{-1}) and near-surface air temperature (at the first model level of 37.5 m) in small-domain RCE simulations with SAM model and horizontal resolution of (a) 3 km (b) 3km but with the Morrison et al. (2005) microphysics; (c)1 km and (d) 0.5 km.

5.2.3 Sensitivity to microphysics scheme

Bretherton et al. (2005) found that self-aggregation could be affected by changes in the microphysics scheme. Particularly, self-aggregation is shown to be slowed down by increasing the threshold mixing ratio for auto conversion from cloud ice to snow. We perform one sensitivity test in which the default one-moment scheme is replaced by the (Morrison et al., 2005) double-moment, five-class bulk microphysics scheme. Convection is found to aggregate in a qualitatively similar manner to our control simulation, with the evolution of $\triangle$**CRH** shown as the blue line in Figure 5.3a. As shown in Figure 5.4b, the effect of microphysics scheme on the size of convective cells is not significant compared with that of horizontal grid resolution. With a similar size of convective cells, it is expected that self-aggregation occurs according to our argument above.

5.2.4 Sensitivity to surface flux scheme

To isolate the impact of the different surface flux scheme in two models, one additional case is conducted with surface fluxes computed from constant surface exchange coefficients:

$$C_K = C_D = 1.6 \times 10^{-3}$$

Convection aggregates in a similar manner to the control experiment, with the evolution of $\triangle$**CRH** shown as the red line in Figure 5.3a.

5.3 WRF

WRF is a fully compressible atmospheric model designed for mesoscale and convective-scale simulations of real and idealized weather. The prognostic equations are for the momentum, perturbation geopotential, perturbation potential temperature, perturbation surface pressure of dry air, and the mixing ratios of water contents (see details in Skamarock et al. (2008)).

The model uses 64 terrain-following mass vertical levels from $\eta = 1$ to $\eta = 0$, with the model top at about 28 km and the lowest model level at about 37.5 m. The horizontal doubly-periodic domain has a size of 768 km $\times$ 768 km with grid resolution of 3 km. The model is initialized from a mean sounding achieved in a small-domain (96 km $\times$ 96 km) RCE simulation and random temperature perturbation at the lower model levels.

Radiation physics is handled by the Rapid Radiative Transfer Model (RRTM-G, the version for application in GCMs) (Iacono et al., 2008), with the same fixed zenith angle $u_o = 50.5^o$ and solar constant $S_o = 650.83 Wm^{-2}$ used in SAM. The WRF single-moment 6-class scheme (Hong and Lim, 2006) is used for microphysical processes. The same TKE-Smagorinsky subgrid scheme used in SAM has been coded in WRF to handle the subgrid mixing. To isolate the effect of surface layer scheme and favor inter-model comparison,

the surface fluxes are computed with constant surface exchange coefficients: $C_K = C_D = 1.6 \times 10^{-3}$.

With all the above configuration, the WRF simulation is identical to the SAM simulation except the differences listed as follows: (1) Different dynamic core; (2) Different version of the same radiation scheme; (3) Different microphysical scheme. As we show in Section 5.3.2, the difference in physics should not be essential for the different behavior between SAM and WRF.

5.3.1 Control experiment

Instead of self-aggregation as seen in SAM run with the same coarse grid resolution of 3 km, there is no triggering of a sustainable drier patch and convection remains fairly homogeneous throughout the 60-days simulations (Figure 5.5). The variance of column relative humidity, $\triangle$**CRH**, as shown by the black solid line in Figure 5.3b, remains smaller than 10% throughout our 60-days run.

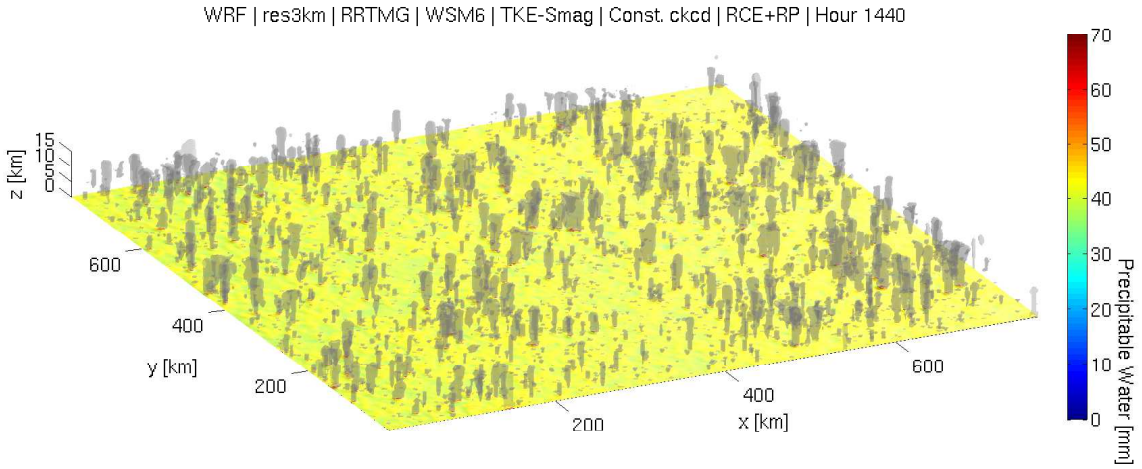

Figure 5.5: The instantaneous isosurface of condensate water content (0.05 g kg^{-1}) with column precipitable water (PW, in mm) for Day 60 in the control experiment using the WRF model.

As shown in Figure 5.6, one distinct difference between SAM and WRF is that: with the same coarse horizontal grid resolution of 3 km, the size of convective cells in WRF is much

smaller compared to those in SAM such that the drier patches within the domain might be too small to allow the positive feedbacks to compete against the surrounding mixing. There is also some sensitivity of the size of convective cells to the horizontal grid resolution in the WRF model but smaller compared to that in the SAM model.

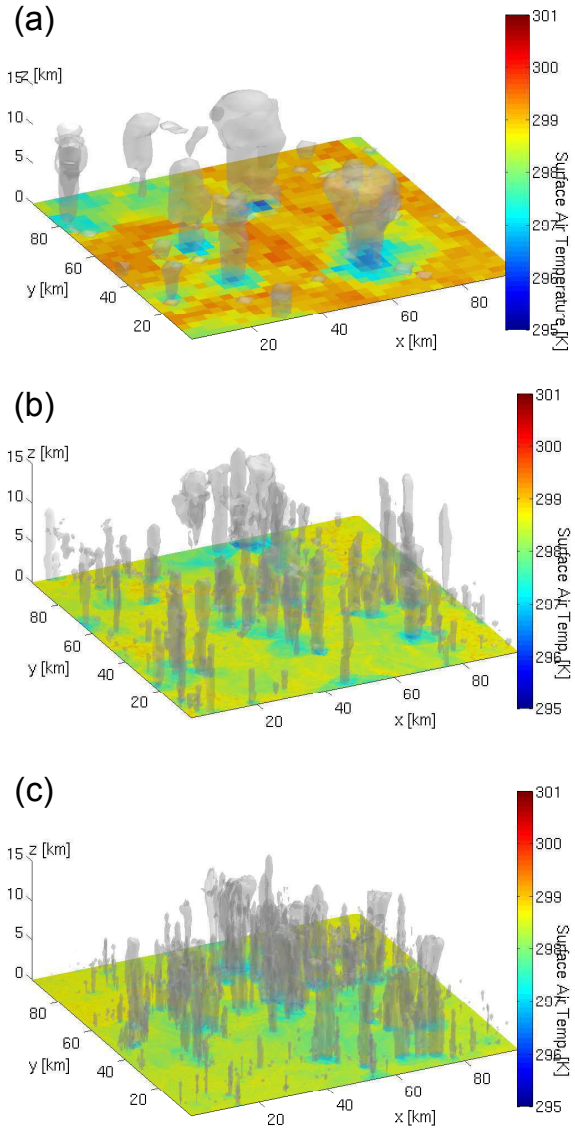

Figure 5.6: The instantaneous isosurface of condensate water content (0.05 g kg^{-1}) and near-surface air temperature (at the first model level of 37.5 m) in small-domain RCE simulations with WRF model and horizontal resolution of (a) 3 km (b) 1 km and (c) 0.5 km.

Given that the control experiment is absent of self-aggregation, we continue to investigate the sensitivity of the occurrence of self-aggregation in the WRF model to the physics scheme, initial perturbation and SST in the following sections.

5.3.2 Sensitivity to the physics schemes

In order to test the sensitivity to physical parameterizations, four additional runs with alternative physics schemes are conducted. First, instead of using constant surface exchange coefficients, a surface layer scheme based on Monin-Obukhov similarity theory is used; Second, the TKE-Smagorinsky subgrid scheme is replaced by a planetary boundary layer scheme (Yonsei University Planetary boundary layer scheme (Hong et al., 2006)) which handles the vertical mixing and a horizontal two-dimensional Smagorinsky scheme which handles the horizontal mixing; Third, the RRTM-G radiation scheme is replaced by the NCAR Community Atmosphere Model radiation scheme (CAM; Collins et al. (2006)); Finally, the WSM-6 microphysics scheme is replaced by the Lin 5-classes scheme (Lin et al., 1983). With all these changes, the convection remains non-aggregated in the WRF model with small $\triangle$**CRH** as shown in Figure 5.3b.

5.3.3 Sensitivity to the initial perturbation

In order to test the sensitivity to the initial perturbation, two additional runs with different initial perturbations are conducted: (1) instead of initializing from random temperature perturbation in the lower model levels, a moist bubble is added to the original moist field, as a function of height and the distance from the center of the domain:

$$\delta q_v = \triangle q_v cos^2(\frac{\pi}{2}((\frac{z-z_0}{z_0})^2 + (\frac{r}{L})^2))$$

where $z_0 = 1.5$ km is the center of the moist bubble, $L = 100$km is the horizontal scale and the maximum perturbation $\triangle q_v$ is 1.5 g kg^{-1}; (2) is identical to (1) but with $\triangle q_v$ reduced to

1.0 g kg^{-1}. Similar perturbation has been used in Muller and Held (2012) to investigate the hysteresis of self-aggregation with finer resolution. They find that hysteresis indeed exists as convective aggregation occurs at very fine resolutions (500 m) when initialized from a moist bubble as long as the domain size is large enough (300 km). Here, instead of resolution, we look at the model dependency.

In case (1) with $\triangle q_v = 1.5gkg^{-1}$, the initial moist bubble triggers local deep convection (Figure 5.7a) which condenses out most of the precipitable water within the columns and results in a drier patch in the center of the domain (Figure 5.7b) . The downdrafts from these deep convections trigger new convections at their outer edge, which also dry the columns and helps expand the drier area. The dry area reaches its maximum size near Day 2 (Figure 5.7c) and after that the mixing process smooths out its periphery. The dry area at the very center however remains (Figure 5.7d) and continues to expand (Figure 5.7e) until a mature state is reached (Figure 5.7f).

In case (2) with $\triangle q_v = 1.0gkg^{-1}$, as a weak initial moist bubble is used, the initial drier area resulted from the triggered deep convection is completely removed later by moistening from surrounding mixing and the convection quickly becomes homogeneous (Figure5.8).

5.3.4 Sensitivity to SST and domain size

Wing and Emanuel (2014) showed self-aggregation is favored with a warmer SST, probably due to the increased radiative-convective instability as discussed in Emanuel et al. (2014). A larger domain is however also needed for a warmer SST in their study. The physical reason for this requirement is not fully clear, as Emanuel et al. (2014) argues that the weaker subsidence due to the larger dry static stability occurring at a warmer SST necessitates a larger area. We then investigate the sensitivity to SST and domain size in the WRF model by increasing domain size and SST. With the default domain size of 768 km x 768 km, no self-aggregation is found even SST has been increased to 35 ^{o}C. With a large domain size of 1536 x 1536 km, self-aggregation is only found in the case with SST of 35°C (black dashed

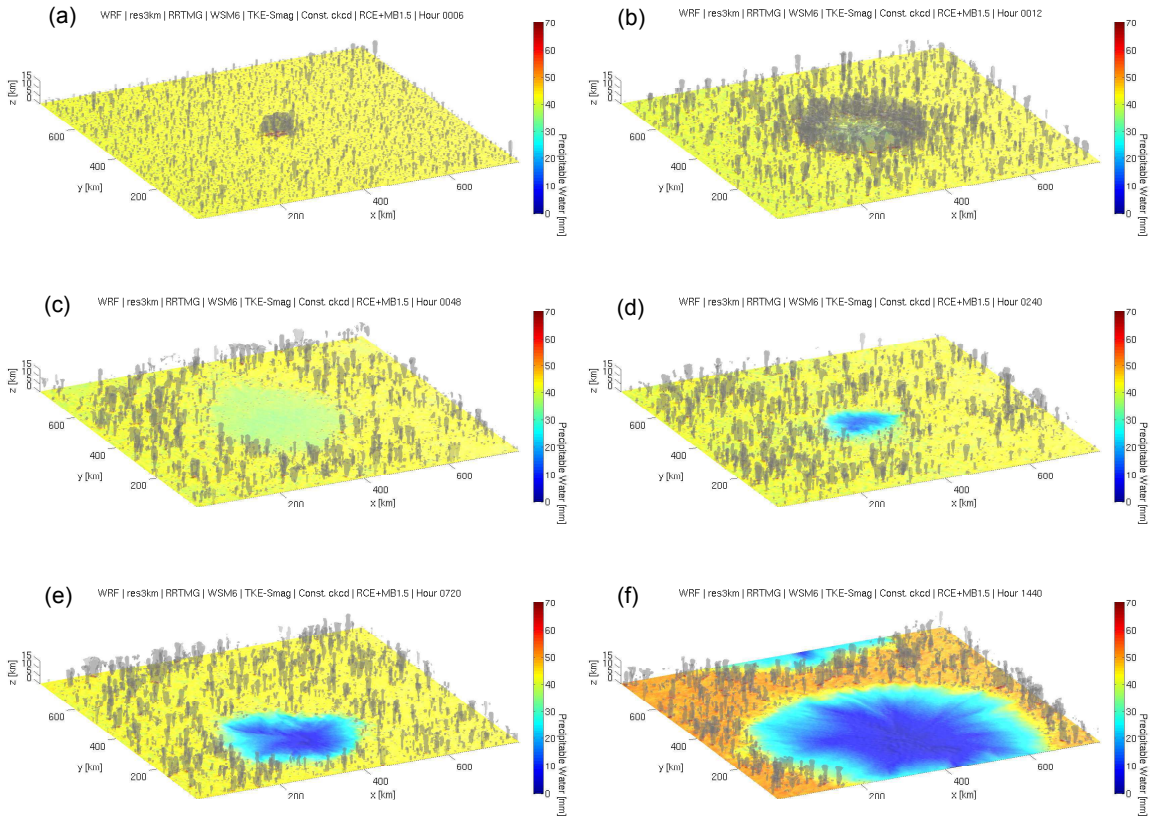

Figure 5.7: The instantaneous isosurface of condensate water content (0.05 g kg^{-1}) with column precipitable water (PW, in mm) for (a) Hour 6 and (b) Hour 12 , (c) Day 2, (d) Day 10, (e) Day 30 and (f) Day 60 in the WRF run initialized with a moist bubble ($\triangle q_v = 1.5$ g kg^{-1}) in the center of the domain.

line in Figure 5.3b). This is consistent with the previous conclusion that self-aggregation is favored with a larger domain and a higher SST. It also indicates that the critical SST for self-aggregation to occur in the WRF model is much higher than that of SAM model.

5.4 Conclusions

In this study, self-aggregation of convection from homogeneous radiative-convective equilibrium (RCE) has been studied with two cloud-resolving models: the System for Atmospheric Modeling (SAM, version 6.10.1) and the Weather Research and Forecasting Model (WRF, version 3.6). These two models simulate very different equilibria with the same coarse horizontal resolution of 3 km and SST of 29°C. In SAM, a sustainable drier patch appears within

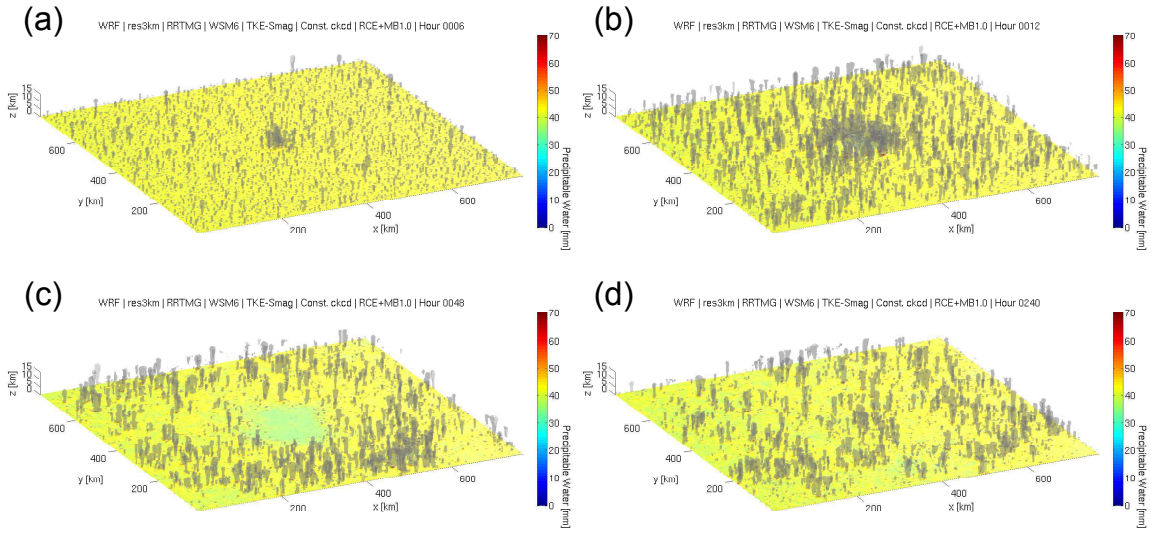

Figure 5.8: The instantaneous isosurface of condensate water content (0.05 g kg^{-1}) with column precipitable water (PW, in mm) for (a) Hour 6 and (b) Hour 12 , (c) Day 2, (d) Day 10 in the WRF run initialized with a moist bubble ($\triangle q_v = 1.0$ g kg^{-1}) in the center of the domain.

10 days, keeps expanding and finally divides the domain into one drier, non-convecting area and one moister, convecting area. Such behavior is well-known as 'self-aggregation' (Bretherton et al., 2005; Muller and Held, 2012; Jeevanjee and Romps, 2013; Wing and Emanuel, 2014). In WRF, no such sustainable drier patch is simulated and the convection remains fairly homogeneous. One distinct difference between the cloud fields simulated by SAM and WRF is that the size of convective cells in WRF is much smaller compared to that in SAM. The size of convective cell could be seen as a characteristic size for initial drier patches randomly produced within the domain. With a smaller initial size, the dry patch is less likely to sustain itself against surrounding mixing and the aggregation of convection is avoided. The reason for the different size of convective cells in these two models however is however not clear yet. It is most likely related to the difference in the implicit mixing in their dynamical cores, since the physics schemes used for these two models are the same. Indeed, by only increasing the grid horizontal resolution from 3 km to 1 km, self-aggregation of convection is also avoided in the SAM model as the size of convective cells becomes smaller.

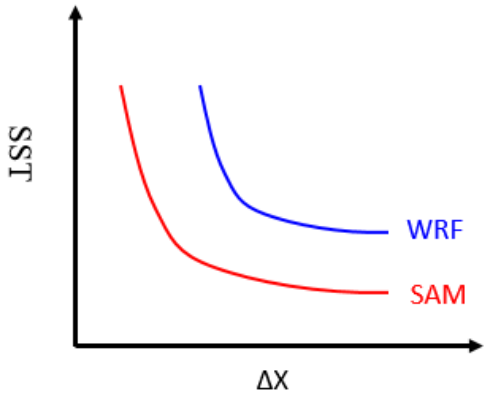

Figure 5.9: The schematic dependence of self-aggregation on sea surface temperature (SST) and the horizontal grid resolution ($\triangle X$) in SAM and WRF model. Above the curve, convection spontaneously aggregates if the domain size is large enough.

Self-aggregation of convection is recovered in the WRF model by increasing sea surface temperature to 35 ^{o}C together with the domain size. We then conclude that the critical SST for self-aggregation to occur is very sensitive to the model configuration, in the sense that the smaller convective cell the model simulates, the higher the critical SST could be. The dependence of self-aggregation on SST and horizontal resolution $\triangle X$ in SAM and WRF model is schematically illustrated in Figure 5.9, with self-aggregation much harder to achieve in the WRF model. The dependency of self-aggregation on SST might be related to how the degree of aggregation changes as climate warms and the consequences for the water vapor feedback and climate sensitivity. It is then important to understand the difference in this dependency among different models. Future work is desired to identify that why these two models simulate such different clouds characteristics and which one is more reasonable. We show that the cloud field is less sensitive to the horizontal resolution in the WRF model compared to that in the SAM model. In this sense, WRF seems to be a better model.

Self-aggregation of convection is also found in the WRF model initialized from a sufficient moist bubble. This further demonstrates the hysteresis of self-aggregation as found in Muller and Held (2012). We show that the initial moist bubble triggers deep convection which precipitates out the water in the column and induces a sustainable drier patch as it decays.

The drier patch then keeps expanding and leads to convective aggregation. It would be interesting to investigate whether the decay of deep convection in reality also helps induce convective organization.

Chapter 6

Conclusions

Tropical convection is studied in the idealized framework of radiative-convective equilibrium with both CRMs and GCMs. Particularly, we seek to further our understanding of tropical cyclones and self-aggregation of convection. The main results of this thesis are summarized and a number of future research directions are proposed for each topic.

6.1 Summary

In Chapter 2, rotating radiative-convective equilibrium (RRCE) is achieved by coupling the column physics of a global atmospheric model to rotating hydrostatic dynamics, along the line of Held and Zhao (2008) but with the column physics of AM2 replaced by that of a mesoscale resolution global atmospheric model, HiRAM, which produces quite realistic TC climatology when run with realistic boundary condition. We first examine RRCE achieved in a large doubly-periodic domain, which allows multiple tropical cyclones to exist simultaneously. The sensitivity of tropical cyclones to environmental parameters is investigated in this idealized geometry. We show that the intensity, radius of maximum wind and size of tropical cyclones increase with SST. The parameter study helps us bettter understand tropical cyclone simulations in the global model and also provides a reference point for future analogous studies with cloud resolving models. We then look at the variation of RRCE

with the domain size. As the domain size increases, the equilibrium state transitions from a weak tropical depression, to an unstable storm, to a single sustained storm, eventually to an equilibrium with multiple long-lived storms. The storm's size in the large domain can be related to this regime behavior.

In Chapter 3, we look at the effect of coupled SST on tropical cyclones by introducing a slab ocean model into RRCE. With coupled SST, we show that the eyewall region of tropical cyclones becomes cooler relative to the environment. The cooling originates from the negative shortwave cloud radiative effect and strong winds in the eyewall region, but is also modulated by a negative SST-surface-flux feedback, such that its magnitude increases as the depth of the slab ocean layer decreases but levels off as the depth approaches zero. The intensity reduction caused by the eyewall cooling in model simulations is found to be smaller than that estimated by Potential-Intensity theory, which underestimates the intensity of simulated tropical cyclones in cases with substantial eyewall cooling due to the fact that moist entropy is no longer well-mixed along angular momentum surfaces within the atmospheric boundary layer.

In Chapter 4, we explore the interactions between vertical shear, ambient rotation and thermodynamics during tropical cyclogenesis from a weak vortex in a small doubly-periodic f-plane through idealized cloud-system resolving simulations. Previous studies found that tropical cyclones intensify faster with a lower f in a quiescent environment. Our result however shows that the faster intensification can be neutralized by the suppression effect from the peripheral convection if the environment is thermodynamically favorable for convection. Also we show that in environments with vertical shear, tropical cyclogenesis is actually suppressed with a lower f due to the weaker coupling between the surface and the middle level. As for the favorability of the environmental thermodynamic state for tropical cyclogenesis, different thermodynamic parameters are found to control tropical cyclogenesis in environments with and without vertical shear. Particularly, an environment whose thermodynamic state is favorable for tropical cyclogenesis without wind shear is not necessarily also favorable

for tropical cyclogenesis with wind shear. To conclude, we find that vertical shear plays an important role in regulating the sensitivity of tropical cyclogenesis to both the ambient rotation and environmental thermodynamic state. Our preliminary result with the resolution and column physics of HiRAM at GFDL indicates that such role of wind shear might not be adequately represented in GCMs.

In Chapter 5, self-aggregation of convection from homogeneous radiative-convective equilibrium (RCE) has been studied with two cloud-resolving models: the System for Atmospheric Modeling (SAM) and the Weather Research and Forecasting Model (WRF). These two models simulate very different equilibria with the same horizontal resolution of 3 km and SST of 29°C. in the SAM model, a sustainable drier patch appears within 10 days, keeps expanding and finally divides the domain into one drier, non-convecting area and one moister, convecting area, consistent with many previous studies on self-aggregation. in the WRF model, no such sustainable drier patch is triggered and the convection remains homogeneous. Muller and Held (2012) found that self-aggregation can be avoid in the SAM with a resolution of 1 km or finer. A consistent result is found in this study with an even larger domain. One distinct difference between the control simulation of SAM and WRF or SAM with a higher resolution is that the convective cells in WRF and SAM with a higher resolution are much smaller compared to that in SAM control run. The size of convective cells could be seen as a characteristic size for initial drier patches randomly produced by the decay of deep convection. With a smaller initial size, the dry patch is less likely to sustain itself against surrounding mixing and the aggregation of convection is avoided. Self-aggregation is recovered in WRF by increasing sea surface temperature together with the domain size. This indicates that the critical SST for self-aggregation to occur is very sensitive to the model configuration, in the sense that the smaller the convective cells the model simulates, the higher the critical SST could be.

6.2 Directions for future research

6.2.1 Tropical cyclones

The sensitivity of TC size and intensity to SST has been studied in RRCE in Chapter 2. It would also be interesting to investigate the direct effect of CO2 concentration and solar insolation, motivated by simulations with global models, such as, Held and Zhao (2011) which found a decrease of hurricane frequency in response to a doubling of CO2 with fixed SST.

Potential-Intensity (PI) theory has been a widely-accepted index for predicting TC intensity. However, PI only provides an upper limit for TC intensity, which is rarely achieved by TCs in reality due to factors that is not considered by PI theory, such as ocean surface cooling induced by TCs themselves. The reduction effect of ocean surface cooling on TC intensity has been well-demonstrated through both observation and numerical studies (Leipper, 1967; Bender et al., 1993; Schade and Emanuel, 1999; Shen and Ginis, 2003; Zhu and Zhang, 2006). Lin et al. (2013) propose an ocean coupling potential index , which is found to be better correlated with the observed TC intensity compared to the original PI. However, their method does not consider the effect of ocean cooling on the surface disequilibrium by only modifying the term of thermodynamic efficiency. It seems that one can then extend their work by simply including the effect of ocean cooling on the surface disequilibrium. However as we show in Chapter 3, the effect of ocean cooling on TC intensity is smaller than that indicated by their direct influence on the surface disequilibrium, as the parameter $\alpha = \sqrt{\frac{dS}{dM}|_b / \overline{\frac{dS}{dM}}}$ becomes larger than 1 with the key assumption in PI theory that entropy and angular momentum are correlated in the atmospheric boundary breaking down. Future work is desired to quantitatively estimate the parameter α as a function of ocean surface cooling and propose an updated ocean coupling potential index for TC intensity.

As a naturally starting place from fixed-SST experiment, our study in Chapter 3 uses a simple slab ocean model to represent the coupling between ocean and atmosphere. To extend

our present work, the simple slab ocean model could be replaced with a dynamic ocean model such that the effect of upwelling and mixing from the subsurface can be included. However, the optimal way of doing this in a homogeneous framework requires further thought.

6.2.2 Tropical cyclogenesis

In Chapter 4, we found that the sensitivity of tropical cyclogenesis to large-scale environmental parameters, such as ambient rotation and thermodynamic state, could be largely modified due to the presence of vertical shear. Such complicated interactions are generally not considered in current GPIs. The insights we gain from these idealized simulations can be helpful for the future improvement of GPIs.

6.2.3 Convective organization

Mesoscale organized convection is frequently observed in the tropics, such small-scale organization can not be resolved by GCMs' coarse resolution. And it is also completely ignored by convective closures in the current generation of GCMs. Recent studies however show that the representation of convective organization in convective closures of GCMs might be crucial for better simulations of both large-scale circulation and small-scale flows (Tobin et al., 2012, 2013). In order to parameterize the effect of convective organization, one at least needs to have some knowledge of the relationship between the degree of convective organization and the large-scale environment state. While it is a good starting point to study self-aggregation in the framework of RCE, which allows one to generate atmospheric states that depend on a minimal number of explicitly controlled parameters and to study the sensitivity to these parameters, one would like to go beyond the RCE framework and look at systems with more degrees of freedom. For example, one can investigate the sensitivity of convective organization to large-scale environmental parameters, such as relative humidity in the mid-troposphere, by simulating self-aggregation in idealized environments with varying relative humidity.

6.2.4 Implications for testing GCM column physics

RRCE in a large domain provides an idealized framework for studying mature tropical cyclones simulated with GCM column physics, since TC characteristics are now intrinsically determined by excluding the large-scale dynamics and artificial boundary effect from the limited domain size. Ultimately, we would like to compare the simulations with GCM column physics to that with CRMs. However current computer resource still cannot afford systematic cloud-resolving simulations in such a large domain, unless one uses some unphysically large f to make the storm size smaller (Khairoutdinov and Emanuel, 2013).

RRCE in a small domain provides an idealized framework for studying tropical cyclogenesis from a weak vortex. Our preliminary study on analogous simulations of tropical cyclogenesis between GCMs and CRMs shows some encouraging results, however, the remaining inconsistency suggests further studies. Specifically, we would like to see whether the precession process of the tilted vortex in vertical shear as found in the cloud-resolving simulations is well simulated with the coarse resolution and convective parameterization of HiRAM.

Self-aggregation of convection from homogeneous non-rotating RCE provides an idealized framework to study convective organization. However, considerable model and resolution dependency has been found between two CRMs. Such dependency needs to be better understood before analogous GCM results can be compared fruitfully to CRMs.

Besides comparing with CRMs, it is also interesting to compare among various GCMs and see how their different resolution and column physics affect their simulations of mature tropical cyclones, tropical cyclogenesis and convective aggregation. For example, one can look at the sensitivity of convective self-aggregation to assumptions in GCMs' convective closures (e.g. Popke et al., 2013) and see how it might be related to a GCM' ability to simulate large-scale convective organization, such as the Madden-Jullian Oscillation and tropical cyclogenesis.

Bibliography

Arakawa, A., 2004: The Cumulus Parameterization Problem: Past, Present, and Future. *Journal of Climate*, **17 (13)**, 2493–2525.

Bechtold, P., J.-P. Chaboureau, A. Beljaars, A. K. Betts, M. Khler, M. Miller, and J.-L. Redelsperger, 2004: The simulation of the diurnal cycle of convective precipitation over land in a global model. *Quarterly Journal of the Royal Meteorological Society*, **130 (604)**, 3119–3137.

Bell, R., J. Strachan, P. L. Vidale, K. Hodges, and M. Roberts, 2013: Response of Tropical Cyclones to Idealized Climate Change Experiments in a Global High-Resolution Coupled General Circulation Model. *Journal of Climate*, **26 (20)**, 7966–7980.

Bender, M. A., I. Ginis, and Y. Kurihara, 1993: Numerical simulations of tropical cyclone-ocean interaction with a high-resolution coupled model. *Journal of Geophysical Research: Atmospheres*, **98 (D12)**, 23 245–23 263.

Bengtsson, L., K. I. Hodges, M. Esch, N. Keenlyside, L. Kornblueh, J.-J. Luo, and T. Yamagata, 2007: How may tropical cyclones change in a warmer climate? *Tellus A*, **59 (4)**, 539–561.

Bister, M., 2001: Effect of Peripheral Convection on Tropical Cyclone Formation. *Journal of the Atmospheric Sciences*, **58 (22)**, 3463–3476.

Bister, M. and K. A. Emanuel, 2002a: Low frequency variability of tropical cyclone potential intensity 1. Interannual to interdecadal variability. *Journal of Geophysical Research: Atmospheres*, **107 (D24)**, ACL 26–1–ACL 26–15.

Bister, M. and K. A. Emanuel, 2002b: Low frequency variability of tropical cyclone potential intensity 2. Climatology for 19821995. *Journal of Geophysical Research: Atmospheres*, **107 (D22)**, ACL 5–1–ACL 5–4.

Bracken, W. E. and L. F. Bosart, 2000: The Role of Synoptic-Scale Flow during Tropical Cyclogenesis over the North Atlantic Ocean. *Monthly Weather Review*, **128 (2)**, 353–376.

Bretherton, C. S., P. N. Blossey, and M. Khairoutdinov, 2005: An Energy-Balance Analysis of Deep Convective Self-Aggregation above Uniform SST. *Journal of the Atmospheric Sciences*, **62 (12)**, 4273–4292.

Bretherton, C. S., J. R. McCaa, and H. Grenier, 2004: A New Parameterization for Shallow Cumulus Convection and Its Application to Marine Subtropical Cloud-Topped Boundary Layers. Part I: Description and 1d Results. *Monthly Weather Review*, **132 (4)**, 864–882.

Brown, B. R. and G. J. Hakim, 2013: Variability and Predictability of a Three-Dimensional Hurricane in Statistical Equilibrium. *Journal of the Atmospheric Sciences*, **70 (6)**, 1806–1820.

Camargo, S. J., A. H. Sobel, A. G. Barnston, and K. A. Emanuel, 2007: Tropical cyclone genesis potential index in climate models. *Tellus A*, **59 (4)**, 428–443.

Camargo, S. J., M. K. Tippett, A. H. Sobel, G. A. Vecchi, and M. Zhao, 2014: Testing the Performance of Tropical Cyclone Genesis Indices in Future Climates Using the HiRAM Model. *Journal of Climate*, **27 (24)**, 9171–9196.

Chavas, D. R. and K. Emanuel, 2014: Equilibrium Tropical Cyclone Size in an Idealized State of Axisymmetric RadiativeConvective Equilibrium*. *Journal of the Atmospheric Sciences*, **71 (5)**, 1663–1680.

Chen, J.-H. and S.-J. Lin, 2012: Seasonal Predictions of Tropical Cyclones Using a 25-km Resolution General Circulation Model. *Journal of Climate*, 120713071748007.

Clough, S. A., M. W. Shephard, E. J. Mlawer, J. S. Delamere, M. J. Iacono, K. Cady-Pereira, S. Boukabara, and P. D. Brown, 2005: Atmospheric radiative transfer modeling: a summary of the AER codes. *Journal of Quantitative Spectroscopy and Radiative Transfer*, **91 (2)**, 233–244.

Collins, W. D., et al., 2006: The Formulation and Atmospheric Simulation of the Community Atmosphere Model Version 3 (CAM3). *Journal of Climate*, **19 (11)**, 2144–2161.

Craig, G. C. and J. M. Mack, 2013: A coarsening model for self-organization of tropical convection. *Journal of Geophysical Research: Atmospheres*, **118 (16)**, 8761–8769.

Derbyshire, S. H., I. Beau, P. Bechtold, J.-Y. Grandpeix, J.-M. Piriou, J.-L. Redelsperger, and P. M. M. Soares, 2004: Sensitivity of moist convection to environmental humidity. *Quarterly Journal of the Royal Meteorological Society*, **130 (604)**, 3055–3079.

Dunion, J. P., 2011: Rewriting the Climatology of the Tropical North Atlantic and Caribbean Sea Atmosphere. *Journal of Climate*, **24 (3)**, 893–908.

Emanuel, K., 2010: Tropical Cyclone Activity Downscaled from NOAA-CIRES Reanalysis, 19081958. *Journal of Advances in Modeling Earth Systems*, **2 (1)**, 1.

Emanuel, K. and R. Rotunno, 2011: Self-Stratification of Tropical Cyclone Outflow. Part I: Implications for Storm Structure. *Journal of the Atmospheric Sciences*, **68 (10)**, 2236–2249.

Emanuel, K., A. A. Wing, and E. M. Vincent, 2014: Radiative-convective instability. *Journal of Advances in Modeling Earth Systems*, **6 (1)**, 75–90.

Emanuel, K. A., 1986: An air-sea interaction theory for tropical cyclones. Part 1: Steady-state maintenance. *Journal of the Atmospheric Sciences*, **43 (6)**, 585–604.

Emanuel, K. A., 1991: The Theory of Hurricanes. *Annual Review of Fluid Mechanics*, **23 (1)**, 179–196.

Emanuel, K. A., 1995: The Behavior of a Simple Hurricane Model Using a Convective Scheme Based on Subcloud-Layer Entropy Equilibrium. *Journal of the Atmospheric Sciences*, **52 (22)**, 3960–3968.

Emanuel, K. A., 2013: Downscaling CMIP5 climate models shows increased tropical cyclone activity over the 21st century. *Proceedings of the National Academy of Sciences of the United States of America*, **110 (30)**, 12 219–12 224.

Emanuel, K. A. and D. S. Nolan, 2004: Tropical cyclone activity and global climate. *26th Conf. on Hurricanes and Tropical Meteorology*, 240–241.

Frierson, D. M. W., 2007: The Dynamics of Idealized Convection Schemes and Their Effect on the Zonally Averaged Tropical Circulation. *Journal of the Atmospheric Sciences*, **64 (6)**, 1959–1976.

Futyan, J. M. and A. D. Del Genio, 2007: Deep Convective System Evolution over Africa and the Tropical Atlantic. *Journal of Climate*, **20 (20)**, 5041–5060.

GAMDT, 2004: The New GFDL Global Atmosphere and Land Model AM2LM2: Evaluation with Prescribed SST Simulations. *Journal of Climate*, **17 (24)**, 4641–4673.

Garner, S., 2014: The relationship between hurricane potential intensity and CAPE. *Journal of the Atmospheric Sciences*.

Ge, X., T. Li, and M. Peng, 2013: Effects of Vertical Shears and Midlevel Dry Air on Tropical Cyclone Developments*. *Journal of the Atmospheric Sciences*, **70 (12)**, 3859–3875.

Ge, X., T. Li, and M. S. Peng, 2011: Tropical Cyclone Genesis Efficiency: Mid-Level Versus Bottom Vortex. Tech. rep.

Gray, W. M., 1968: Global view of the origin of tropical disturbances and storms. *Monthly Weather Review*, **96 (10)**, 669–700.

Gray, W. M., 1979: Hurricanes: Their formation, structure and likely role in the tropical circulation. Meteorology over the Tropical Oceans. *Royal Meteorological Society*, 155–218.

Guichard, F., et al., 2004: Modelling the diurnal cycle of deep precipitating convection over land with cloud-resolving models and single-column models. *Quarterly Journal of the Royal Meteorological Society*, **130 (604)**, 3139–3172.

Hakim, G. J., 2011: The Mean State of Axisymmetric Hurricanes in Statistical Equilibrium. *Journal of the Atmospheric Sciences*, **68 (6)**, 1364–1376.

Hakim, G. J., 2013: The Variability and Predictability of Axisymmetric Hurricanes in Statistical Equilibrium. *Journal of the Atmospheric Sciences*, **70 (4)**, 993–1005.

Held, I. M., 2005: The Gap between Simulation and Understanding in Climate Modeling. *Bulletin of the American Meteorological Society*, **86 (11)**, 1609–1614.

Held, I. M., R. S. Hemler, and V. Ramaswamy, 1993: Radiative-Convective Equilibrium with Explicit Two-Dimensional Moist Convection. *Journal of the Atmospheric Sciences*, **50 (23)**, 3909–3927.

Held, I. M. and M. Zhao, 2008: Horizontally Homogeneous Rotating Radiative-Convective Equilibria at GCM Resolution. *Journal of the Atmospheric Sciences*, **65 (6)**, 2003–2013.

Held, I. M. and M. Zhao, 2011: The Response of Tropical Cyclone Statistics to an Increase in CO2 with Fixed Sea Surface Temperatures. *Journal of Climate*, **24 (20)**, 5353–5364.

Held, I. M., M. Zhao, and B. Wyman, 2007: Dynamic RadiativeConvective Equilibria Using GCM Column Physics. *Journal of the Atmospheric Sciences*, **64 (1)**, 228–238.

Hong, S. and J. Lim, 2006: The WRF singlemoment 6class microphysics scheme (WSM6). *J. Korean Meteor. Soc.*, **42 (2)**, 129–151.

Hong, S.-Y., Y. Noh, and J. Dudhia, 2006: A New Vertical Diffusion Package with an Explicit Treatment of Entrainment Processes. *Monthly Weather Review*, **134 (9)**, 2318–2341.

Houze, R. A., 1977: Structure and Dynamics of a Tropical SquallLine System. *Monthly Weather Review*, **105 (12)**, 1540–1567.

Iacono, M. J., J. S. Delamere, E. J. Mlawer, M. W. Shephard, S. A. Clough, and W. D. Collins, 2008: Radiative forcing by long-lived greenhouse gases: Calculations with the AER radiative transfer models. *Journal of Geophysical Research: Atmospheres*, **113 (D13)**, D13 103.

Jeevanjee, N. and D. M. Romps, 2013: Convective self-aggregation, cold pools, and domain size. *Geophysical Research Letters*, **40 (5)**, 994–998.

Jones, S. C., 1995: The evolution of vortices in vertical shear. I: Initially barotropic vortices. *Quarterly Journal of the Royal Meteorological Society*, **121 (524)**, 821–851.

Jones, S. C., 2000: The evolution of vortices in vertical shear. III: Baroclinic vortices. *Quarterly Journal of the Royal Meteorological Society*, **126 (570)**, 3161–3185.

Jordan, C. L., 1958: Mean soundings for the west indies area. *Journal of Meteorology*, **15 (1)**, 91–97.

Khairoutdinov, M. and K. Emanuel, 2013: Rotating radiative-convective equilibrium simulated by a cloud-resolving model. *Journal of Advances in Modeling Earth Systems*, **5 (4)**, 816–825.

Khairoutdinov, M. F. and D. A. Randall, 2003: Cloud Resolving Modeling of the ARM Summer 1997 IOP: Model Formulation, Results, Uncertainties, and Sensitivities. *Journal of the Atmospheric Sciences*, **60 (4)**, 607–625.

Kim, D., et al., 2014a: Process-Oriented MJO Simulation Diagnostic: Moisture Sensitivity of Simulated Convection. *Journal of Climate*, **27 (14)**, 5379–5395.

Kim, H.-S., G. A. Vecchi, T. R. Knutson, W. G. Anderson, T. L. Delworth, A. Rosati, F. Zeng, and M. Zhao, 2014b: Tropical Cyclone Simulation and Response to CO2 Doubling in the GFDL CM2.5 High-Resolution Coupled Climate Model. *Journal of Climate*, **27 (21)**, 8034–8054.

Knutson, T. R., et al., 2010: Tropical cyclones and climate change. *Nature Geoscience*, **3 (3)**, 157–163.

Leipper, D. F., 1967: Observed Ocean Conditions and Hurricane Hilda, 1964. *Journal of the Atmospheric Sciences*, **24 (2)**, 182–186.

Lin, I.-I., et al., 2013: An ocean coupling potential intensity index for tropical cyclones. *Geophysical Research Letters*, **40 (9)**, 1878–1882.

Lin, J.-L., M.-I. Lee, D. Kim, I.-S. Kang, and D. M. W. Frierson, 2008: The Impacts of Convective Parameterization and Moisture Triggering on AGCM-Simulated Convectively Coupled Equatorial Waves. *Journal of Climate*, **21 (5)**, 883–909.

Lin, Y.-L., R. D. Farley, and H. D. Orville, 1983: Bulk Parameterization of the Snow Field in a Cloud Model. *Journal of Climate and Applied Meteorology*, **22 (6)**, 1065–1092.

Lindzen, R. S., M.-D. Chou, and A. Y. Hou, 2001: Does the Earth Have an Adaptive Infrared Iris? *Bulletin of the American Meteorological Society*, **82 (3)**, 417–432.

Lock, A. P., A. R. Brown, M. R. Bush, G. M. Martin, and R. N. B. Smith, 2000: A new boundary layer mixing scheme. Part I: Scheme description and single-column model tests. *Monthly weather review*, **128 (9)**, 3187–3199.

Madden, R. A. and P. R. Julian, 1971: Detection of a 4050 Day Oscillation in the Zonal Wind in the Tropical Pacific. *Journal of the Atmospheric Sciences*, **28 (5)**, 702–708.

Maddox, R. A., 1980: Meoscale Convective Complexes. *Bulletin of the American Meteorological Society*, **61 (11)**, 1374–1387.

Mapes, B. E. and R. A. Houze, 1993: Cloud Clusters and Superclusters over the Oceanic Warm Pool. *Monthly Weather Review*, **121 (5)**, 1398–1416.

Mauritsen, T. and B. Stevens, 2015: Missing iris effect as a possible cause of muted hydrological change and high climate sensitivity in models. *Nature Geoscience*, **8 (5)**, 346–351.

McBride, J. L. and R. Zehr, 1981: Observational Analysis of Tropical Cyclone Formation. Part II: Comparison of Non-Developing versus Developing Systems. *Journal of the Atmospheric Sciences*, **38 (6)**, 1132–1151.

Miyamoto, Y. and T. Takemi, 2015: A Triggering Mechanism for Rapid Intensification of Tropical Cyclones. *Journal of the Atmospheric Sciences*.

Mlawer, E. J., S. J. Taubman, P. D. Brown, M. J. Iacono, and S. A. Clough, 1997: Radiative transfer for inhomogeneous atmospheres: RRTM, a validated correlated-k model for the longwave. *Journal of Geophysical Research: Atmospheres*, **102 (D14)**, 16 663–16 682.

Moorthi, S. and M. Suarez, 1992a: Relaxed Arakawa-Schubert- A parameterization of moist convection for general circulation models. *Monthly Weather Review*, **120 (6)**, 978–1002.

Moorthi, S. and M. J. Suarez, 1992b: Relaxed Arakawa-Schubert. A Parameterization of Moist Convection for General Circulation Models. *Monthly Weather Review*, **120 (6)**, 978–1002.

Morrison, H., J. A. Curry, and V. I. Khvorostyanov, 2005: A New Double-Moment Microphysics Parameterization for Application in Cloud and Climate Models. Part I: Description. *Journal of the Atmospheric Sciences*, **62 (6)**, 1665–1677.

Muller, C., 2013: Impact of Convective Organization on the Response of Tropical Precipitation Extremes to Warming. *Journal of Climate*, **26 (14)**, 5028–5043.

Muller, C. J. and I. M. Held, 2012: Detailed Investigation of the Self-Aggregation of Convection in Cloud-Resolving Simulations. *Journal of the Atmospheric Sciences*, **69 (8)**, 2551–2565.

Nesbitt, S. W., E. J. Zipser, and D. J. Cecil, 2000: A Census of Precipitation Features in the Tropics Using TRMM: Radar, Ice Scattering, and Lightning Observations. *Journal of Climate*, **13 (23)**, 4087–4106.

Nolan, D. S. and E. D. Rappin, 2008: Increased sensitivity of tropical cyclogenesis to wind shear in higher SST environments. *Geophysical Research Letters*, **35 (14)**, L14 805.

Nolan, D. S., E. D. Rappin, and K. A. Emanuel, 2007: Tropical cyclogenesis sensitivity to environmental parameters in radiativeconvective equilibrium. *Quarterly Journal of the Royal Meteorological Society*, **133 (629)**, 2085–2107.

Pauluis, O. and I. M. Held, 2002a: Entropy Budget of an Atmosphere in RadiativeConvective Equilibrium. Part I: Maximum Work and Frictional Dissipation. *Journal of the Atmospheric Sciences*, **59 (2)**, 125–139.

Pauluis, O. and I. M. Held, 2002b: Entropy Budget of an Atmosphere in RadiativeConvective Equilibrium. Part II: Latent Heat Transport and Moist Processes. *Journal of the Atmospheric Sciences*, **59 (2)**, 140–149.

Popke, D., B. Stevens, and A. Voigt, 2013: Climate and climate change in a radiativeconvective equilibrium version of ECHAM6. *Journal of Advances in Modeling Earth Systems*, **5 (1)**, 1–14.

Rappin, E. D., M. C. Morgan, and G. J. Tripoli, 2011: The Impact of Outflow Environment on Tropical Cyclone Intensification and Structure. *Journal of the Atmospheric Sciences*, **68 (2)**, 177–194.

Rappin, E. D. and D. S. Nolan, 2012: The effect of vertical shear orientation on tropical cyclogenesis. *Quarterly Journal of the Royal Meteorological Society*, **138 (665)**, 1035–1054.

Rappin, E. D., D. S. Nolan, and K. A. Emanuel, 2010: Thermodynamic control of tropical cyclogenesis in environments of radiative-convective equilibrium with shear. *Quarterly Journal of the Royal Meteorological Society*, **136 (653)**, 1954–1971.

Raymond, D. J., 1995: Regulation of Moist Convection over the West Pacific Warm Pool. *Journal of the Atmospheric Sciences*, **52 (22)**, 3945–3959.

Riemer, M., M. T. Montgomery, and M. E. Nicholls, 2010: A new paradigm for intensity modification of tropical cyclones: thermodynamic impact of vertical wind shear on the inflow layer. *Atmos. Chem. Phys.*, **10 (7)**, 3163–3188.

Romps, D. M., 2008: The Dry-Entropy Budget of a Moist Atmosphere. *Journal of the Atmospheric Sciences*, **65 (12)**, 3779–3799.

Romps, D. M., 2010: Response of Tropical Precipitation to Global Warming. *Journal of the Atmospheric Sciences*, **68 (1)**, 123–138.

Rotunno, R. and K. A. Emanuel, 1987: An AirSea Interaction Theory for Tropical Cyclones. Part II: Evolutionary Study Using a Nonhydrostatic Axisymmetric Numerical Model. *Journal of the Atmospheric Sciences*, **44 (3)**, 542–561.

Schade, L. R. and K. A. Emanuel, 1999: The Oceans Effect on the Intensity of Tropical Cyclones: Results from a Simple Coupled AtmosphereOcean Model. *Journal of the Atmospheric Sciences*, **56 (4)**, 642–651.

Schecter, D. A., 2011: Evaluation of a reduced model for investigating hurricane formation from turbulence. *Quarterly Journal of the Royal Meteorological Society*, **137 (654)**, 155–178.

Schecter, D. A. and T. J. Dunkerton, 2009: Hurricane formation in diabatic Ekman turbulence. *Quarterly Journal of the Royal Meteorological Society*, **135 (641)**, 823–838.

Shen, W. and I. Ginis, 2003: Effects of surface heat flux-induced sea surface temperature changes on tropical cyclone intensity. *Geophysical Research Letters*, **30 (18)**, 1933.

Simpson, J., E. Ritchie, G. J. Holland, J. Halverson, and S. Stewart, 1997: Mesoscale Interactions in Tropical Cyclone Genesis. *Monthly Weather Review*, **125 (10)**, 2643–2661.

Singh, M. S. and P. A. O'Gorman, 2013: Influence of entrainment on the thermal stratification in simulations of radiative-convective equilibrium. *Geophysical Research Letters*, **40 (16)**, 4398–4403.

Skamarock, W., J. Klemp, and J. Dudhia, 2008: A Description of the Advanced Research WRF Version 3. NCAR Technical Note NCAR/TN-475+STR.

Smith, R. K., G. Kilroy, and M. T. Montgomery, 2014: Why Do Model Tropical Cyclones Intensify More Rapidly at Low Latitudes? *Journal of the Atmospheric Sciences*, **72 (5)**, 1783–1804.

Sobel, A. H., J. Nilsson, and L. M. Polvani, 2001: The Weak Temperature Gradient Approximation and Balanced Tropical Moisture Waves*. *Journal of the Atmospheric Sciences*, **58 (23)**, 3650–3665.

Stern, D. P. and D. S. Nolan, 2012: On the Height of the Warm Core in Tropical Cyclones. *Journal of the Atmospheric Sciences*, **69 (5)**, 1657–1680.

Tang, B. and K. Emanuel, 2010: Midlevel Ventilations Constraint on Tropical Cyclone Intensity. *Journal of the Atmospheric Sciences*, **67 (6)**, 1817–1830.

Tang, B. and K. Emanuel, 2012: A Ventilation Index for Tropical Cyclones. *Bulletin of the American Meteorological Society*, **93 (12)**, 1901–1912.

Tobin, I., S. Bony, C. E. Holloway, J.-Y. Grandpeix, G. Sze, D. Coppin, S. J. Woolnough, and R. Roca, 2013: Does convective aggregation need to be represented in cumulus parameterizations? *Journal of Advances in Modeling Earth Systems*, **5 (4)**, 692–703.

Tobin, I., S. Bony, and R. Roca, 2012: Observational Evidence for Relationships between the Degree of Aggregation of Deep Convection, Water Vapor, Surface Fluxes, and Radiation. *Journal of Climate*, **25 (20)**, 6885–6904.

Tompkins, A. M., 2000: The Impact of Dimensionality on Long-Term Cloud-Resolving Model Simulations. *Monthly Weather Review*, **128 (5)**, 1521–1535.

Wang, Y., L. Zhou, and K. Hamilton, 2007: Effect of Convective Entrainment/Detrainment on the Simulation of the Tropical Precipitation Diurnal Cycle*. *Monthly Weather Review*, **135 (2)**, 567–585.

Wang, Z., 2014: Role of Cumulus Congestus in Tropical Cyclone Formation in a High-Resolution Numerical Model Simulation. *Journal of the Atmospheric Sciences*, **71 (5)**, 1681–1700.

Wehner, M., Prabhat, K. A. Reed, D. Stone, W. D. Collins, and J. Bacmeister, 2015: Resolution Dependence of Future Tropical Cyclone Projections of CAM5.1 in the U.S. CLIVAR Hurricane Working Group Idealized Configurations. *Journal of Climate*, **28 (10)**, 3905–3925.

Wing, A. A. and K. A. Emanuel, 2014: Physical mechanisms controlling self-aggregation of convection in idealized numerical modeling simulations. *Journal of Advances in Modeling Earth Systems*, **6 (1)**, 59–74.

Zhang, F. and D. Tao, 2013: Effects of Vertical Wind Shear on the Predictability of Tropical Cyclones. *Journal of the Atmospheric Sciences*, **70 (3)**, 975–983.

Zhao, M. and I. M. Held, 2010: An Analysis of the Effect of Global Warming on the Intensity of Atlantic Hurricanes Using a GCM with Statistical Refinement. *Journal of Climate*, **23 (23)**, 6382–6393.

Zhao, M., I. M. Held, S. J. Lin, and G. A. Vecchi, 2009: Simulations of global hurricane climatology, interannual variability, and response to global warming using a 50-km resolution GCM. *Journal of Climate*, **22 (24)**, 6653–6678.

Zhou, W., I. M. Held, and S. T. Garner, 2014: Parameter Study of Tropical Cyclones in Rotating RadiativeConvective Equilibrium with Column Physics and Resolution of a 25-km GCM. *Journal of the Atmospheric Sciences*, **71 (3)**, 1058–1069.

Zhu, T. and D.-L. Zhang, 2006: The impact of the storm-induced SST cooling on hurricane intensity. *Advances in Atmospheric Sciences*, **23 (1)**, 14–22.